

UNIVERSITY OF NOVA GORICA
GRADUATE SCHOOL

**LOW-TEMPERATURE SYNTHESIS,
CHARACTERIZATION AND APPLICATION OF TiO₂
AND TiO₂/SiO₂ POWDERS IN PHOTODEGRADATION
OF VOCs**

DISSERTATION

MINOO TASBIHI

Mentor: Prof. dr. Urška Lavrenčič Štangar

Nova Gorica, 2010

SUMMARY

Recently, emission of volatile organic compound (VOCs) in air and water has become a very serious problem causing different degrees of hazard to public health. In order to remove VOCs, different techniques have been developed and used. One of them is photochemical oxidation (PCO), which is widely used in recent years. The aim of this method is to mineralize VOCs (the pollutants) to CO₂, H₂O and mineral acids and salts. TiO₂ is the most common semiconductor used as a photocatalyst for PCO and has been extensively studied over the last 20 years. Compared to other methods, TiO₂-photocatalysis has some obvious advantages, but on the other hand there are also some drawbacks. The goals of my Ph.D. research were to overcome some of the problems in application of TiO₂ in photochemical oxidation process. The major goals of my research were: (1) preparation of nanocrystalline TiO₂ by employing low-temperature preparation technique; (2) investigation of its photocatalytic activity towards degradation of aqueous phenol solution; (3) loading of aqueous titania sol into/onto silica mesoporous powder for enhancing active surface area; (4) studying its photocatalytic activity towards degradation of gaseous toluene in the self-constructed fluidized-bed photoreactor system, which was built for this purpose.

In this study, first, the anatase nanocrystalline TiO₂ powders were synthesized using titanium tetrachloride (TiCl₄) as a precursor via sol-gel method at low-temperature preparation conditions. These powders were designated as unsupported TiO₂ powders of the two types (Ti-Cl and Ti-N) since perchloric acid (HClO₄) and nitric acid (HNO₃) were used as peptizing mediators. The photocatalytic activities of the as-prepared powders were studied towards degradation of aqueous phenol solution under UVA radiation. The HClO₄-based TiO₂ had approximately a 1.5 times higher catalytic activity than similar catalysts prepared by using HNO₃. Smaller aggregated colloidal particles, and consequently a larger surface area in HClO₄-based powder, demonstrate the main reason for better photocatalytic activity compared to the HNO₃-based powder.

The aggregation of the as-prepared TiO₂ nanocrystallites often prevents a high catalytic activity. In this regard, I tried to support (to fix) the nanocrystals of TiO₂ within mesoporous silica materials to gain higher photocatalytic activity in a gaseous

phase. Ordered (SBA-15) and disordered (KIL-2) mesoporous silica supports have been synthesized and loaded with different amount of titania via sol-gel impregnation method. Aqueous titania sol prepared by low-temperature sol-gel method and by employing HClO_4 as a peptizing agent was used as a source of titania. The Ti/Si nominal molar ratio was adjusted to 1/2, 1/1 and 2/1. The powders prepared from KIL-2 and SBA-15 were designated as Ti/KIL-2(x) and Ti/SBA-15(x), respectively, where x means the Ti/Si nominal molar ratio that was adjusted to 1/2, 1/1 and 2/1.

The physico-chemical properties of as-prepared samples were characterized by different techniques. The influences of Ti/Si molar ratio and of the mesoporous silica structure were investigated by measuring adsorption capacity and photocatalytic degradation of gaseous toluene as a representative of a VOC pollutant. The photocatalytic degradation of toluene was carried out in a self-constructed gaseous fluidized-bed photoreactor equipped with UVA light source and connected on-line to the GC-MS analyzer. The rates of photocatalytic degradation reactions were found to be similar for photocatalysts with the same Ti/Si molar ratio and were not dependent on the mesoporous structure of silica. The adsorption capacity was decreasing as a function of the increasing Ti/Si molar ratio in the case of both types of mesoporous silica support. However, the photocatalytic degradation proceeded faster for the Ti/Si molar ratio 1/1 while, in the case of the other investigated Ti/Si molar ratios 1/2 and 2/1, the degradation rates were lower. In general, the photocatalytic activity was considerably improved by using supported titania-silica catalyst compared to an unsupported titania powder prepared from the same nanocrystalline titania sol. Furthermore, titania/silica powders were tested for photocatalytic degradation of isopropanol in the gaseous medium at the Slovenian National Building and Civil Engineering Institute, Ljubljana. The adsorption capacity of isopropanol was the highest in the presence of the SBA-15-supported powders. The photoactivity results indicated that the powders which were prepared using SBA-15 as a silica support and a Ti/Si molar ratio of 1/1 were the most active toward isopropanol oxidation monitored in-situ by FT-IR spectroscopy. The photocatalytic results obtained from two different solid-gas photoreactor systems confirmed the beneficial influence of mesoporous silica support to an increased activity of low-temperature titania.

LIST OF CONTENT:

SUMMARY	I
LIST OF FIGURES	VII
LIST OF TABLES	X
ABBREVIATIONS	XI
SYMBOLS.....	XIII
I. INTRODUCTION	1
II. Theoretical background.....	3
2.1. Advanced oxidation processes (AOPs).....	3
2.1.1. General mechanism of photocatalytic process.....	4
2.1.2. Titanium dioxide (TiO ₂) photocatalyst.....	6
2.2. Synthesis processes of TiO ₂	8
2.2.1. Sol–gel process	8
2.2.1.1. Low–temperature sol–gel process	11
2.3. Support (for the photocatalyst)	13
2.3.1. Porous materials.....	17
2.3.1.1. Well–ordered mesoporous silica materials (SBA–15 type).....	18
2.3.1.2. Foam–like (disordered) mesoporous silica materials (KIL–2 type) .	20
2.4. Techniques for depositing TiO ₂ into/onto porous material	22
2.5. Organic contaminants	25
2.5.1. Phenol	26
2.5.2. Toluene	27
2.5.3. Isopropanol	30
2.6. Photoreactor concepts	31
2.6.1. Photoreactors for water treatment.....	33
2.6.2. Photoreactors for air treatment	34
2.6.2.1. Fluidized–bed photoreactor	37
2.6.2.2. Annular photoreactor	41
III. Research goals	43
IV. Experimental.....	45
4.1. Chemicals.....	45
4.2. Synthesis of materials	45
4.2.1. Synthesis of unsupported titania materials	45
4.2.1.1. Synthesis of aqueous titania sol	45
4.2.1.2. Synthesis of unsupported titania powders	46
4.2.2. Synthesis of supported titania powders	47
4.2.2.1. Synthesis of KIL–2 as a silica support.....	47
4.2.2.2. Synthesis of SBA–15 as a silica support	47
4.2.2.3. Synthesis of titania/silica powders: MTi/KIL–2 and MTi/SBA–15 using Ti–isopropoxide	48
4.2.2.4. Synthesis of titania/silica powders: STi/KIL–2 and STi/SBA–15 using aqueous titania sol	48
4.3. Characterization of materials	49
4.3.1. X–ray diffraction (XRD)	49
4.3.2. Dynamic light scattering (DLS).....	50
4.3.3. UV–vis spectroscopy	50
4.3.3.1. UV–vis transmittance	50
4.3.3.2. UV–vis diffuse reflectance (UV–vis DRS)	51
4.3.4. Nitrogen–sorption measurement.....	52

4.3.5. Electron microscopy	52
4.3.5.1. Scanning electron microscopy (SEM)	52
4.3.5.2. High resolution transmittance electron microscopy (HR-TEM)	52
4.3.6. Elemental analysis	53
4.3.7. Fourier transform infrared spectroscopy (FT-IR)	53
4.3.8. Thermal analysis (TGA-DSC)	53
4.4. Photocatalytic activity tests	54
4.4.1. Determination of photocatalytic activities in liquid-solid system	54
4.4.1.1. Photoreactor set-up	54
4.4.1.2. Photocatalytic degradation of phenol	54
4.4.1.3. High performance liquid chromatography (HPLC) analysis.....	55
4.4.2. Determination of photocatalytic activities in gas-solid system with in-situ FT-IR	57
4.4.2.1. Photoreactor set-up	57
4.4.2.2. Photocatalytic degradation of isopropanol	57
4.4.3. Determination of photocatalytic activities in gas-solid system with in-situ GC-MS	60
4.4.3.1. Photoreactor set-up	60
4.4.3.2. Photocatalytic degradation of toluene	60
4.4.3.3. Gas chromatography-mass spectrometry (GC-MS) analysis	61
V. Results and discussion	64
5.1. Unsupported titania materials	64
5.1.1. XRD analysis	64
5.1.1.1. Impact of peptizing agent (acid)	64
5.1.1.2. Impact of the [Ti]/[H ⁺] ratio	66
5.1.1.3. Impact of calcination temperature	68
5.1.2. Dynamic light scattering.....	71
5.1.3. UV-vis spectra	72
5.1.3.1. UV-vis transmittance	72
5.1.3.2. UV-vis diffuse reflectance	73
5.1.4. Nitrogen-sorption measurement.....	74
5.1.5. Scanning electron microscopy of titania powders.....	77
5.1.6. Thermal analysis (TGA-DSC)	78
5.1.7. Photocatalytic degradation of phenol	80
5.2. Titania/silica powders.....	84
5.2.1. XRD analysis.....	84
5.2.1.1. Small-angle XRD analysis	84
5.2.1.2. Wide-angle XRD analysis.....	86
5.2.2. UV-vis diffuse reflectance	89
5.2.3. Nitrogen-sorption measurement.....	93
5.2.4. Scanning electron microscopy.....	100
5.2.5. High resolution transmittance electron microscopy (HR-TEM)	102
5.2.6. Fourier transform infrared spectroscopy (FT-IR)	109
5.2.7. The photocatalytic activity towards gaseous isopropanol degradation ..	112
5.2.8. The photocatalytic activity towards gaseous toluene degradation	118
5.2.9. Regeneration of the partially deactivated photocatalyst.....	125
VI. Conclusions	127
VII. References	130

LIST OF FIGURES

Fig 1: Schematic representation of photochemical process in and on a semiconductor particle (for example TiO ₂) (Oppenlander, 2003)	5
Fig 2: Crystal structures of (A) anatase; (B) rutile; (C) brookite of TiO ₂ (Carp et al., 2004)	6
Fig 3: Scheme of the sol–gel processing options (Brinker and Scherer, 1990).....	9
Fig 4: Schematic illustration of several functions assigned to a support in a photocatalytic system (Serpone and Pelizzetti, 1989).	16
Fig 5: Nitrogen adsorption–desorption isotherms of (A) pore system with completely open mesopores and intrawall micropores (SBA–15); (B) pore system with blocked mesopore openings (ink–bottle pores) and intrawall micropores (PHTS–3); (C)“plugged” mesopores, comprising both open and blocked mesopores, intrawall micropores, and microporous silica nanocapsules (PHTS–2) (Van der Voort et al., 2002).	20
Fig 6: Nitrogen sorption isotherm with pore size distribution curve (inset) of KIL–2 (Novak Tušar et al., 2010)	22
Fig 7: A possible mechanism of phenol destruction and mineralization on illuminated TiO ₂ (Sobczynski et al., 2004).....	27
Fig 8: Types of ideal chemical reactors for water treatment: (A) batch reactor; (B) mixed flow reactor; (C) plug flow reactor; (D) batch recirculation reactor (Levenspiel, 1999)	33
Fig 9: Process technologies for air pollution control (Oppenlander, 2003).....	35
Fig 10: Bed expansion at minimum fluidization (Howard, 1989).....	38
Fig 11: Pressure drop versus fluid velocity for packed and fluidized beds (Howard, 1989)	39
Fig 12: Scheme of the photocatalytic annular reactor: (1) gas inlet, (2) outer tube with the catalyst layer, (3) inner tube, (4) end plate, (5) gas outlet, (6) UV tube, (7) rubber O ring (Tomasic et al., 2008)	42
Fig 13: Determination of energy band gap from a transformed diffuse reflectance spectrum (Kuči et al., 2009).....	51
Fig 14: Photoreactor set–up for aqueous system: (A) the side view; (B) the upper view; (C) a photocatalytic cell with an aqueous phenol solution and dispersed catalyst used for the photocatalytic experiment.....	56
Fig 15: Schematic diagram of the experimental set–up for in–situ FT–IR gaseous system	59
Fig 16: A photo of photoreactor set–up for in–situ FT–IR gaseous system (provided by Slovenian National Building and Civil Engineering Institute, Ljubljana).....	59
Fig 17: Schematic diagram of the set–up for in–situ GC–MS gaseous photocatalysis: (1) gas regulator, (2) 3–way valve, (3) mass flow meter/controller, (4) humidifier, (5) mixing chamber, (6) syringe pump, (7) thermometer and humidity meter, (8) diaphragm pump, (9) water bath, (10) reservoir vessel, (11) flow meter, (12) reactor cell with surrounding UVA lamps, (13) sampling port, (14) GC–MS	62
Fig 18: (A) A photo of the photoreactor set–up for in–situ GC–MS gaseous photocatalysis; (B) GC–MS instrument.....	63
Fig 19: X–ray diffraction pattern of the precipitate obtained after neutralization of TiCl ₄ and washing with water (A = anatase)	64
Fig 20: X–ray diffraction patterns of as–prepared samples Ti–N and Ti–Cl at the (a) [Ti]/[H ⁺] = 0.5; (b) [Ti]/[H ⁺] = 2.5 ratios (A = anatase, R = rutile, B = brookite, * = TiO(ClO ₄) ₂ ·6H ₂ O).....	66

Fig 21: X-ray diffraction patterns of as-prepared samples (a) Ti-Cl(0.5), Ti-Cl(2.5); (b) Ti-N(0.5), Ti-N(2.5) (A = anatase, R = rutile, B = brookite, * = TiO(ClO ₄) ₂ ·6H ₂ O)	67
Fig 22: X-ray diffraction patterns of samples before and after calcination at 600 °C (a) Ti-N(2.5); (b) Ti-N(0.5) (A = anatase, R = rutile, B = brookite).....	69
Fig 23: X-ray diffraction patterns of samples before and after calcination at 600 °C (a) Ti-Cl(2.5); (b) Ti-Cl(0.5) (A = anatase, R = rutile, B = brookite, * = TiO(ClO ₄) ₂ ·6H ₂ O)	70
Fig 24: UV-vis transmittance spectra of the colloidal solutions (the same as used for the photocatalytic experiments) made from as-prepared powders: (a) Ti-Cl(0.5); (b) Ti-N(0.5)	72
Fig 25: DR UV-vis spectra of (a) Ti-Cl(0.5) and Ti-Cl(2.5); (b) Ti-Cl(0.5), calcined Ti-Cl(0.5) at 400 °C and 600 °C	74
Fig 26: The adsorption-desorption isotherm curves for the titania samples; (a) before calcination; (b) calcined at 400 °C	76
Fig 27: SEM micrographs of powders (a) Ti-Cl(0.5); (b) Ti-Cl(2.5); (c) Ti-N(0.5)	78
Fig 28: SEM micrographs of calcined powders at 400 °C (a) Ti-Cl(0.5); (b) Ti-N(0.5).....	78
Fig 29: TGA-DSC analysis of (a) Ti-N(0.5); (b) Ti-Cl(0.5) powders.....	80
Fig 30: Photocatalytic degradation of phenol by using different as-prepared powders	82
Fig 31: Photocatalytic degradation of phenol for HClO ₄ -prepared powders calcined at 400 °C.....	83
Fig 32: Small-angle X-ray powder diffraction (XRD): (A) SBA-15, STi/SBA-15(x), MTi/SBA-15(1/1); (B) KIL-2, STi/KIL-2(x), MTi/KIL-2(1/1).....	85
Fig 33: Wide-angle X-ray powder diffraction (XRD): (A) SBA-15, STi/SBA-15(x), MTi/SBA-15(1/1); (B) KIL-2, STi/KIL-2 (x), MTi/KIL-2(1/1)	87
Fig 34: Wide-angle X-ray powder diffraction (XRD): (A) STi/SBA-15(1/1); (B) STi/KIL-2(1/1)	88
Fig 35: DR UV-vis spectra of (A) STi/SBA-15(x), MTi/SBA-15(1/1), Ti-Cl(2.5); (B) STi/KIL-2(x), MTi/KIL-2(x), Ti-Cl(2.5)	91
Fig 36: Absorption spectra of (A) Ti-Cl(2.5), STi/SBA-15(x); (B) Ti-Cl(2.5), STi/KIL-2(x).....	92
Fig 37: (A) Nitrogen-sorption isotherms; (B) pore size distribution of SBA-15, STi/SBA-15(x), MTi/SBA-15(1/1)	96
Fig 38: (A) Nitrogen-sorption isotherms; (B) pore size distribution of KIL-2, STi/KIL-2(x), MTi/KIL-2(1/1)	99
Fig 39: SEM images of (a) SBA-15; (b) STi/SBA-15(1/2); (c) STi/SBA-15(1/1); (d) STi/SBA-15(2/1); (e) MTi/SBA-15(1/1)	101
Fig 40: SEM images of (a) KIL-2; (b) STi/KIL-2(1/2); (c) STi/KIL-2(1/1); (d) STi/KIL-2(2/1); (e) MTi/KIL-2(1/1).....	102
Fig 41: SEM images of (a) STi/SBA-15(1/1); (b) STi/KIL-2(1/1) after calcination at 300 °C.....	102
Fig 42: HR-TEM micrographs of (a) SBA-15; (b) STi/SBA-15(1/2); (c) STi/SBA-15(1/1); (d) STi/SBA-15(2/1) at different magnifications.....	105
Fig 43: HR-TEM micrographs of (a) STi/KIL-2(1/2); (b) STi/KIL-2(1/1); (c) STi/KIL-2(2/1) at different magnifications and inset ED pattern of STi/KIL-2(2/1)	106
Fig 44: EDX analysis of STi/SBA-15(1/1) (A) at point without presence of Ti; (B) at point with presence of Ti	107

Fig 45: EDX analysis of STi/KIL-2(1/1) (A) at point without presence of Ti; (B) at point with presence of Ti	108
Fig 46: FT-IR spectra of (A) Ti-Cl(2.5); (B) SBA-15, STi/SBA-15(x); (C) KIL-2, STi/KIL-2(x)	111
Fig 47: (A) Dark adsorption of isopropanol (negative illumination times) and its photocatalytic disappearance; (B) acetone formation curves in presence of SBA-15, STi/SBA-15(x), MTi/SBA-15(1/1), Ti-Cl(2.5), blank	116
Fig 48: (A) Dark adsorption of isopropanol (negative illumination times) and its photocatalytic disappearance; (B) acetone formation curves in presence of KIL-2, STi/KIL-2(x), MTi/KIL(1/1), Ti-Cl(2.5), blank.....	117
Fig 49: Concentration of toluene measured prior to and after turning on the UV lamp for (A) blank, Ti-Cl(2.5), SBA-15, STi/SBA-15(x), Millennium PC500; (B) blank, Ti-Cl(2.5), KIL-2, STi/KIL-2(x), Millennium PC500.....	124
Fig 50: Concentration of toluene measured prior to and after turning on the UV lamp for (A) fresh STi/SBA-15(1/1), 1× regenerated STi/SBA-15(1/1), 2× regenerated STi/SBA-15(1/1); (B) fresh STi/KIL-2(1/1), 1× regenerated STi/KIL-2(1/1), 2× regenerated STi/KIL-2(1/1)	126

LIST OF TABLES

Table 1: Suspended versus immobilized photocatalytic systems.....	34
Table 2: Examples of research related to photo-initiated AOPs in a gaseous phase.....	37
Table 3: The TiO ₂ content in different unsupported titania powders.....	46
Table 4: Crystallite sizes (obtained by XRD) and particle sizes in solution (obtained by DLS).....	71
Table 5: Surface area, pore volume, pore size and band-gap energy of as-prepared and calcined powders.....	75
Table 6: The rate constant of phenol degradation in the presence of different powders.....	81
Table 7: Structural parameters of titania/silica powders determined from XRD.....	89
Table 8: Band-gap energies of the powders determined with different amount of Ti.....	93
Table 9: Structural parameters of powders determined from N ₂ sorption measurements.....	97
Table 10: The acetone formation rate in the presence of different powders.....	118
Table 11: Dark adsorption capacities and photocatalytic rate constants of used powders.....	123

ABBREVIATIONS

A = acceptor species

AOPs = advanced oxidation processes

ASHRAE = American Society of Heating, Refrigeration and Air-Conditioning Engineering

BET = Brunauer-Emmett-Teller

BJH = Barrett, Joyner, Halenda

BSE = back-scattered electron

BTEX = benzene, toluene, ethylbenzene, xylene

CB = conduction band

CVD = chemical vapour deposition

D = donor species

1D = one-dimensional model

2D = two-dimensional model

DLS = dynamic light scattering

ED = electron diffraction

EDX = energy dispersive X-ray

EI = electron impact

e_{cb}^- = conduction-band electron

FBR = fluidized-bed reactor

FT-IR = Fourier transform infrared spectroscopy

GC-MS = gas chromatography – mass spectrometry

HPLC = high performance liquid chromatography

HR-TEM = high resolution – transmittance electron microscope

h_{vb}^+ = valence-band hole

ICP-AES = inductively-coupled plasma-atomic emission spectroscopy

IUPAC = International Union of Pure and Applied Chemistry

JCPDS = Joint Committee on Powder Diffraction Standards

KIL = Kemijski Inštitut Ljubljana amorphous mesoporous silica

MCM = Mobile Composition of Matter

MSNs = mesoporous silica nanoparticles

OMMs = ordered mesoporous materials

OMSs = ordered mesostructured silicates

$\cdot\text{OH}$ = hydroxyl radical

PCBs = polychlorobiphenyls
PHTSs = plugged hexagonal templated silicates
PSDs = pore size distributions
PVD = physical vapour deposition
SBA = Santa Barbara Amorphous mesoporous silica
SC = semiconductor
SE = secondary electron
SEM = scanning electron microscopy
SPD = spray pyrolysis deposition
TGA–DSC = thermal gravimetric analysis–differential scanning calorimetry
UV = ultraviolet
UV–vis–DR = ultraviolet–visible diffuse reflectance spectroscopy
VB = valence band
VOCs = volatile organic compounds
VUV = vacuum ultraviolet
XRD = X–ray diffraction

SYMBOLS

U_{mf} = minimum fluidization velocity

ρ_p = particle density, kg m^{-3}

ρ_f = fluid density, kg m^{-3}

H = depth of bed, m

ε = voidage

A = cross sectional area, m^2

g = acceleration of gravity, m s^{-2}

ΔP = pressure drop across the bed, N m^{-2}

U = fluid velocity, m s^{-1}

μ = fluid viscosity, Ns m^{-2}

d_p = particle diameter, μm

Ar = Archimedes number

Re_{nu} = Reynolds number

Re_{mf} = Reynolds number at incipient fluidization

ε_{mf} = voidage at incipient fluidization

L = crystallite size

λ = wavelength

k = shape factor

β = peak width at half-maximum height

D = diffusion coefficient, m s^{-2}

τ = relaxation time, s

q = scattering vector, m^2

R_h = hydrodynamic radius, m

k_B = Boltzmann constant, J K^{-1}

T = absolute temperature, K

η = solvent viscosity, cP

K = Kubelka–Munk function

$h\nu$ = photon energy

α = absorption coefficient

E_{bg} = band-gap energy

V_t = total pore volume

V_{me} = primary mesoporous volume

S_{ex} = external surface area

S_{me} = mesoporous surface area

W_{BJH} = mesoporous diameters at the maximum (maxima) of the BJH pore size distribution

I. INTRODUCTION

Over last few decades the United Nations have developed and agreed an extensive system of international documents in order to involve and oblige their member countries for comprehensive protection of global environment against pollution and devastation. The European Union promptly followed the development to be implemented in the former as well as in the new member states. The main subjects of concern are global warming, stratospheric ozone layer depletion, troposphere photochemical pollution and noise and radiation which all affect human health, biodiversity and environmental quality.

The most air-polluting group sources are:

- (i) combustion in energy and transformation industries,
- (ii) non-industrial combustion plants,
- (iii) combustion in manufacturing industry,
- (iv) production processes,
- (v) extraction and distribution of fossil fuels,
- (vi) solvent and other product use,
- (vii) road transport,
- (viii) other mobile sources and machinery,
- (ix) waste treatment and disposal,
- (x) agriculture,
- (xi) other sources and sinks.

Volatile organic compounds (VOCs), as a group of the principle air and water pollutants, are defined as any organic compounds, having at 293.15 K (i.e. 20 °C) a vapor pressure of 0.01 kPa or more (1999/13/EC). For hydrocarbons solvents a vapor pressure of 0.01 kPa at 20 °C correspond to a boiling point or initial boiling point in the range 215–220 °C. This limit value is very high, so that practically all liquid organic compounds and many solid ones must be considered (1999/13/EC).

Since a large number of VOCs is oxidizable, chemical oxidation processes (a group of technologies known as advanced oxidation processes or AOPs) can be considered

as a possible method among the various alternative forms of treatment for air and water pollutant control. Photocatalytic oxidation of VOCs using titanium dioxide (TiO_2) as a catalyst has been proposed as an alternative advanced oxidation process for the decontamination of water and air (Litter,1999).

For using TiO_2 as a photocatalyst, poor adsorption and relatively low surface area properties lead to sever limitations in exploiting the photocatalyst to the best of its photoefficiency. Mesoporous silica material with high surface area is considered as a promising support for improving the efficiency of TiO_2 for decomposing the organic pollutants in water and air.

The titania loaded mesoporous/nanoporous supports have some advantages in the photocatalysis such as: (1) formation of separated titania nanoparticles in the final composition, (2) increase of adsorption capacity especially for non-polar compounds, (3) lower scattering of UV irradiation.

Beside a development of the photocatalytic materials with increased efficiencies, a development of suitable photocatalytic reactor system is of the same importance to treat the polluted media efficiently.

II. Theoretical background

2.1. Advanced oxidation processes (AOPs)

AOPs have become increasingly popular for chemical treatment of industrial waste water, contaminated ground water, drinking water and air. AOPs have been defined broadly as oxidation processes which are primarily based on the intermediacy of the hydroxyl radicals in the mechanism(s) resulting in the destruction of the contaminant compound. Some of the processes to obtain these radicals are: ozone (O_3) treatment, O_3/H_2O_2 , VUV, O_3/UV , UV/H_2O_2 , $O_3/UV/H_2O_2$, Fenton's treatment and photocatalysis. Photocatalysis processes use semiconductors as a catalysts in combination with UV radiation and oxygen (Esplugas et al., 2002). Heterogeneous photocatalysis can be considered as an advanced oxidation technology and has been proven to be a promising method for the elimination of toxic and bio-resistant organic and some of the inorganic compounds (Chen and Ray, 1999). The main difference compared to other AOPs stated above is the use of the semiconductor metal oxide as a catalyst instead of oxidants like H_2O_2 and O_3 which are considered as expensive reactants (Esplugas et al., 2002).

Heterogeneous photocatalysis can be carried out in various media, namely gaseous phase, pure organic liquid phase or aqueous solution. The overall photocatalytic process can be divided into five independent steps (Herrmann, 1999):

- 1– mass transfer of reactants (contaminants) to the catalyst surface,
- 2– adsorption of the reactants on the catalyst surface,
- 3– photochemical reaction on the surface,
- 4– desorption of the products from the surface,
- 5– mass transfer of the products from the surface into the bulk of the fluid.

A highly attractive advantage of the heterogeneous photocatalytic treatment is that it is capable of decomposing many kinds of organic and inorganic compounds under ambient temperature (Obuchi et al., 1999). The process is non-selective to a very broad range of chemicals. Variety of organic compounds such as alkanes and alkenes, phenolic compounds, aromatics, organic acids and amines and also inorganic compounds especially transition metal ions, cyanide or nitrite can be

degraded. Other advantages are: no additives required, cheap chemicals can be used, total mineralization achieved for many organic pollutants, suitable for low concentration, possible combination with other decomposition methods (in particular biological) (Herrmann, 1999).

In most cases, the semiconductors used as photocatalysts can be activated by sunlight which makes them economically competitive. Many semiconductors such as TiO_2 , ZnO , CdS , ZnS , SnO_2 , Fe_2O_3 and WO_3 have been studied as photocatalysts (Hoffmann et al., 1995).

2.1.1. General mechanism of photocatalytic process

The ability to degrade organic and inorganic pollutants comes from the redox reaction undergoing after photo-activation of the semiconductor material. A semiconductor (SC) material has an electronic band structure in which the highest occupied energy band is called valence band (VB) and the lowest empty band is called conduction band (CB). These bands are separated by a band gap which is in the order of electron volts (Litter, 1999).

When a photon of energy higher or equal to the band-gap value of the semiconductor is absorbed by a particle, an electron from the VB is promoted to the CB with simultaneous generation of a photogenerated hole (h_{vb}^+) in the VB and photogenerated electron (e_{cb}^-) in the CB (Eq. (1)) (Li Puma et al., 2008).

The general mechanism of the hydroxyl-radical mediated photocatalytic reaction process is represented by Eqs. 1–12 following the example of TiO_2 , but also other semiconductors with similar band gap energies and valence and conduction band electrochemical positions act in the same way. It must be noted that although both anatase and rutile type of TiO_2 absorb UV radiation, rutile type of TiO_2 can also absorb radiation that is nearer to visible light. However, anatase type of TiO_2 exhibits higher photocatalytic activity than rutile due to its conduction band position which demonstrates stronger reducing power as compared to rutile type of TiO_2 (the band-gap value of anatase TiO_2 is 3.2 eV and for rutile TiO_2 is 3.0 eV). The e_{cb}^- and the h_{vb}^+ can recombine on the surface or in the bulk of the particle in a few nanoseconds

(Eq. (8)) (and the energy is dissipated as heat) or can be trapped in surface states where they can react with donor (D) or acceptor (A) species adsorbed or close to the surface of the particle. Thereby, subsequent redox reactions can be initiated (Eqs. (2)–(4)) (Figure 1).

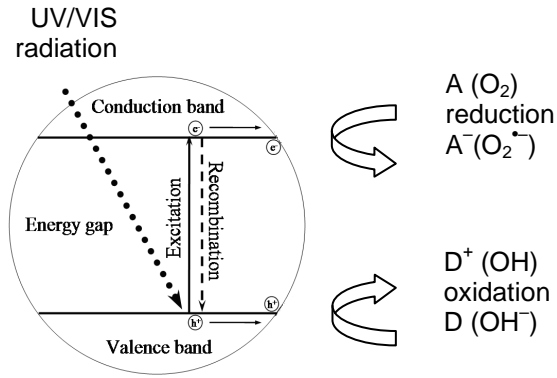


Fig 1: Schematic representation of photochemical process in and on a semiconductor particle (for example TiO₂) (Oppenlander, 2003)

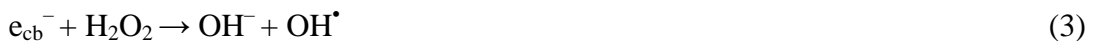
Principally it is accepted that the initial step for photocatalytic degradation is the formation of extremely reactive but short-lived hydroxyl radical ($\cdot\text{OH}$) by hole trapping (Eqs. 5, 6). The $\cdot\text{OH}$ is formed on the highly hydroxylated semiconductor surface. This process is immediately followed by the reduction of adsorbed oxygen species, derived either from dissolved oxygen molecules, or by other electron acceptors available. Main reactions governing the photocatalysis process are as follows:

Electron-hole pair formation:



(Semiconductor valence band hole and conduction band electron)

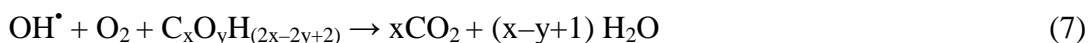
Electron removal from the conduction band:



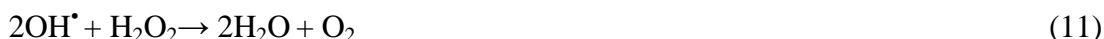
Hole trapping:



Oxidation of organic pollutant molecules:



Non-productive radical reactions:



2.1.2. Titanium dioxide (TiO₂) photocatalyst

TiO₂ is a versatile material that has applications in wide assortment of products including paint, white pigments, plastic, inks, paper, sunscreen lotions, electrochemical electrodes, food stuffs, pharmaceuticals and solar cells (Music et al., 1997; Schneider and Baiker, 1997).

Titanium dioxide exists in four mineral forms: anatase, rutile, brookite and titanium dioxide (B) or TiO₂ (B). Anatase type of TiO₂ has a crystalline structure that corresponds to the tetragonal symmetry. Rutile type of TiO₂ also has a tetragonal crystalline structure and is mainly used as a white pigment in paints. Brookite type of TiO₂ has an orthorhombic crystalline structure (Figure 2). TiO₂ (B) is a monoclinic mineral and is relatively a newcomer to the titania family (Carp et al., 2004).

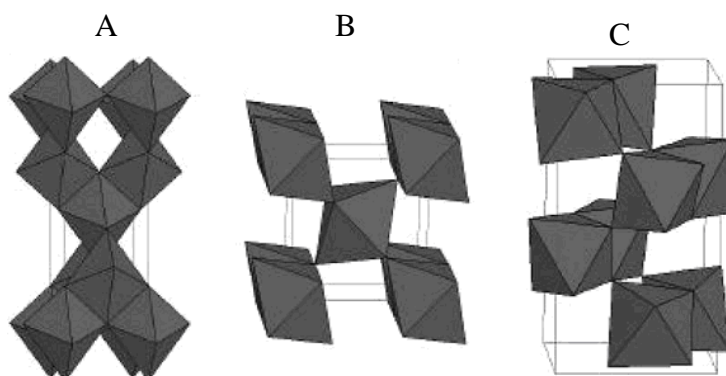


Fig 2: Crystal structures of (A) anatase; (B) rutile; (C) brookite of TiO₂ (Carp et al., 2004)

Since 1972, when Fujishima and Honda (1972) reported about water splitting on TiO₂ single crystal electrodes, titanium dioxide has been intensively investigated as a

semiconductor photocatalyst in the new field of solar energy conversion, water splitting and environmental purification. In 1976, Carey et al. (1976) observed degradation of polychlorobiphenyls (PCBs) using TiO₂ catalyst by UV radiation. Afterwards, numerous researches have been done on degradation of different pollutants utilizing TiO₂/UV system, as well as the basic studies on the mechanism of degradation reactions (Carey et al., 1976). In the last decade, however, TiO₂ has been developed and used also as a photocatalyst for indoor and outdoor air purification and for the purification and remediation of contaminated waters and air loaded with low concentrations of toxic organic pollutants (Yu et al., 2006).

The popularity of TiO₂ as a photocatalyst is based on its environmentally friendly nature (i.e. non toxicity), low cost, chemical stability, high natural abundance and versatile potential applications (Carp et al., 2004; Ambrus et al., 2008).

For photocatalytic degradation process, two methods of TiO₂ application are favored: (1) TiO₂ suspended in aqueous media and (2) TiO₂ immobilized on suitable support material. Although suspended photocatalyst systems always give higher degradation rates, there is one obvious problem arising from it. Basically, the particle size of catalyst powders synthesized by the industry is in the range of 30–200 nm. Therefore, the reactor must be equipped with a liquid–solid separator, which increases the costs of the whole process. The second problem arising from a suspension system is that the fine solid particles from the effluent may cause turbidity in the downstream. Taking into account the above problems and also from the economic point of view, immobilization of photocatalyst seems to offer a plausible solution (Takeda et al., 1995, Gao et al., 2008, Tasbihi et al., 2007).

The supported TiO₂ is generally considered more practical due to its easier separation from treated water. It can be supported on various substrates such as glass beads (Tasbihi et al., 2007; Qui and Zheng, 2007), silica gel, quartz sand (Tasbihi et al., 2007), carbon nanotubes (Gao et al., 2008), glass slides (Guillard et al., 2002; Lavrenčič Štangar et al., 2006; Černigoj et al., 2007), fibreglass tissue (Enriquez et al., 2007), alumina, mordenite (Takeda et al., 1995), different types of zeolites (Takeda et al., 1995; Durgakumari et al., 2002; Shankar et al., 2006), activated

carbons (Li Puma et al., 2008; Takeda et al., 1995) and mesoporous materials (Busuioc et al., 2006; Grieken et al., 2002; Lopez–Munoz et al., 2005).

2.2. Synthesis processes of TiO₂

TiO₂ can be prepared in the form of powder, crystals or thin films. Both powders and films can be built up from crystallites ranging from a few nanometers to several micrometers. It should be noted that nanosized crystallites tend to agglomerate. If separate nanosized particles are desired, often a deagglomeration step is necessary. Many novel methods lead to nanoparticles without an additional deagglomeration step (Carp et al., 2004).

It is important to mention that the physical and chemical properties of TiO₂ are strongly dependent on the preparation method. Basically, there are two different routes of preparation, i.e. gas–phase methods and solution methods. Among gas–phase methods, the main techniques are chemical vapour deposition (CVD), physical vapour deposition (PVD) and spray pyrolysis deposition (SPD). The solution methods include solvothermal method, precipitation method, microemulsion method, combustion synthesis, electrochemical synthesis and sol–gel method (Carp et al., 2004). Among these synthesis methods, sol–gel process is the method used very often due to the several advantages which are explained below.

2.2.1. Sol–gel process

The sol–gel process allows to obtain of solid products by gelation rather than by crystallization or precipitation. It can be described as the creation of an oxide network by progressive polycondensation reactions of molecular precursors in a liquid medium, or as a process to form materials via a sol, gelation of the sol and finally removal of the solvent. This method is considered as “chimie douce” or soft chemical approach to the synthesis of metastable oxide materials (Schubert and Hüsing, 2005).

The terms “sol” and “gel” are being defined as (Schubert and Hüsing, 2005):

A “sol” is a stable suspension of colloidal solid particles or polymers in a liquid. The particles can be amorphous or crystalline.

A “gel” consists of a porous, three-dimensionally continuous solid network surrounding and supporting a continuous liquid phase (“wet gel”). In “colloidal” (“particulate”) gels, the network is made by agglomeration of dense colloidal particles, whereas in “polymeric” gels the particles have a polymeric sub-structure made by aggregation of sub-colloidal chemical units.

Figure 3 presents a scheme of the different process routes leading from the sol to a variety of materials. Powders can be obtained by spray-drying of a sol. Gel fibers can be drawn directly from the sol, or thin films can be prepared by standard coating technologies such as dip- or spin-coating, spraying, etc. Here, gelation occurs during the preparation of the film or fiber due to rapid evaporation of the solvent (Schubert and Hüsing, 2005).

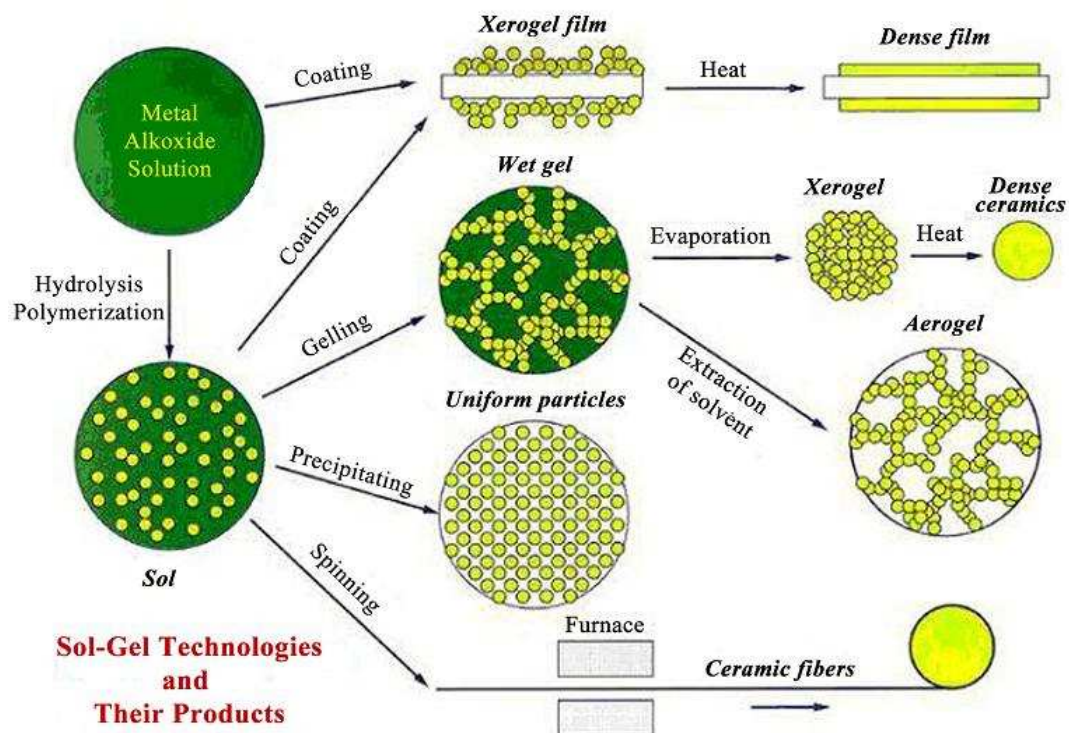


Fig 3: Scheme of the sol-gel processing options (Brinker and Scherer, 1990)

Gelation can also occur after a sol is cast into a mold, in this case it is possible to make a monolith of a desired shape. Drying by evaporation of the pore liquid gives rise to capillary forces that causes shrinkage of the gel network. The resulting dried gel is called a xerogel. Compared to original wet gel its volume is often reduced by factor 5–10. Due to the drying stress, the monolithic gel is often destroyed and powders are obtained. When the wet gel is dried in a way that the pore and network structure of the gel is maintained even after drying, the resulting dried gel is called an aerogel. Dense ceramics or glass can be obtained after heat treatment of xerogels or aerogels to a temperature high enough to cause sintering (Schubert and Hüsing, 2005).

Typical applications of sol–gel materials include all kinds of coatings, catalysts and catalyst supports, ceramic fibers, electroceramic powders, insulating materials, high-purity glasses, etc. The many processing options allow unique access to multicomponent oxide systems (Schubert and Hüsing, 2005).

A number of reasons to choose the sol–gel route for the synthesis of materials are apparent (Brinker and Scherer, 1990):

(i) The chemical conditions are mild. Hydrolysis and condensation are catalyzed by acids and bases, but extreme pH conditions can be easily avoided, especially by the use of two step methods in which acid catalyzed hydrolysis is followed by rapid neutralization or buffering. In this way pH sensitive organic species (e.g. dyes) and even biological species including enzymes and whole cells may be entrapped and still retain their functions.

(ii) Highly porous materials and nanocrystalline materials may be prepared in this way.

(iii) By appropriate chemical modification of the precursors, control may be achieved over the rates of hydrolysis and condensation, and over colloid particle size and the pore size, porosity and pore wall chemistry of the final material.

(iii) By controlling ageing and drying conditions, further pore size and mechanical strength control may be achieved.

Two processing routes of the sol–gel method are known: the non–alkoxide (inorganic) and the alkoxide (organic) route. The non–alkoxide route uses inorganic salts (such as nitrates, chlorides, acetates, carbonates, acetylacetonates, etc.) and requires an additional removal of the inorganic anion, while the alkoxide route (the most usually employed) uses metal alkoxides as starting material (Carp et al., 2004).

As precursors for titanium dioxide, inorganic compounds such as TiCl_4 , TiCl_3 , $\text{Ti}(\text{SO}_4)_2$ are easily available and more economical than alkoxides (Zhang et al., 1999; Nag et al., 2007).

In the preparation temperature point of view, sol–gel process is divided in two different categories: high–temperature preparation (using calcination treatment) and low–temperature preparation (crystallinity is achieved without calcination treatment).

2.2.1.1. Low–temperature sol–gel process

In the past, by the usual sol–gel chemistry in water–rich solvent mixtures, only amorphous titania could be synthesized which does not possess the desired electronic properties (Hu et al., 2008). Most of the research works usually employed the precalcined titanium dioxide at around 300–400 °C to induce crystallization of the anatase form (Kanna and Wongnawa, 2008). Although further heating at higher temperatures would activate the material into highly crystalline structure, excessive thermal energy often leads to the collapse of mesoporous frameworks accompanied by loss of surface area, increasing the particle size and particle agglomeration. The agglomeration and precipitation of TiO_2 powder particles in aqueous suspension can reduce the active sites on TiO_2 surface significantly. One way to obtain non aggregated (separated) particles is immobilized titania using porous materials (Wu et al., 2005).

Liu et al. (2008a, 2008b) prepared TiO_2 hydrosols by chemical precipitation–peptization method from titanium sulfate and metatitanic acid under various

peptizing conditions. The optimized peptizing conditions were determined and the properties of the sols were correlated with their photocatalytic activities. The TiO₂ sols or particles prepared at low temperature (< 100 °C) have several advantages such as (1) finer particle size with more uniform distribution and better dispersion in water; (2) stronger interfacial adsorption ability; and (3) easy coating on various supporting materials. In fact, the photocatalytic activity and transparency of TiO₂ sols depend on some factors such as their crystal phase, degree of crystallization, and particle size.

Lee and Liu (2002) synthesized crystalline TiO₂ sol at low temperature using acid-hydrolysis method. Acid-hydrolysis method was developed in order to avoid calcination at high temperature. TiCl₄ was used as a starting material and HCl as a peptizing agent. The HCl was added to a gel of hydrated titanium oxide to dissolve it. pH value, [H⁺]/[Ti] ratio, HCl concentration, storage temperature and hydroxypropyl cellulose as dispersant were investigated as preparation parameters, but no photocatalytic tests were performed.

Randorn et al. (2004) prepared hydrated titanium dioxide using TiCl₄ and concentrated NH₃ solution without calcination. The compositions of the prepared powders were mostly of an amorphous form with a small amount of anatase mixed in. The photocatalytic decomposition of methylene blue was investigated. The activity was inferior to Degussa P25 if adsorption is excluded.

Addamo et al. (2005) prepared nanostructured TiO₂ sols by controlling the hydrolysis of TiCl₄ in very mild experimental conditions without heat treatment. The properties of the samples depended on TiCl₄/H₂O ratio, procedure of preparation and boiling time. It was shown that the photoactivity of the samples mainly depended on a compromise between crystallinity and particle size.

Low-temperature synthesis (< 100 °C) of crystalline oxide particles eliminates the need for high temperature operations, what is beneficial from economical point of view, since elimination of calcination step means lower cost due to the less energy consumption and shorter time between the synthesis and application point (Kanna and Wongnawa, 2008; Randorn et al., 2004, Addamo et al., 2005). The main

problem of low-temperature preparation routes is low crystallinity and consequently low photocatalytic activity of the obtained samples (Kanna and Wongnawa, 2008).

2.3. Support (for the photocatalyst)

In classical heterogeneous catalysis, the active material (often a metal, an oxide, or a sulfide) is usually in the form of small particles, typically in the nanometer range. The reason for this small size is very simple: the chemistry occurs on the surface of the particles and for a given mass, the surface area that is developed by a particulate material increases as the particle size decreases. Thus a high dispersion rate (a small particle size) is beneficial to the chemical activity per unit mass of material. Unfortunately, a highly dispersed state is fundamentally an unstable state of matter, because the surface tension (which has units of force per unit length or, equivalently, energy per unit surface) tends to favor the states of smallest interface area per unit mass. This is especially true at high temperature when the atomic and particulate diffusion rates allow sintering and particle growth. A common way of limiting these phenomena is to support the highly dispersed active phase on a matrix. Thanks to its porous micro texture and/or to interfacial interactions, the support keeps the active phase in the dispersed state in a temperature range and in a gaseous or liquid environment where sintering would otherwise occur. In addition to this physical role, the support often interferes either directly or indirectly in the reaction mechanism via the active phase-support interactions. Strong metal support interactions may lead to epitaxial growth of particles with unusual morphologies. Electronic interactions between a dispersed metal and insulating or semiconducting supports may also modify the catalyst behaviour (Serpone and Pelizzetti, 1989).

All this shows that the concept of support covers numerous physical and/or chemical functionalities. This is even more pronounced in photocatalysis. Photocatalysis is, in the overwhelming majority of cases, a bi- or even multifunctional process. The following functions may be involved in a photocatalytic process (Serpone and Pelizzetti, 1989):

- 1- temporary adsorption or coordination of the substrate to be transformed;
- 2- absorption of light;
- 3- energy transfer to the substrate;

- 4– generation of elementary redox intermediates (which can be electrons and holes);
- 5– separation of the elementary redox intermediates, eventually via the generation of secondary redox intermediates;
- 6– reaction of the adsorbed or coordinated substrate (when the substrate goes through an excited state);
- 7– reaction of the substrate with at least one of the redox intermediates;
- 8– desorption or decoordination of the products.

All the above mentioned functions are not necessarily involved in a given photocatalytic process, but one can appreciate the number of possible combinations. In each of them, the concept of support covers a different reality. A few examples are sketched in Figure 4 (Serpone and Pelizzetti, 1989).

(a) In the simplest possible case one may consider, for instance, the photoisomerisation of a molecule, after absorption of light in the adsorbed state. In this case the support is merely an adsorbent, but it may influence the yield or the selectivity of the reaction by modifying the absorption spectrum of the substrate or by introducing conformational or chemical (acidity) constraints.

(b) In the same layer, one may consider the photolysis of a light-absorbing molecule in a microporous solid. In this case the support is not only an adsorbent. Microporous structure acts as a restricted geometrical environment, which introduces a cage effect and modifies the fragment recombination possibilities. Silicas and zeolites have been used in this way.

(c) Next in the sequence of Figure 4 is a case in which an adsorbed molecule undergoes a reaction induced by a sensitizer anchored to the surface, or by an electron-hole pair generated in a semiconductor support. The support is here an adsorbent as well as a photosensitizer. TiO_2 or ZnO belong to this class of supports in numerous oxidation and isomerization reactions. The photo-oxidation of organic species sensitized by adsorbed dyes belongs to the same rationale.

(d) An additional function is included in the system when the reaction requires a dispersed metal in order, for instance, to generate molecular hydrogen by reverse

hydrogen spillover. Pt/TiO₂ in the dehydrogenation of alcohols belongs to this class. TiO₂ adsorbs the alcohol, supports the platinum, and absorbs light.

(e) A further step is made when two types of dispersed catalysts are required, each catalyst taking charge of a redox reaction, for instance. This situation is encountered in the splitting of water with RuO₂/TiO₂/Pt.

(f) The "ultimate" level of integration with a multifunctional catalyst based on a semiconductor support is probably achieved when the surface of the semiconductor is derivatized with a molecular sensitizer. RuO₂/TiO₂ system is probably the only example of this type.

(g) Derivatization (i.e. covalent linkage) or ionosorption (strong adsorption by ion exchange) can also be used to heterogeneous homogeneous catalysts. Colloidal clay supports have been used for this purpose, with water oxidation catalysts.

(h) A special function involved in redox photocatalysis, which is often devoted to the support, is the so-called separation of charges (i.e. the slowing down of the "recombination" reaction of the primary redox intermediates generated by the sensitizer). This can be achieved either within the internal (electronic) space charge region of a semiconductor support, when one deals with electrons, holes, or both, or within the external (ionic) space charge region (diffuse double layer) of a charged insulator support, when one deals with ions in a polar liquid.

In fact, there is no well-defined limit to the number of duties that one may ask a support to perform. When several molecular and (or) finely dispersed particulate species are linked to a support, the system is best regarded as an organized assembly and the support is nothing else than a structuring matrix, at a supramolecular level (Serpone and Pelizzetti, 1989).

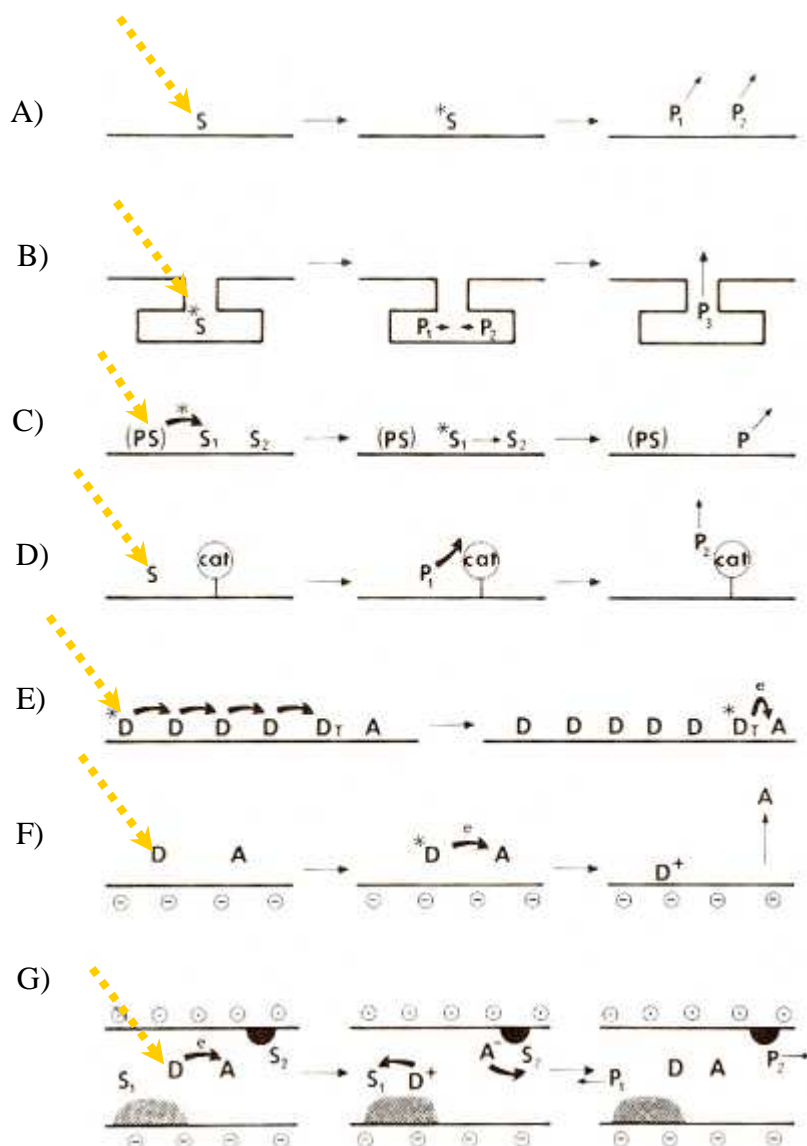


Fig 4: Schematic illustration of several functions assigned to a support in a photocatalytic system. In Figure 4 symbols are as follows: S or Si are substrates to be transformed; P or Pi are final or intermediate products ($i = 1$ or 2); PS stands for photosensitizer; D and A are energy or electron donors and acceptors, respectively. The functions that are represented are (A) adsorption of the substrate; (B) adsorption of the substrate and intermediate products in a restricted geometry; (C) anchoring a photosensitizer; (D) anchoring a molecular catalyst; (E) organizing a molecular assembly for energy transfer toward a reaction center; (F) separating redox intermediates by double-layer effects; (G) organizing a bifunctional catalytic system, with two dispersed metal or oxide catalysts (Serpone and Pelizzetti, 1989).

Based on these criteria, silicate porous materials have been already extensively studied and used as a highly structured support with dispersed photocatalytic material in its restricted geometrical environment (case b of support concept).

2.3.1. Porous materials

After approximately 50 years of intensive research on the development of inorganic molecular sieves, the porous materials have recently gained a firm position in materials science. Based on their unique molecular dimensions and high surface areas and porosities, they find important applications in the field of adsorption and catalyst technology (Linssen et al., 2003).

A solid is porous when it contains pores, i.e. cavities, channels, or interstices (which are deeper than they are wide). In nature, many materials are porous, including wood, rock, sponge, bone, etc. The physical properties of the porous materials such as density, thermal conductivity, strength, etc., depend on the porosity and the pore structure of the solid. Furthermore, porosity is one of the factors that influence the chemical reactivity and the physical interaction of solid with gases and liquids (Schubert and Hüsing, 2005).

Porous material can be characterized by pore size. Generally, three different pore-size regimes are defined by IUPAC (International Union of Pure and Applied Chemistry): micropores (pore diameter smaller than 2 nm), mesopores (pore diameter between 2 and 50 nm) and macropores (pore diameter larger than 50 nm) (Schubert and Hüsing, 2005).

Mesoporous silica nanoparticles (MSNs) were first synthesized in 1990 by Japanese scientists (Yanagisawa et al., 1990). Later on, in 1992, Mobil Oil Corporation researchers developed the MCM (Mobil Composition of Matter) family of the surfactant-templated ordered mesoporous materials (OMMs) with the high surface area and narrow pore size distribution (1.5 to 10 nm) (Bagshaw et al., 1995). Among OMMs with the different framework compositions, ordered mesostructured silicates (OMSs) are particularly synthesized using a variety of synthesis procedures, including cost-effective ones, and they have attractive properties such as high specific surface area, large mesoporous volume, adjustable pore diameter, narrow pore size distribution and tailorable surface properties. OMSs are desirable in numerous applications as they can serve as catalysts, or catalyst supports, adsorbents, components for sensors, chromatographic packing, media for immobilization of biomolecules and materials with wholesome optical and magnetic properties (Landau

et al., 2005; Celer et al., 2006). Unfortunately their hydrothermal stability was quite poor both in steam at high temperatures and in hot water. This deficiency is one of the major factors that hinder prospective applications of OMSs in petrochemical processing. Over the last several years, much research has been devoted to the identification of conditions suitable for the direct synthesis of hydrothermally stable OMSs and to the development of methods for an effective post-synthesis stabilization of OMSs.

2.3.1.1. Well-ordered mesoporous silica materials (SBA-15 type)

In 1998, Zhao et al. at the University of California in Santa Barbara reported that they had produced silica nanoparticles of well-ordered mesoporous structure with tunable large uniform pore sizes varying from 5 to 30 nm. The material was denoted Santa Barbara Amorphous (SBA) type material. The SBA-n (n = 1-3, 8, 11, 12, 14-16) family was synthesized under acidic media using different nonionic surfactants. The synthesis is based on employing triblock copolymer and oligomer templates as organic structure-directing agents. The poly(alkylene oxide) triblock copolymers such as poly(ethylene oxide)-poly(propylene oxide)-poly(ethylene oxide) (PEO-PPO-PEO) were found to be good candidates due to their mesostructural ordering properties, amphiphilic character, low cost, commercial availability, nontoxicity and biodegradability. SBA-15 has highly ordered two-dimensional (2D) hexagonal ($P6mm$) pore structure similar to MCM-41 (Zhao et al., 1998). This material with tunable large uniform pore sizes had a thicker silica walls and greater hydrothermal stability compared to MCM-41.

In general applications, SBA-15 shows desirable properties due to the various advantages such as chemical inertness, transparency to the UV radiation, no photoactivity, high specific surface area, easy synthesis, narrow pore size distribution, high pore volume and in particular thick amorphous silica walls and superior hydrothermal stability (Zhao et al., 1998; Jung et al., 2008; Perathoner et al., 2006; Yang et al., 2006).

In specific applications, SBA-15 is talented for the manufacturing of waveguides, mirrorless lasers, fast response photochromic mesostructures, superradiant fluorescent nanomaterials and sensing devices (Kruk et al., 2003).

After successful preparation of mesoporous SBA-15, some efforts have been made to crystallize the pore walls of mesoporous materials in order to provide them with the specific functionality. The generation of the microprosity within the amorphous pore walls of mesoporous materials was a promising strategy for providing them with the particular functionality. Such a material possesses a bimodal pore system, in which micropores exist within the walls of mesopores. It is an ideal porous material for catalysts and adsorbents, because molecules are first transported through mesopore channels and then strongly adsorbed in the micropores. These SBA-15 silicates referred to as plugged hexagonal templated silicate materials (PHTSs).

Although before 2000 there had been some reports suggesting microprosity within the pore walls of MCM-41 (Long et al., 1998) and SBA-15 (Kruh et al., 2000), a systematic study for confirmation and control of the microprosity within the pore walls of an ordered mesoporous material has not been reported. In 2000 Miyazawa and Inagaki (2000) developed microprosity within the pore walls of ordered mesoporous silica SBA-15 by controlling the synthesis temperature and the silica/surfactant ratio in the starting mixture in order to optimize the ratio of micro- to mesopores in SBA-15 materials. They used a triblock copolymer, Pluronic P104 (BASF), $\text{EO}_{17}\text{PO}_{58}\text{EO}_{17}$ ($\text{EO} = -\text{CH}_2\text{CH}_2\text{O}-$, $\text{PO} = -\text{CH}_2\text{CH}(\text{CH}_3)\text{O}-$), as a structure-directing agent for the synthesis of these materials. PHTS has the same 2-D hexagonal symmetry as SBA-15, but some of its cylindrical mesopores have internal porous plugs, while others are open as inferred from gas adsorption-desorption data.

Afterwards, in 2002, Van der Voort et al. (2002) proposed the fast and easy synthesis of stable composite materials, with combined micro- and mesoprosity and large pore volumes. The high micropore volume and high stability of these PHTS materials is governed by internal silica nanocapsules. In the initial synthesis step, they dissolved Pluronic P123 ($\text{EO}_{20}\text{PO}_{70}\text{EO}_{20}$) and tetraethyl orthosilicate (TEOS) in various ratios in a 2 M HCl solution. PHTSs materials were found to exhibit a remarkable hydrothermal and mechanical stability that was much higher than that of SBA-15 silica synthesized using a typical procedure. The 77 K nitrogen adsorption-desorption isotherms of three distinctly different samples are shown in Figure 5.

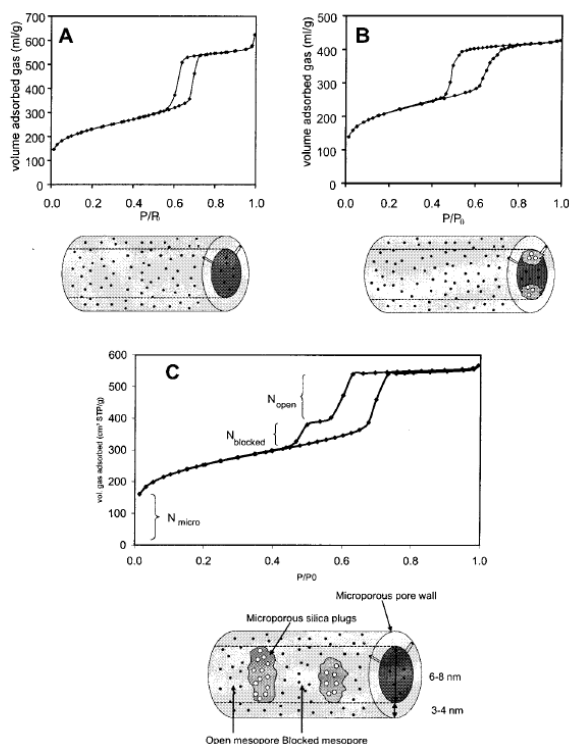


Fig 5: Nitrogen adsorption–desorption isotherms of (A) pore system with completely open mesopores and intrawall micropores (SBA–15); (B) pore system with blocked mesopore openings (ink–bottle pores) and intrawall micropores (PHTS–3); (C) “plugged” mesopores, comprising both open and blocked mesopores, intrawall micropores, and microporous silica nanocapsules (PHTS–2) (Van der Voort et al., 2002).

2.3.1.2. Foam–like (disordered) mesoporous silica materials (KIL–2 type)

The novel foam–like mesoporous silica materials defined as KIL were synthesized by the researchers at the National Institute of Chemistry in Ljubljana. The materials were named as KIL family of materials, which is a denotation for Kemijski Inštitut Ljubljana. The KIL–2 family is related to mesostructured silicate families with textural porosity (HMS, MSU, NBS) (Fuertes, 2004; Haskouri et al., 2008; Tuel, 1999). KIL–2 materials possess interparticle mesopores with pore dimensions between 5 and 60 nm and surface area between 450 to 550 m² g^{–1}. The mesopores are formed by the aggregation of silica nanoparticles thus creating network with interparticle voids. The controllable two–step synthesis was developed (Novak Tušar et al., 2010). In the first step the synthesis strategy of KIL–2 is based on the neutral templating method (Tuel, 1999) in which small, non–surfactant templates such as triethanolamine (TEA) direct the polycondensation of inorganic species (Jansen et al., 2001). After the polycondensation of silicate species, the gel is aged at relatively low aging temperature of 50 °C. Such a low temperature leads to larger silicate particles. In the second step the gel was treated solvothermally in ethanol. This step

is crucial because it determines the size of the pores. By calcination of the product at 500 °C for 10 h, triethanolamine is removed and thermal stability of the product is verified. Treatment of the product in boiling water proves that the obtained material is also hydrothermally stable. The particle size and the pore diameters depend on the temperature of the ageing step (first step) and on the solvothermal treatment in ethanol (second step), respectively. The synthesis procedure is simple and reproducible. The nitrogen adsorption–desorption curve of KIL–2 is shown in Figure 6. The shape of a gas adsorption isotherm reveals a qualitative structural information. The nitrogen adsorption–desorption isotherm for the sample studied was typical type–IV isotherm (Sing et al., 1985) with a steep increase of adsorption branch at p/p_o of 0.85–0.95 corresponding to capillary condensation within framework mesopores and textural large pores. A hysteresis loop exhibits parallel and nearly vertical branches and it does not level off at relative pressures close to the saturation vapor pressure. This kind of hysteresis loop was often reported for materials with large cylindrical pores and that ones consisted of aggregates (Kruh and Jaroniec, 2001). Textural large pores or interparticle pores arise from the aggregation of small fundamental particles. The textural porosity is typical for HMS framework structure (Zhang et al., 1997) and it is dependent on the size, connectivity, and surface texture of the fundamental particles. HMS structures have < 200 nm small fundamental particles which result in complementary textural mesoporosity for providing a more efficient transport of reagents to framework reaction centers (Zhang et al., 1996; Zhang et al., 1997).

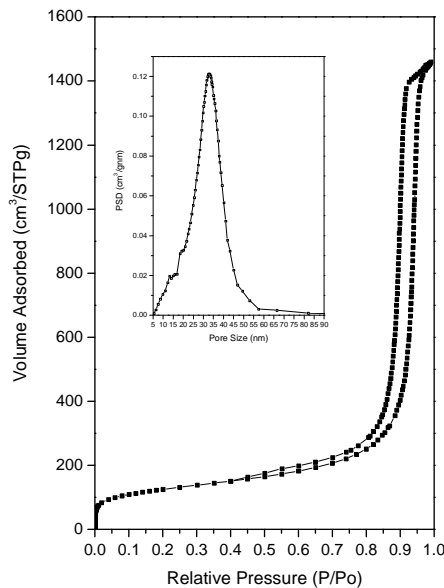


Fig 6: Nitrogen sorption isotherm with pore size distribution curve (inset) of KIL-2 (Novak Tušar et al., 2010)

2.4. Techniques for depositing TiO₂ into/onto porous material

Considering the application of mesoporous materials as catalysts and adsorbents, it is desirable to introduce active sites in the mesoporous channels or on the mesoporous surface (Zhang et al., 1996). Incorporation of transition-metal ions into the frameworks of the molecular sieves is a general method for introducing catalytic sites into mesoporous materials. So far, numerous attempts have been made to prepare transition metal-substituted mesoporous molecular sieves for making them into effective catalysts which are capable of treating large molecules (Chen et al., 2004).

For using TiO₂ as a photocatalyst, poor adsorption and relatively low surface area properties lead to great limitations in exploiting the photocatalyst to the best of its photoefficiency. Several attempts have been made to improve the photoefficiency of titania by depositing it on adsorbents like silicate materials, alumina, zeolites, clays and active carbon (Takeda et al., 1995; Durgakumari et al., 2002; Shankar et al., 2006; Busuioc et al., 2006; Grieken et al., 2002; Lopez-Munoz et al., 2005; Pozzo et al., 2000).

Titanium-containing molecular sieves have attracted much attention in past decades, since titanium silicate-1 (TS-1) molecular sieve have shown excellent activities for

the selective oxidation of a variety of organic compounds by using hydrogen peroxide as oxidant. This increased adsorption capacity is the result of the large specific surface area produced by incorporation of TiO₂ particles inside the silicate layers, creating a mesoporous structure. In this respect, incorporation of titania particles into mesoporous materials has been the subject of many practical application and research work (Chen et al., 2004).

In the last few years, many techniques for depositing TiO₂ have been investigated using different porous materials for the photocatalytic degradation reaction in liquid and gas phase media. The methods of synthesizing titania–silica mixed oxides include grafting titania on silica support and fabricating titania–silica composites. The titania–silica composite can be synthesized by homogeneous mixing of suitable precursors, whereby Ti atoms are incorporated in the silica structure during formation of the silica support itself. In contrast to the former supported oxides, Ti can be introduced in a post–synthesis step, by which a titanium precursor is deposited onto the silica surface by grafting methods, precipitation or impregnation followed by solvent evaporation (Yang et al., 2006).

The most used methods involve incipient–wetness impregnation (Luan and Kevan, 2001; Luan et al., 1999), one– or multi–step impregnation (De Witte et al., 2007; Wang and Song, 2006) and post–synthesis deposition using the acid–catalyzed sol–gel method (Busuioc et al., 2006; De Witte et al., 2007).

In the incipient–wetness impregnation method, the active metal precursor is dissolved in water or organic solvent. Then the metal–containing solution is added to a catalyst support containing the same pore volume as the volume of solution that was added. Capillary action draws the solution into the pores. The catalyst can then be dried and calcined to drive off the volatile components within the solution, depositing the metal on the catalyst surface. Luan et al. (1999, 2001) incorporated titania into mesoporous silica molecular sieve SBA–15 via incipient–wetness impregnation with various stoichiometric Ti/Si molar ratios in the range from 0.025 to 0.2. The results show that titania is present in two distinct chemical forms and their relative amounts depend on the titania loading. At the low loading, the guest Ti–phase is monoatomically dispersed as titanium ions on the SBA–15 wall surface

and the pore size of SBA-15 is not altered, whereas at high titanium loading a titanium dioxide anatase film is formed as a thin film anchored inside the mesopores of SBA-15.

In multi-step impregnation method the loading procedure of metal oxide materials is repeated for more than once to integrate higher amount of titania. Wang and Song (2006) incorporated high amount of titania into the mesoporous SBA-15 by employing multistep impregnation method. They found very small titania nanodomains up to 1.3 nm instead of bulk titania phases by wide-angle XRD, Raman and UV-vis diffuse reflectance spectra. They suggested that multistep impregnation method is more effective to incorporate high amount of titania compared to one-step impregnation method.

Landau et al. (2005) inserted TiO₂ (30–80 wt. %) inside the pores of SBA-15, with the minimum pore blocking by chemical solution decomposition and internal hydrolysis. Both methods yielded composites with high (85–94 %) TiO₂-anatase crystallinity. The nanocrystal structure of TiO₂/SBA-15 composites did not change by calcination up to 800 °C while the crystal domain size increased slightly.

Perathoner et al. (2006) studied the characteristics of TiO₂/SBA-15 materials with loading of TiO₂ below 15 wt. %. The SBA-15 was grafted with Ti-isopropoxide in different organic solvents. They found out that the pre-treatment of the SBA-15 before the grafting with titania and the solvent used in the preparation have some influence on the relative distribution of various titania species, affecting the concentration of hydroxyl groups and of defects. However their results indicate that this could be considered as a minor effect. They confirmed that introducing by grafting, titanium reacts with silanol groups in the corona area of inner SBA-15 walls forming either TiO₄ tetrahedral sites and/or pseudo-octahedral surface sites anchored by two (or more) Si or Ti ions through bridging oxygen. In the region of high silanol density, where the micropores are located in the corona of SBA-15 channels, this reaction leads reasonably to the formation of TiO₂-like nanoareas with the dimensions of around 1–2 nm not detected by XRD but evidenced from the UV-vis spectroscopy. Their characterization results showed that there is no formation of

separated anatase phase and the distribution of Ti within the samples is homogeneous.

Busuioc et al. (2006) synthesized TiO₂/SBA-15 by the post synthesis deposition using the acid-catalyzed sol-gel method. They showed that by changing the initial amount of Ti-isopropoxide, pH and temperature for formation of TiO₂ sol, the size, the location and the amount of the anatase nanoparticles on SBA-15 could be controlled. By confining TiO₂ nanoparticles into SBA-15 the growth of these nanoparticles is controlled and the size could be tuned to few nanometers only, resulting in an improved adsorption capacity and photocatalytic activity towards photodecomposition of dye (rhodamine 6G) in aqueous solution compared with pure TiO₂.

2.5. Organic contaminants

Organic chemical contamination is a widespread problem around the world and can commonly be a contamination factor virtually at every corner of our environment including soil, groundwater, surface water, plants, and our bodies. Industrial processes generate a variety of molecules that may pollute air and waters due to negative impacts such as toxicity, carcinogenic and mutagenic properties for ecosystems and humans (Busca et al., 2008; Lim et al., 2008; Tomasic et al., 2008).

Volatile organic compounds (VOCs) are organic chemical compounds that have high enough vapour pressures under normal conditions to vaporize significantly and enter the atmosphere. A wide range of carbon-based molecules, such as ketones and other light hydrocarbons are VOCs. According to European Union legislation, a VOC is any organic compound having an initial boiling point roughly in the range of 50 to 250 °C measured at a standard atmospheric pressure of 101.3 kPa (Lim et al., 2008).

Many VOCs are human-made chemicals that are used and produced in the manufacture of paints, pharmaceuticals and refrigerants. Typically, VOCs are industrial solvents such as trichloroethylene, fuel oxygenates such as methyl tert-butyl ether, or by-products produced by chlorination in water treatment such as chloroform. VOCs are often components of petroleum fuels, hydraulic fluids, paint

thinners and dry cleaning agents. VOCs are also common ground–water contaminants (Tomasic et al., 2008).

VOCs are emitted as gases from certain solids or liquids. VOCs include a variety of chemicals, some of which may have short– and long–term adverse health effects. Concentrations of many VOCs are consistently higher indoors (up to ten times higher) than outdoors.

2.5.1. Phenol

Phenol as a VOC (boiling point = 181.75 °C) is one of the most common organic contaminant, because of its toxicity even at low concentrations and because it could be further transformed to the substituted compounds during disinfection and oxidation processes in natural waters (Busca et al., 2008).

Phenol was first isolated from coal tar in 1834 by the german chemist Runge. This aromatic compound is a hygroscopic crystalline solid. When pure, solid phenol is white but is mostly colored due to the presence of impurities. Phenol is very soluble in ethanol, in ether and in several polar solvents, as well as in hydrocarbons such as benzene. In water it has a limited solubility and behaves as a weak acid. Phenol and substituted phenols are found as contaminants in waste water produced in pesticide, paint, pharmaceuticals, coal processing, paper and pulp industries (Lin et al., 1995).

The oxidative degradation of phenol and its derivatives has been widely studied at the laboratory scale (Sobczynski et al., 2004). Figure 7 shows a possible oxidation pathway in the presence of illuminated TiO₂ in a photocatalytic process.

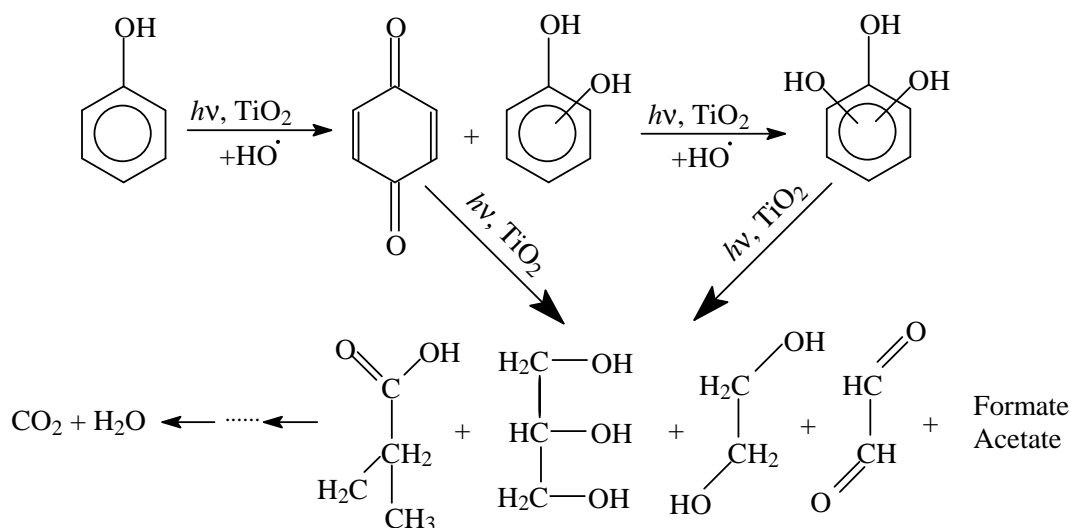


Fig 7: A possible mechanism of phenol destruction and mineralization on illuminated TiO₂ (Sobczynski et al., 2004)

2.5.2. Toluene

Toluene, also known as methylbenzene (boiling point = 110.6 °C) is a clear water-insoluble liquid with the typical smell of paint thinners, reminiscent of the related compound benzene. It is an aromatic hydrocarbon that is widely used as an industrial feedstock and as a solvent.

Toluene is usually used as a model VOC for gaseous system, because it belongs to BTEX (Benzene, Toluene, Ethylbenzene and Xylene), a major group of pollutants frequently encountered in indoor air in different countries (Jones, 1999). Moreover, toluene has been classified as one of the eight representative indoor VOCs by the proposed ASHRAE (American Society of Heating, Refrigerating and Air-Conditioning Engineering) test method for determining the efficiency and capacity of gas-phase air cleaning systems for indoor air applications (Chen et al., 2005).

Toluene is one of the major indoor and industrial air pollutants; therefore several strategies have been identified in order to reduce its presence in civil and industrial emissions. It is widespread reagent used for preparation of many compounds such as chloro derivatives, benzyl alcohol, benzaldehyde and benzoic acid (Augugliaro et al., 1999).

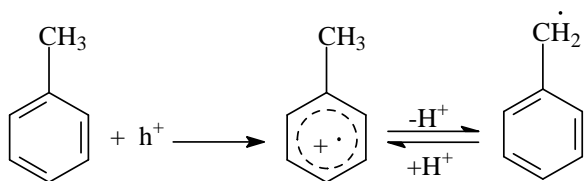
Among the methods to oxidize toluene, heterogeneous photocatalysis is one of the most attractive method due to the mild experimental conditions (Prieto et al., 2007; Kuo et al., 2009; Sekiguchi et al., 2008).

For the first time in gas–solid photoreaction regime, Ibusuki and Takeuchi (1986) investigated photo–oxidation of toluene in trace amounts (80 ppm) in air in the presence of water vapor at room temperature by using UV irradiated TiO₂. They used four photoreactors in series and the main product of the reaction at 10 min residence time was CO₂ with the trace (< 2ppm) of benzaldehyde as the only detected gas–phase intermediate. Water appears to be required for reaction while no reaction products or decrease of toluene concentration were detected in a toluene–dry air system, so the presence of water was crucial in order to achieve the almost complete photo–oxidation of toluene.

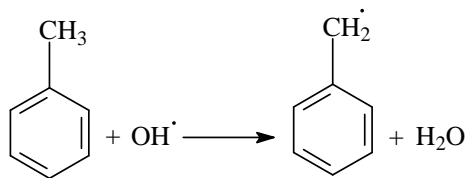
There are two kinds of hydrogen atom in a toluene molecule: one is in the methyl group, the other is in the aromatic ring.

1) If oxidation of toluene takes place on the methyl group: then according to the degradation pathway suggested by D’Hennezel et al. (1998) and Guo et al. (2008), two initial routes are suggested for the formation of benzyl radical.

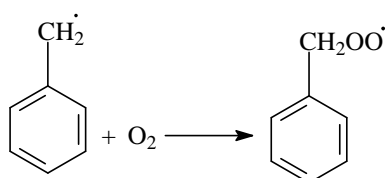
A) Direct hole transfer to toluene (in fact, it is an abstraction of an electron from toluene molecule). A mechanism in thermal heterogeneous catalysis of toluene oxidation proposed by Andersson (1986) shows that the first step is the reversible transfer of one electron from toluene to the metal oxide with the formation of an aromatic radical cation. This most probably slow, rate–determining step is followed by a faster proton release by the radical cation to form the benzyl radical.



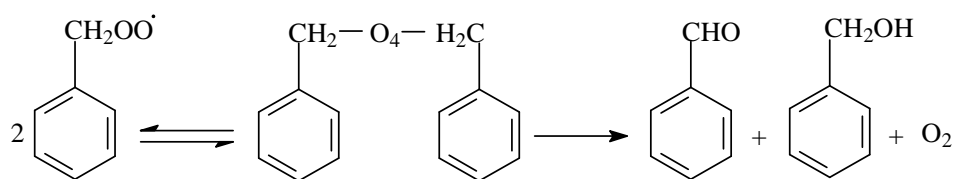
B) Abstraction of hydrogen atom (H) by a hydroxyl radical. This is considered to be minor pathway (D'Hennezel et al., 1998).



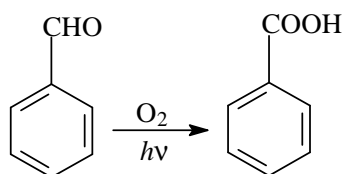
The surface benzyl radical can then react with O_2 to form benzylperoxy radical, or with an incoming toluene molecule, thus initiating a polymerization reaction as proposed by Sitkiewitz and Heller (1996) for benzene photocatalyzed conversion (Sitkiewitz and Heller, 1996):



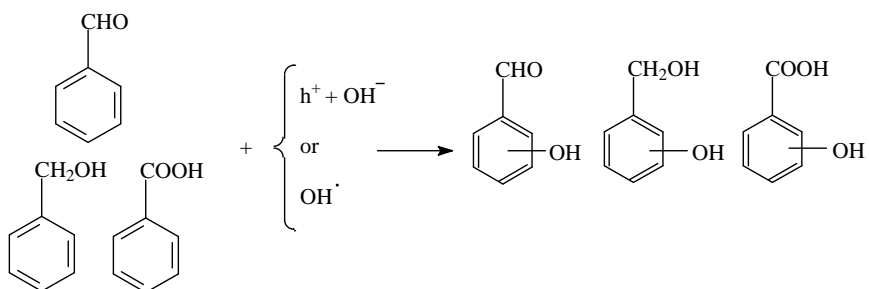
The benzylperoxy radicals can couple to form a tetroxide proposed by Sonntag and Schuchmann (1991) for oxidation of toluene in aqueous phase. The tetroxide decomposes to benzaldehyde, benzyl alcohol and O_2 :



Benzaldehyde is oxidized easily into benzoic acid in the presence of O_2 and UV irradiation (D'Hennezel et al., 1998):



2) If the oxidation of toluene takes place on the aromatic ring: it is accepted as a minor reaction pathway and takes place simultaneously with the methyl group oxidation. The degradation reactions lead to three main intermediate products: hydroxybenzaldehyde, hydroxybenzoic acid and hydroxybenzyl alcohol (D’Hennezel et al., 1998; Guo et al., 2008).

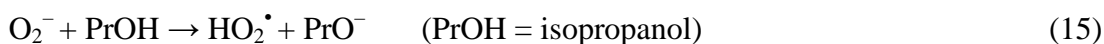


2.5.3. Isopropanol

Isopropanol (also propan-2-ol, 2-propanol or i-PrOH) is one of the most widely used solvents in the world. The second largest use of i-PrOH is as a chemical intermediate. It is also found in many everyday products such as paints, inks, general-purpose cleaners, disinfectants, room sprays and windshield deicing agents.

Photocatalytic degradation of gaseous isopropanol is a good model system because the initial reaction pathway involves almost exclusively the partial oxidation to acetone (Ohko and Fujishima, 1998).

Bickley et al. (1973) suggested the following mechanism for photocatalytic degradation of isopropanol in the gaseous phase at room temperature under UV irradiation in the presence of O₂ gas:

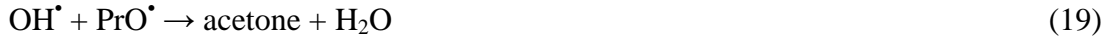
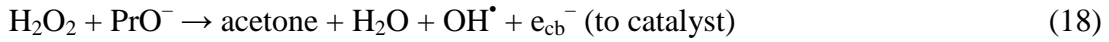


or as an H-atom transfer:



So that either of the two following pathways may then occur:

Pathway (A):



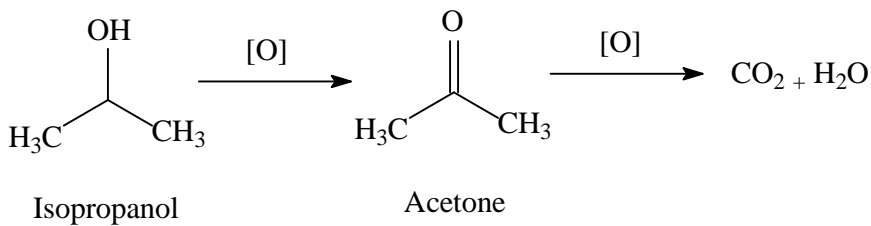
Pathway (B):



Both pathways involve two molecules of isopropanol, one of which reacts as a radical and another as an anion. In either case the overall reaction is the same, namely:



or a simplified reaction if we consider the whole mineralization:



2.6. Photoreactor concepts

One of the aims of modern chemical engineering research is the development of photoassisted processes, as the utilization of radiations has been an object of great interest in chemical process industries. In particular, improvements in UV technology have established an instrument that can be utilized for many purposes in chemical processing and especially for pollution control (Schiavello, 1988).

The development of water and air treatment systems based on heterogeneous photocatalysis is an area of major technical importance. There is general agreement that an important problem in the development of highly efficient photocatalytic reactors is the establishment of effective reactor designs for intermediate and large-scale use, as demanded by industrial and commercial applications. To achieve a successful commercial implementation, several reactor design parameters must be optimized, such as the photoreactor geometry, the type of photocatalyst and the utilization of radiated energy (De Lasa et al., 2005).

The engineering of photochemical reactor systems for the applications of AOPs refers to the basic principles of chemical reaction engineering; however, it has to take into account the particular concepts of photochemical engineering, which include the following substantial issues:

- (i) specific excitation of the reactive species;
- (ii) total absorbance of electromagnetic radiation to avoid unnecessary losses;
- (iii) radiation losses by reflection and scattering should be minimized;
- (iv) optimal oxygen saturation of the aqueous phase;
- (v) convergence of lamp and reactor geometry and the spatial separation between the lamp and the reaction mixture;
- (vi) efficient cooling of the lamp;
- (vii) precise description of the radiation distribution within the reactor volume considering the heterogeneity of the photochemical process;
- (viii) combination of this spatially defined energy absorption with the classical mass and energy system balances allows the description of the photoreactor/photochemical system (Oppenlander, 2003).

Photoreactors can be from application and industrial point of view divided into two different systems, aqueous systems and gaseous systems.

2.6.1. Photoreactors for water treatment

Classical chemical reaction engineering provides mathematical concepts to describe the ideal or real mass balances and reaction kinetics of commonly used reactor types that include discontinuous batch, mixed flow, plug flow, batch recirculation systems and staged or cascade reactor configurations (Levenspiel, 1999). The different reactor types for water treatment are shown schematically in Figure 8. All these reactors are amenable to photochemical reaction engineering. Many commercial photochemical reactor systems make use of the batch recirculation mode for the treatment of highly contaminated wastewaters of limited volume. On the other hand, cascades of photoreactor modules allow the gradual treatment of contaminated water streams with a very high photon flow in total (Oppenlander, 2003).

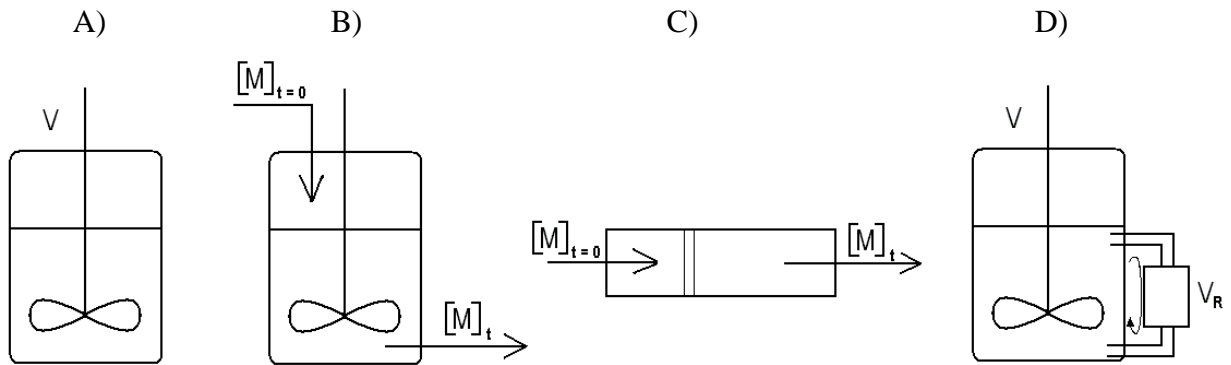


Fig 8: Types of ideal chemical reactors for water treatment: (A) batch reactor; (B) mixed flow reactor; (C) plug flow reactor; (D) batch recirculation reactor (Levenspiel, 1999)

Based on the manner in which the photocatalyst is used, all photocatalytic reactor configurations fall under two main categories regarding the shape of the solid phase (photocatalyst). The solid phase could be dispersed or stationary. Dispersed phase photoreactors may be operated with the catalyst particles and the fluid phase agitated by mechanical or other means. Depending on the means of agitation, the photoreactors resemble slurry or fluidized bed reactors. In numerous investigations, an aqueous suspension of the catalyst particles in immersion- or annular-type photoreactors has been used. In the case of stationary photocatalyst phase, the photocatalyst particles are immobilized onto a fixed transparent surface, such as the reactor wall or a fibre mesh, or are supported on particles, such as glass ceramic beads, that are held in fixed positions in the photoreactor (Mukherjee and Ray, 1999).

The summaries of the advantages and disadvantages of fluidized (slurry) and immobilized photocatalytic reactors systems are reported in Table 1 (De Lasa et al., 2005).

Table 1: Suspended versus immobilized photocatalytic systems

Fluidized (slurry) reactors	Immobilized reactors
<p>Advantages</p> <ul style="list-style-type: none"> • Fairly uniform catalyst distribution • High photocatalytic surface area to reactor volume ratio • Limited mass transfer • Well mixed particle suspension • Low pressure drop through the reactor 	<p>Advantages</p> <ul style="list-style-type: none"> • Continuous operation • Improved removal of organic material from water phase while using a support with adsorption properties • No need for an additional catalyst separation operation
<p>Disadvantages</p> <ul style="list-style-type: none"> • Requires post – process • Important light scattering and adsorption in the particle suspended medium 	<p>Disadvantages</p> <ul style="list-style-type: none"> • Low light utilization efficiencies due to light scattering by immobilized photo catalyst • Restricted processing capacities due to possible mass transfer limitations • Possible catalyst deactivation and catalyst wash out

2.6.2. Photoreactors for air treatment

The most important process technologies for the air treatment are summarized in Figure 9. They cover processes for the removal of gases or volatile compounds or the removal of particles. The removal of particulate matter in flow gases emitted from point sources can be performed by applying cyclones, fabric filters, electrostatic precipitators and scrubbers. The applicability of these different techniques depends on the particle size. The removal of gases and volatile compounds from waste streams is based on a variety of different technologies such as thermal treatment, adsorption (on activated carbon or zeolite), membrane and biological processes, condensation, use of catalysts or adsorption in water (Oppenlander, 2003).

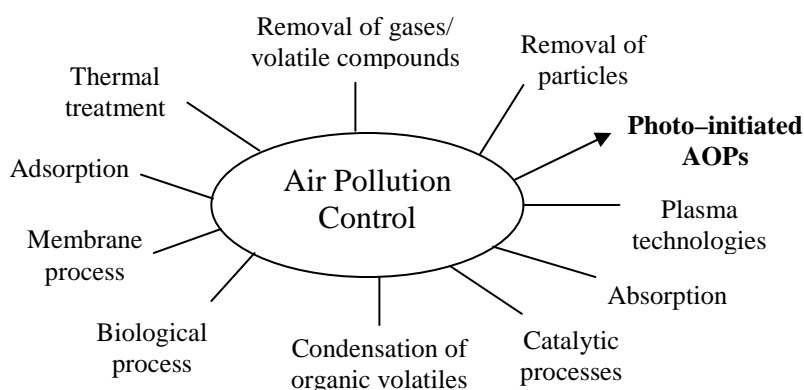


Fig 9: Process technologies for air pollution control (Oppenlander, 2003)

Non-thermal plasma processing and photo-initiated AOPs are promising and innovative in this field. The latter have great potential in air pollution control with respect to odor abatement, infection of air by control of air-borne bacteria, yeasts and mould spores, determination and mineralization of organic contaminants (Oppenlander, 2003).

Generally, all technologies that have been developed and applied commercially for VOCs are classified into two different groups: destructive and nondestructive. In the destructive methods, such as incineration, thermal and catalytic oxidation, VOCs are transformed into inert or less harmful compounds. In the second group, VOCs are retained and removed from the air without suffering any chemical modification. This group includes treatments as adsorption, condensation, and absorption (Zhao et al., 1998).

The treatment of air-borne organic pollutants by photo-initiated AOPs offers several advantages over aqueous systems and over conventional air purification technologies (Oppenlander, 2003; Carp et al., 2004; De Lasa et al., 2005):

- (i) simple process technology and photoreactor design;
- (ii) operating at ambient temperature and pressure;
- (iii) small scale indoor and industrial scale systems are realizable;
- (iv) the amount of photons adsorbed by air is negligible;
- (v) from low flow rate of the polluted gas up to $10^6 \text{ m}^3 \text{ h}^{-1}$ and more is possible;
- (vi) contaminant levels are often in the range of 0.1 to 1000 ppm;

- (vii) efficient mass transfer of substrate in the gas phase;
- (viii) relatively low levels of UV radiation are needed;
- (ix) OH^\bullet scavengers present in solution do not interfere and electron scavengers such as O_2 are rarely limiting.

Thus, when photoreactors are used to treat air pollution, they should be capable of treating fairly high gas feed rates. Hence, the high volume and low–pressure–drop reactor configuration is required. In order to achieve high conversion rate, the reactors require careful design and the selection of a number of reactor parameters such as (De Lasa et al., 2005):

- (i) light source;
- (ii) reactor configuration;
- (iii) lamp location;
- (iv) catalyst configuration;
- (v) interaction between the light, catalyst and reacting fluid.

Some of research papers on photo–initiated AOPs using TiO_2 in a gas phase are collected in Table 2. It is obvious from the Table 2 that the main activities in gas phase photochemical AOPs research are related to the investigation of the behavior of the volatile organic compounds.

As summarized in the Table 2, among several laboratory photoreactors designed for the determination of VOCs in gas phase, the fluidized–bed and annular photoreactors are the two representative types.

Table 2: Examples of research related to photo-initiated AOPs in a gaseous phase

Substrate	Photoreactor type	Reference
toluene	annular flow	Tomasic et al., 2008 Barraud et al., 2005 Blount and Falconer, 2002
toluene	fixed bed flow	Augugliaro et al., 1999 Kwang et al., 2008
toluene	fixed bed, carberry type	Marci et al., 2003
toluene	fluidized bed	Prieto et al., 2007 Kuo et al., 2009 Sekiguchi et al., 2008
VOCs ¹	annular flow	Bouzaza et al., 2006
VOCs ²	batch	Kim and Hong, 2002
VOCs ³	mixed flow	Strini et al., 2005
nitrogen oxide	annular flow & fluidized bed	Lim et al., 2000
trichloroethylene	annular flow & fluidized bed	Lim and Kim, 2004
acetone	annular flow	Ku et al., 2005
ethanol	annular flow	Paschoalino et al., 2006
oxalic acid	fluidized bed	Pozzo et al., 2006
<i>o</i> -xylene	fluidized bed	Gimeno et al., 2008
styrene	fluidized bed	Lim et al., 2008
carbonyl compound	fluidized bed	Zhang et al., 2006

¹trichloroethylene, toluene, isopropanol and butane; ²trichloroethylene, acetone, methanol, toluene; ³benzene, toluene, ethylbenzene and xylene (BTEX)

2.6.2.1. Fluidized-bed photoreactor

A fluidized-bed reactor (FBR) is a type of reactor where a fluid (gas or liquid) is passed through granular solid materials (catalyst material) at high enough velocities to suspend the solid and causes it to behave as it was a fluid. The catalysts in the fluidized-bed reactor are typically supported by a porous plate, known as a distributor. The fluid is forced to pass through the distributor up through the catalyst. At lower fluid velocities, the catalysts remain in place as the fluid passes through the voids in the catalyst. As the fluid velocity is increased, the reactor will reach a stage where the force of the fluid on the solids is enough to balance the weight of the solid material (Figure 10). This stage is known as incipient fluidization and occurs at this minimum fluidization velocity. Once this minimum velocity is surpassed, the contents of the reactor bed begin to expand and swirl around much like an agitated tank or boiling pot of water (Howard, 1989).

When trying to describe the operation of a fluidized-bed reactor, one main definition is the minimum fluidization velocity (U_{mf}). The superficial gas velocity at which the packed bed becomes a fluidized bed is known as the minimum fluidization velocity. This is also sometimes referred to as the velocity at incipient fluidization ("incipient" means "about to begin") (Howard, 1989).

Another common characteristic of fluidized beds is the *bed expansion*. When incipient fluidization is achieved, the fluid flowing upwards pushes the particles up and the separation distance between particles increases. This increases the void volume within the bed of particles and the bed is considered expanded. A schematic of an expanded bed is shown in Figure 10 (Howard, 1989).

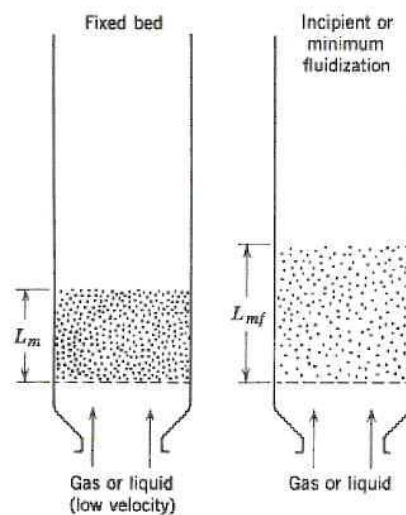


Fig 10: Bed expansion at minimum fluidization (Howard, 1989)

When a fluid is passed upwards through a bed of particles the pressure loss in the fluid due to frictional resistance increases with increasing fluid flow. A point is reached when the upward drag force exerted by the fluid on the particles is equal to the apparent weight of particles in the bed. At this point the particles are lifted by the fluid, the separation of the particles increases, and the bed becomes fluidized. The force balance across the fluidized bed dictates that the fluid pressure loss across the bed of particles is equal to the apparent weight of the particles per unit area of the bed. Thus:

$$\text{pressure drop} = \frac{\text{weight of particles} - \text{upthrow on particles}}{\text{bed cross sectional area}}$$

For a bed of particles of density ρ_p , fluidized by a fluid of density ρ_f to form a bed of depth H and voidage ε in a vessel of cross sectional area A, the pressure drop is given by:

$$\Delta P = \frac{HA(1-\varepsilon)(\rho_p - \rho_f)g}{A} \quad (24)$$

or

$$\Delta P = H(1-\varepsilon)(\rho_p - \rho_f)g \quad (25)$$

A plot of fluid pressure loss across the bed versus superficial fluid velocity through the bed would have the appearance depicted in Figure 11.

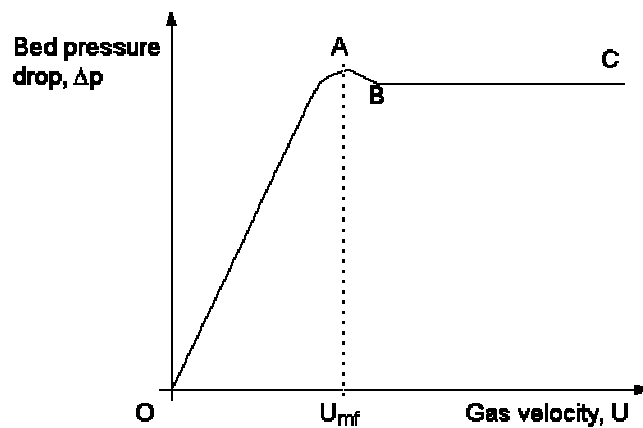


Fig 11: Pressure drop versus fluid velocity for packed and fluidized beds (Howard, 1989)

The straight line region OA is the packed bed region. Here the solid particles do not move relative to one another and their separation is constant. The pressure loss versus fluid velocity relationship in this region is described in general by the Ergun equation (Howard, 1989):

$$\frac{(-\Delta P)}{H} = 150 \frac{(1-\varepsilon)^2 \mu U}{\varepsilon^3 d_p^2} + 1.75 \frac{1-\varepsilon}{\varepsilon^2} \frac{\rho_f U^2}{d_p} \quad (26)$$

The region BC in Figure 11 is the fluidized-bed region where Eq. 24 applies. At point A it is noticed that the pressure loss rises above the value predicted by Eq. 24. This rise is more marked in powders which have been compacted to some extent before the test and is associated with the extra force required to overcome interparticle attractive forces.

U_{mf} increases with particle size and particle density and is affected by fluid properties. It is possible to derive an expression for U_{mf} by equating the expression for pressure loss in a fluidized bed (Eq. 25) with the expression for pressure loss across a packed bed. Thus substituting the expression for $(-\Delta P)$ for a fluidized bed from Eq. 25 into the expression for $(-\Delta P)$ for a packed bed from Eq. 26 leads to:

$$(1-\varepsilon)(\rho_p - \rho_f)g = 150 \frac{(1-\varepsilon)^2}{\varepsilon^3} \frac{\mu U_{mf}}{d_p^2} + 1.75 \frac{(1-\varepsilon)}{\varepsilon^3} \frac{\rho_f U_{mf}^2}{d_p} \quad (27)$$

Rearranging,

$$Ar = 150 \frac{(1-\varepsilon)}{\varepsilon^3} Re_{nu} + 1.75 \frac{1}{\varepsilon^3} Re_{nu}^2 \quad (28)$$

where Ar is the dimensionless number known as the Archimedes number and Re_{mf} is the Reynolds number at incipient fluidization,

$$Ar = \frac{\rho_f (\rho_p - \rho_f) g d_p^3}{\mu^2} \quad (29)$$

$$Re_{mf} = \left(\frac{U_{mf} d_p \rho_f}{\mu} \right) \quad (30)$$

In order to obtain a value of U_{mf} from Eq. 28 we need to know the voidage of the bed at incipient fluidization, $\varepsilon = \varepsilon_{mf}$. Taking ε_{mf} as the voidage of the packed bed, we

can obtain crude U_{mf} . However, in practice voidage at the onset of fluidization may be considerably greater than the packed bed voidage. A typical often used value of ε_{mf} is 0.4. Using this value, Eq. 28 becomes:

$$Ar = 1406 Re_{mf} + 27.3 Re_{mf}^2 \quad (31)$$

When a photocatalytic reaction takes place in a gas–solid reactor, it is necessary to achieve both, exposure of the catalysts to light irradiation and a good contact between reactants and catalyst. Fluidized–bed reactors not only bring more contact between catalysts and gas but also enhance UV radiation penetration compared with annular flow reactors in which photons cannot penetrate easily into the interior of the catalyst film. It is accepted that the fluidized–bed reactors have advantage for enhancing of UV radiation penetration efficiency into the interior of photocatalyst bed, easy temperature control and good contacting between target components and photocatalyst. Taking all described features into account, the reactor should be designed to provide higher reactant throughput and lower pressure drops in the bed (Lim et al., 2000; Na et al., 2004).

2.6.2.2. Annular photoreactor

The annular reactors are generally composed of two concentric cylinders that form an annular region with a certain gap. The catalyst is coated on the interior wall of the outer cylinder when the light source locates at the center, and the thickness of the catalyst film coated on the surface of reactor is thin enough to let all the catalyst be illuminated by UV radiation. When light source locates outside the reactor, the catalyst is coated on the surface of two centric cylinders. In general, the cross section of annular reactor is small so that high gas flow velocity can be obtained to ensure that products desorbed from surface could be removed quickly (Larson et al., 1995). Figure 12 shows a typical annular flow reactor which was used for photocatalytic oxidation of toluene in gas phase over UV–illuminated thin film layer of TiO_2 at room temperature (Tomasic et al., 2008). Different operating variables like water content, inlet toluene concentration and gas flow rate were investigated. The catalytic activity for toluene removal was evaluated by measuring the inlet and outlet toluene concentrations with GC/FID at the steady–state conditions. Modelling analysis was carried out to investigate effect of the key parameters on the reactor performance

(one-dimensional (1D) model and two-dimensional (2D) models based on ideal flow and laminar flow conditions). The proposed models were verified by comparing the computer simulation data with the experimental laboratory results. It was found out that the behaviour of the annular photocatalytic reactor was mainly limited by the interphase mass transfer (Tomasic et al., 2008). Finally, the 2D heterogeneous model, based on the assumed laminar flow through the reactor, appeared to be the most suitable model for a detailed description of the annular photocatalytic reactor used for air pollution remediation (Tomasic et al., 2008).

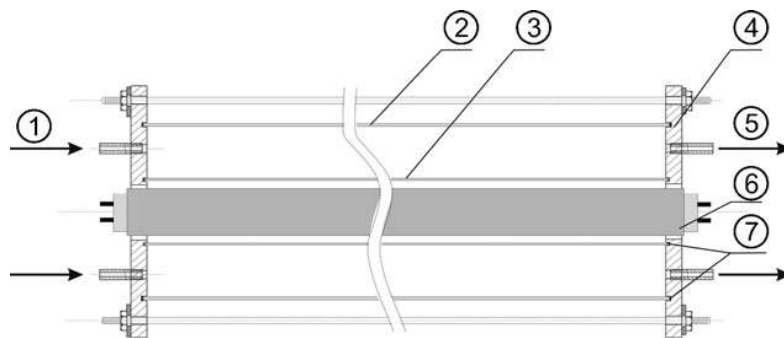


Fig 12: Scheme of the photocatalytic annular reactor: (1) gas inlet, (2) outer tube with the catalyst layer, (3) inner tube, (4) end plate, (5) gas outlet, (6) UV tube, (7) rubber O ring (Tomasic et al., 2008)

III. Research goals

The main goals of research could be divided into four parts:

- Preparation of nanocrystalline titania (unsupported TiO_2) in the form of aqueous sol and powder via sol–gel method at low–temperature preparation condition; studying the effect of the type of the acid, HNO_3 and HClO_4 , and the effect of the amount of the acid on the structure and properties of titania aqueous sol and powder; characterization of as-prepared titania powder by X–ray diffraction, thermal analysis, UV–vis spectroscopy and nitrogen sorption measurements; measuring the aggregate size of titania powder in the colloidal solution by dynamic light scattering; studying the correlation between characteristics and photocatalytic activities of the as–prepared powders towards degradation of aqueous phenol solution under UVA radiation.
- For increasing the photocatalytic activity of titania and to prevent the aggregation of the nanocrystalline titania, loading the as–prepared aqueous titania sol into/onto silica mesoporous materials (as a high–surface–area support) via sol–gel impregnation method; synthesis of the two types of silica mesoporous powders: SBA–15 as an ordered and KIL–2 as a disordered mesoporous silica.
- Investigation of the physico–chemical properties of titania/silica photocatalysts powders (supported TiO_2) by X–ray diffraction, nitrogen–sorption measurements, UV–vis diffuse reflectance (DRS), infrared absorption spectroscopy (FT–IR) and high resolution transmittance electron microscopy (HR–TEM); studying the influence of a Ti/Si nominal molar ratio and the type of the silica support towards photocatalytic degradation of gaseous toluene.
- Studying the photocatalytic degradation of toluene in the self–constructed fluidized–bed photoreactor system which was built for this purpose; studying the photocatalytic activities of the titania/silica powders for degradation of

gaseous isopropanol as well in another type of solid–gas photoreactor system to correlate the functional properties of prepared powders in gaseous photocatalysis.

IV. Experimental

4.1. Chemicals

All the chemicals in this study were used as purchased: titanium tetrachloride, perchloric acid, triethanolamine, potassium oxalate and phenol from Fluka, ammonia solution from Poch, silver nitrate and sodium hydroxide from Carlo Erba, nitric acid and toluene from J. T. Baker, hydrochloric acid from Merck, tetraethyl ortosilicate and tetraethylammonium hydroxide from Acros, Pluronic[®] P123 triblock copolymer and tetraethyl orthosilicate from Aldrich, ethanol and iron (III) sulfate from Riedel–de Haen, air 5.5 from Istrabenz. For all experiments, all the aqueous solutions were prepared by using highly pure water ($< 18 \text{ M}\Omega \text{ cm}^{-1}$) from the NaNOpure (Barnstead). For the HPLC analyses: ammonium acetate solution from Merck and acetonitrile from J. T. Baker, all analytical grade, were used. For the GC–MS analyses: helium 5 and nitrogen 5 were purchased from Fegelj.

4.2. Synthesis of materials

4.2.1. Synthesis of unsupported titania materials

4.2.1.1. Synthesis of aqueous titania sol

The TiO_2 sols were synthesized using a titanium tetrachloride (TiCl_4) as a precursor via sol–gel method at low–temperature preparation conditions. The synthesis procedure and characterization of products is also described in our publication (Tasbihi et al., 2009). Titanium tetrachloride was used as a main starting material without any further purification. A 10 % ammonia solution ($\text{NH}_{3(\text{aq})}$) was slowly added to certain amount of TiCl_4 until the pH value reached 7. The reaction was highly exothermic and produced high quantities of fumes. The resulting white precipitate was then washed with double deionized water until all chlorides were completely removed (negative silver nitrate (AgNO_3) test). The deionized water was added to this precipitate at room temperature to obtain 2.5 wt. % of TiO_2 . The suspension was divided into two parts. Each part was mixed with an acid at a suitable $[\text{Ti}]/[\text{H}^+]$ ratio for redispersion of amorphous titanium hydroxide in aqueous solution. The optimized molar ratio of $[\text{Ti}]/[\text{H}^+]$ to obtain the most active photocatalyst was suggested to be around 1 (Liu et al., 2008a). Generally, while preparing crystalline

TiO₂ at low temperatures, strong acids are used as peptizing agents and as the condensation promoters. In this study, nitric acid (HNO₃) and perchloric acid (HClO₄) were used for peptization of the two parts of the suspension and [Ti]/[H⁺] ratios were fixed at 0.5 and 2.5 in order to elucidate the influence of this ratio on the sol properties. The resulting solution was refluxed at 70 °C for 24 h under vigorous stirring following the treatment proposed by Liu et al. (2008a). To verify the effect of reflux condition, some experiments were conducted at 100 °C, but the obtained sols were of much lower quality (unstable colloids were obtained).

4.2.1.2. Synthesis of unsupported titania powders

The powder was obtained from the colloidal sols by evaporation of solvent (water) at 50 °C for 12 h and drying in air at 150 °C for 3 h. These powders were designated as Ti–N (0.5 or 2.5) and Ti–Cl (0.5 or 2.5), where N and Cl indicate HNO₃ and HClO₄ peptizing agents respectively, and numbers refer to the [Ti]/[H⁺] ratio. White powders were obtained irrespective of the type or amount of acid used. These as-prepared white powders contained some inorganic residual (see XRD results, section 5.1.1.). For determining a TiO₂ quantity in the as-prepared powders, which were used in photocatalytic experiments, a certain amount of powder was calcined in air at 400 and 600 °C. The mass differences of powders before and after calcination were considered for the determination of the weight of the TiO₂ catalyst in the photoreactor experiments (Table 3).

Table 3: The TiO₂ content in different unsupported titania powders

Sample	Dried sample (g)	Calcined sample (400 °C, 1h) (g)	wt. % of TiO ₂
Ti–Cl(0.5)	0.3042	0.2042	67.6
Ti–Cl(2.5)	0.3747	0.2551	68.1
Ti–N(0.5)	0.3028	0.2352	77.9
Ti–N(2.5)	0.2201	0.1603	72.8

4.2.2. Synthesis of supported titania powders

4.2.2.1. Synthesis of KIL-2 as a silica support

The two-step synthesis of the disordered mesoporous KIL-2 powders was developed on the basis of the neutral templating method in which small, non-surfactant templates such as triethanolamine (TEA) direct the polycondensation of inorganic species (Novak Tušar et al., 2010). In the first step tetraethyl orthosilicate (TEOS) and triethanolamine were stirred for 30 min. Then deionized water was added to the mixture, followed by the addition of tetraethylammonium hydroxide (TEAOH). The solution was stirred with the aid of a magnetic stirrer to obtain homogeneous gel. The final gel, having pH of 7, with molar composition of 1 TEOS: 0.5 TEA: 0.1 TEAOH: 11 H₂O was aged overnight at room temperature and then dried in an oven for 24 h at 50 °C. In the second step the gel was solvothermally treated in ethanol in Teflon-lined stainless steel autoclaves at 150 °C for 48 h. Removal of the template was performed by calcination at 500 °C for 10 h using a heating rate of 1 °C min⁻¹ in air. In this way the thermal stability of the product was also established. The hydrothermal stability of the products was verified by keeping them in the boiling water for 2 h (Novak Tušar et al., 2010).

4.2.2.2. Synthesis of SBA-15 as a silica support

Ordered mesoporous silica SBA-15 powders were synthesized according to the well-known procedure (Zhao et al., 1998; Mazaj et al., 2009). 8 g of Pluronic[®] P123 triblock copolymer was added to 260 mL of distilled water and 40 mL of concentrated hydrochloric acid (37 wt. %, HCl). The mixture was stirred until the surfactant was dissolved. Then 17 mL of TEOS was added under stirring at 45 °C. The reaction gel was stirred for 8 h at 45 °C and aged for another 16 h at 80 °C. The obtained gel with molar ratios of reaction components 1 SiO₂: 0.017 P123: 5.85 HCl: 190 H₂O was hydrothermally treated in a stainless steel Teflon-lined autoclave at 100 °C for 24 h. The obtained product was continuously washed with distilled water and dried at room temperature. The surfactant was removed by calcination at 550 °C for 6 h in an air flow at a heating rate of 1 °C min⁻¹ (Mazaj et al., 2009).

4.2.2.3. Synthesis of titania/silica powders: MTi/KIL-2 and MTi/SBA-15 using Ti-isopropoxide

The MTi/KIL-2(x) and MTi/SBA-15(x) powders were prepared by using Ti-isopropoxide ($\text{Ti}(\text{O}^i\text{Pr})_4$) as a precursor and SBA-15 or KIL-2 synthesized support using acid-catalyzed sol-gel method which was described by Busuioc et al. (2006). Ti-isopropoxide was added gradually to aqueous solution of 1 M nitric acid (HNO_3) under continuous stirring for 2 h. Subsequently, the colloidal solution was diluted with deionized water and the pH was adjusted to 3 with 1 M sodium hydroxide (NaOH) solution. The pH adjustment was made to prevent destruction of the support by reaction with the acid. Then an appropriate amount of SBA-15 or KIL-2 was added to the colloidal dispersion. The mixture was stirred for 2 h at room temperature, followed by centrifugation and washing with deionized water, until the pH was about 6. The capillary force was believed to drive titania dispersion into the highly ordered mesoporous silica support. The solid product was dried at 60 °C and then calcined at 300 °C for 6 h. These samples were denoted as MTi/KIL-2(x) or MTi/SBA-15(x) where x is the molar ratio of Ti/Si that was adjusted to 1/1. These powders were prepared at the National Institute of Chemistry in Ljubljana and were used as a reference.

4.2.2.4. Synthesis of titania/silica powders: STi/KIL-2 and STi/SBA-15 using aqueous titania sol

The STi/KIL-2(x) and STi/SBA-15(x) powders were prepared using freshly made aqueous crystalline anatase- TiO_2 sol which was described in section 4.2.1.1. with $[\text{Ti}]/[\text{H}^+]$ ratio 2.5 (Tasbihi et al., 2009). The sol was deposited to the appropriate amount of SBA-15 or KIL-2 by the impregnation method (Tasbihi et al., 2010a). Before impregnation of sol to the support, the pH of the sol was adjusted to 3 with 1 M NaOH solution, resulting in a milky colloidal suspension. Here the pH adjustment was also made to prevent destruction of the support by reaction with the acid. Then a nominal amount of support was added to the colloidal dispersion. The mixture was stirred for 2 h at room temperature, followed by centrifugation and washing with deionized water, until the pH was about 6. The white precipitate was dried at 60 °C for 24 h. Calcination at higher temperature was not needed because the titania source was already crystalline. The samples prepared from KIL-2 and SBA-15 were

designated as STi/KIL-2(x) and STi/SBA-15(x), respectively, where x is the nominal molar ratio of Ti/Si that was adjusted to 1/2, 1/1 and 2/1.

The commercial photocatalyst, a Millennium PC500 (100 % anatase, BET surface area: 300 m² g⁻¹, crystal size: 5–10 nm), was used as a reference photocatalyst.

4.3. Characterization of materials

4.3.1. X-ray diffraction (XRD)

The X-ray powder diffraction (XRD) patterns were obtained on a PANalytical X'Pert PRO high-resolution diffractometer with an alpha 1 configuration using CuK_{α1} radiation (1.5406 Å) in the range with a step size of 0.033 using a fully opened X'Celerator detector. Diffraction patterns were compared with reference JCPDS (Joint Committee on Powder Diffraction Standards) powder diffraction files (anatase: 21-1272, rutile: 21-1276, brookite: 29-1360). The average crystallite size was determined from the broadening of the (1 0 1) anatase peak reflection by Scherrer formula:

$$L = \frac{k\lambda}{\beta \cos \theta} \quad (32)$$

where L is the crystallite size, λ is the wavelength of the X-ray radiation (CuK_α = 1.5406 Å), shape factor k is related to the crystallite shape, usually taken as 0.9 (Ambrus et al., 2008), and β is the peak width at half-maximum height corrected for instrumental broadening.

The determination of crystallite size measured by Scherrer's equation gives an effective size of coherently scattering domains and serves to estimate the sizes rather than to give the exact values. Spherical crystallites and no crystal distortion in the lattice are assumed in calculation.

4.3.2. Dynamic light scattering (DLS)

The sizes of aggregated TiO₂ particles in colloidal suspension solutions (the same as used for photocatalytic degradation of phenol in aqueous solution experiments (section 4.4.1.2)) were measured by dynamic light scattering. For this purpose we have used the 3D-DLS-SLS spectrometer from LS Instruments (Fribourg, Switzerland) equipped with a 20 mV He-Ne laser (Uniphase JDL 1145 P) and operating at 632.8 nm. The instrument enables the determination of hydrodynamic radii of particles even in extremely turbid suspensions by the so-called 3d cross-correlation technique that successfully eliminates multiple scattering of light (Urban et al., 1998). Scattering was measured at an angle of 90°. Samples in the scattering cells were immersed in a large-diameter bath of index matching liquid that was thermostated at 25 °C. Ten measurements of 60 s each were recorded for each sample and averaged afterwards. In a DLS experiment, the translational diffusion coefficient D is determined via the relationship $D = (1/\tau)q^{-2}$, where τ is the relaxation time and q is the scattering vector. The average size of particles can be estimated from D as the hydrodynamic radius R_h of the assumed hard sphere by applying the Stokes-Einstein equation:

$$R_h = \frac{k_B T}{6\pi\eta D} \quad (33)$$

In Eq. 33, k_B is the Boltzmann constant, T is the absolute temperature and η is the viscosity of the solvent. The viscosity of the solvents used in this study was measured in a capillary viscosimeter at 25 °C. Their values ($\eta = 0.8908$ cP) were very close to water viscosity ($T = 25$ °C: $\eta = 0.8903$ cP) and therefore no corrections of results were needed if the viscosity of pure water was taken into account.

4.3.3. UV-vis spectroscopy

4.3.3.1. UV-vis transmittance

The transmittance spectra (300–700 nm spectral range) of colloidal suspensions of TiO₂ with the concentration of 1.0 g L⁻¹ (the same as used for photocatalytic degradation of phenol in aqueous solution experiments (section 4.4.1.2)) were recorded on a UV-vis-NIR spectrophotometer Lambda 950 (Perkin-Elmer).

4.3.3.2. UV–vis diffuse reflectance (UV–vis DRS)

Band–gap energy of the all synthesized powders was determined spectroscopically (Tasbihi et al., 2010b). Diffuse reflectance spectra of the powder photocatalysts placed in 1 mm quartz cell were measured using UV–vis–NIR spectrophotometer Lambda 19 (Perkin–Elmer) equipped with an integrating sphere. The original coordinates of the spectra (reflectance vs. wavelength) were transformed to Kubelka–Munk function (K) vs. photon energy ($h\nu$) (Burgeth et al., 2002; Kuči et al., 2009). The final plots of $(Kh\nu)^{1/2}$ as a function of $h\nu$ are in accordance with the theoretical equation (Serpone and Pelizzetti, 1989)

$$h\nu\alpha = \text{const}(h\nu - E_{bg})^2 \quad (34)$$

where α is absorption coefficient of the photocatalyst and E_{bg} its band–gap energy. (The Kubelka–Munk function (K) calculated from the reflectance spectra is predetermined to be directly proportional to the absorption coefficient (α)). The values of energy band gap are usually estimated by extrapolation of the linear part of the dependence. However, we employed a more precise method based on fitting of the experimental dependences by Boltzmann symmetrical function using non–linear regression (Kuči et al., 2009). Then the calculated crossing point of the tangent line in the inflection point of the Boltzmann fit with its lower asymptote determines the energy band gap as shown in Figure 13 (Kuči et al., 2009).

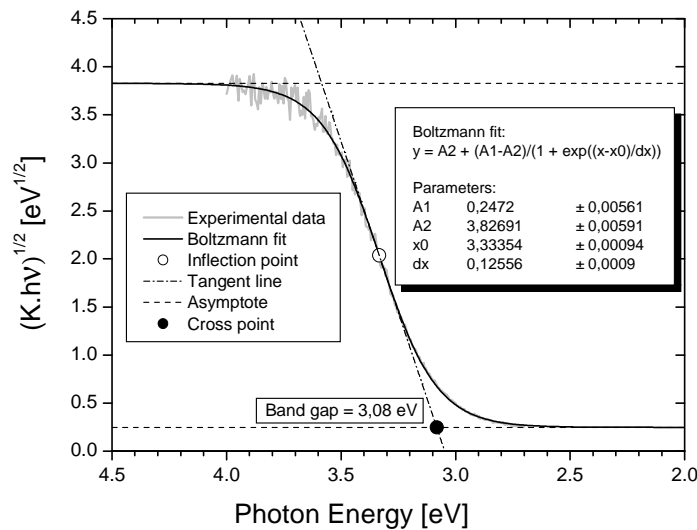


Fig 13: Determination of energy band gap from a transformed diffuse reflectance spectrum (Kuči et al., 2009)

For powders composed of more components (e.g. two different crystallographic phases), the single Boltzmann function did not fit the experimental data well. In such cases, a double Boltzmann fit by a sum of two Boltzmann functions was applied.

4.3.4. Nitrogen-sorption measurement

Porosity and specific surface area were evaluated by analysis of nitrogen adsorption isotherms measured on a Micromeritics Tristar 3000 instrument (Tasbihi et al., 2010a). These isotherms were recorded at 77 K. The samples were outgassed at 473 K for 2 h in the port of the adsorption analyzer. The BET (Brunauer–Emmett–Teller) specific surface area (Brunauer et al., 1938) was calculated from adsorption data in the relative pressure range from 0.05 to 0.2. The total pore volume (V_t) was estimated on the basis of the amount adsorbed at a relative pressure of 0.96 (Sing et al., 1985). The primary mesopore volume (V_{me}) and the external surface area (S_{ex}) were determined using the α_s -plot method (Sing et al., 1985; Sayari et al., 1997) from the adsorption data in the range of the standard reduced adsorption from 1.7 to 2.5 for SBA-15 materials and from 2.1 to 3.0 for KIL-2 materials. In the α_s -plot calculations, a macroporous silica material LiChrospher Si-1000 ($S_{BET} = 22.1 \text{ m}^2 \text{ g}^{-1}$) was used as a reference adsorbent (Tan et al., 2005). The pore size distributions (PSDs) were calculated from nitrogen adsorption data using an algorithm based on ideas of Barrett, Joyner, and Halenda (BJH) (Barrett et al., 1951). The maximum on the PSD is considered as the primary mesopore diameter for given powders.

4.3.5. Electron microscopy

4.3.5.1. Scanning electron microscopy (SEM)

Structural morphology of the prepared powders was revealed by scanning electron microscopy (SEM). A Philips XL 30 CP microscope equipped with EDX (energy dispersive X-ray), Robinson, SE (secondary electron) and BSE (back-scattered electron) detectors was used.

4.3.5.2. High resolution transmittance electron microscopy (HR-TEM)

High resolution transmission electron micrographs of STi/SBA-15(2/1) and STi/KIL-2(2/1) powders were carried out on a JEOL JEM 3010 microscope operated at 300 kV (LaB6 cathode, 1.7 Å point resolution) with an energy dispersive X-ray

(EDX) detector attached. The powders were dispersed in water and a drop of diluted suspension was placed on a carbon-coated grid and evaporated at ambient temperature. Electron diffraction (ED) patterns were evaluated using the Process Diffraction software package.

High resolution transmission electron micrographs of SBA-15, STi/SBA-15(1/2), STi/SBA-15(1/1), STi/KIL-2(1/2) and STi/KIL-2(1/1) powders were obtained on a JEOL JEM 2100 microscope operated at 200 keV with an energy dispersive X-ray (EDX) detector attached. EDX spectroscopy measurements were performed on a JEOL JED-2300T EDS system having high energy resolution and high sensitivity.

4.3.6. Elemental analysis

The concentration of elements were measured with inductively-coupled plasma atomic emission spectrometry (ICP-AES) on Thermo Jarrell Ash, model Atomscan 25. This method measures intensity of emitted light from excited atoms of elements in the gas phase. Atomization of the sample is needed for obtaining free atoms, which is achieved through very high temperature (6000 to 10,000 °C). Since atoms in the gas phase are separated from each other, the emitted energy (wavelengths) is characteristic for each element. Strength (intensity) of each line is proportional to the concentration of particles, which forms the basis for quantitative analysis.

4.3.7. Fourier transform infrared spectroscopy (FT-IR)

The IR spectra of the powder samples dispersed in KBr pellets were recorded using a FT-IR Perkin-Elmer Spectrum 100 spectrometer with a 4 cm⁻¹ resolution in the frequency range from 4000 to 400 cm⁻¹.

4.3.8. Thermal analysis (TGA-DSC)

Thermal gravimetric analysis (TGA) and differential scanning calorimetry (DSC) were performed using a Mettler Toledo TG/SDTA 851° instrument with heating range from room temperature up to 900 °C. The samples were heated in air flow with a heating rate of 5 K min⁻¹. DSC measurements were performed on a Mettler Toledo DSC 822° instrument. The baseline was subtracted in all cases.

4.4. Photocatalytic activity tests

4.4.1. Determination of photocatalytic activities in liquid–solid system

4.4.1.1. Photoreactor set–up

The photocatalytic experiments in aqueous system were performed in a photoreactor (Figure 14) that was previously constructed in our laboratory (Černigoj et al., 2007). Three low–pressure mercury fluorescent lamps were used as a UVA radiation source (CLEO 20W, 438 mm × 26 mm, Philips; broad maximum at 355 nm). The lamps are positioned on a circular line at the periphery of the photoreactor and the reflective surface of polished aluminum is placed behind them. In order to conduct experiments at a controlled temperature and to protect the lamp from overheating, there is a fan at the bottom part of the reactor. The photocatalytic cell was positioned in the center of the reactor and it consists of a quartz glass tube (400 mm, inner diameter of 18.5 mm and outer diameter of 22.7 mm) which was closed with the valve for purging with air at the bottom. The photon flux in the cell was evaluated by potassium ferrioxalate actinometry (Murov et al., 1993) (potassium oxalate, $K_2C_2O_4$, iron(III) sulfate, $Fe_2(SO_4)_3$), and determined to be 4.28×10^{-5} einstein $L^{-1} s^{-1}$.

4.4.1.2. Photocatalytic degradation of phenol

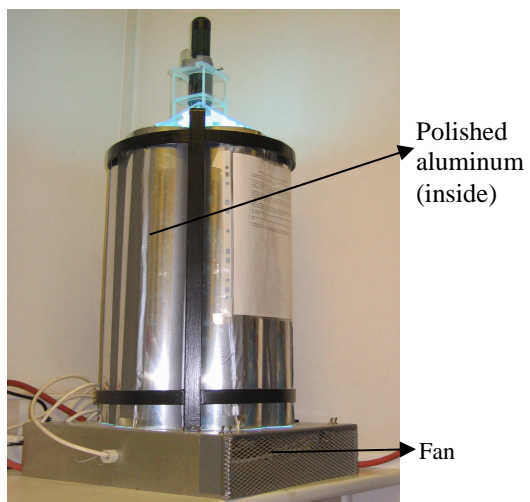
Aqueous solution (50 mL) of phenol (C_6H_5OH) (50 mg L^{-1}) was used as a photodegradation medium in all experiments. The concentration of the dried pure TiO_2 powders was 1.0 g L^{-1} (refer to Table 3). Before adding a catalyst to the phenol solution, $HClO_4$ was added to adjust the pH value of the solution. The pH was adjusted to $pH = 2.6$ due to the two reasons: (1) the powders at neutral or near neutral pH precipitated in the aqueous solution; (2) the pH of the phenol solution during photocatalysis does not change much if the initial pH is low enough (consequently also the kinetics of the degradation does not change much during the course of photodegradation). The mixtures of phenol solution and catalyst powder were sonicated for 15 min using a sonicator (Sonic 4, Iskra Pio d.o.o.). The prepared suspension was then kept in dark for about 30 min to achieve the adsorption/desorption equilibrium. After dark adsorption procedure the suspension was irradiated. During the irradiation, the solution was constantly purged with air (10 L h^{-1}), keeping the solution saturated with dissolved air during the whole irradiation

time. The temperature was kept constant at 35 °C during the experiment. Samples were taken out at regular time intervals, and they were immediately stored in a 2.5 mL screw cap amber glass. Before HPLC analysis, the samples were neutralized with ammonium acetate solution, centrifuged (Eppendorf, 5415 R) at 13,200 rpm for 10 min and then the supernatant was collected for analysis.

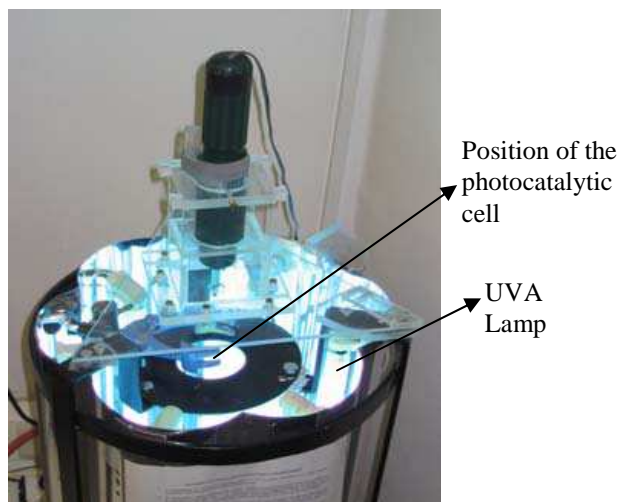
4.4.1.3. High performance liquid chromatography (HPLC) analysis

A high performance liquid chromatography (HPLC) was used to evaluate the concentration of phenol in the solution. The HPLC equipment consists of an HP 1100 Series chromatograph, coupled with a DAD detector. The chromatographic separations were run on a Kromasil 100, C8 column (BIA separations d.o.o., 250 mm × 4.6 mm, 5 μm) using a 85:15 mixture of 10 mM aqueous ammonium acetate ($\text{NH}_4\text{OOCCH}_3$) solution and acetonitrile (CH_3CN) as the eluent in the first 4 min, then it was changed into a 30:70 mixture by applying a linear gradient between 4 and 16 min. The eluent flow rate was 1.0 mL min⁻¹ and injection volume 10 μL. The elutions of compounds were monitored by the DAD detector at 272 nm.

A)



B)



C)

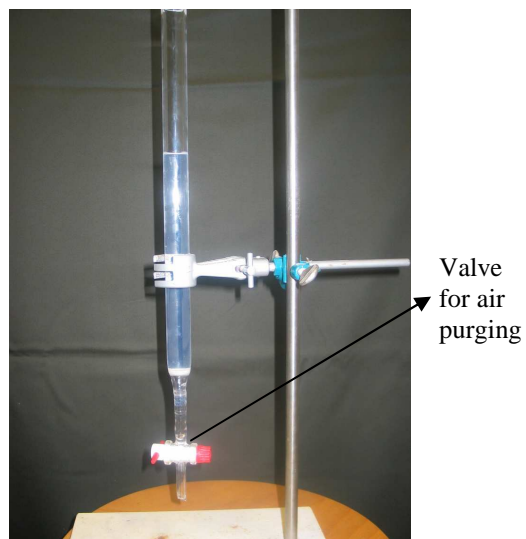
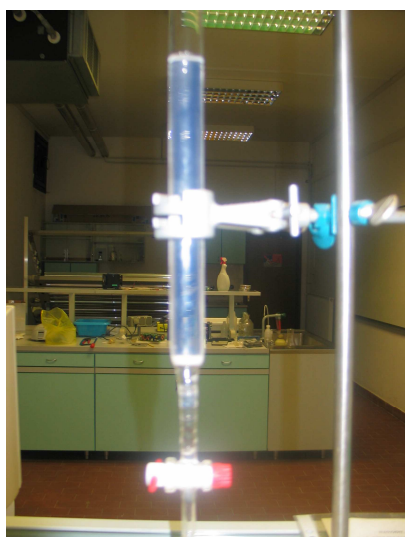


Fig 14: Photoreactor set-up for aqueous system: (A) the side view; (B) the upper view; (C) a photocatalytic cell with an aqueous phenol solution and dispersed catalyst used for the photocatalytic experiment

4.4.2. Determination of photocatalytic activities in gas–solid system with in–situ FT–IR

4.4.2.1. Photoreactor set–up

Photocatalytic activity of the powders in a gas medium was first evaluated by monitoring the degradation of a model organic compound with FT–IR spectroscopy (Tasbihi et al., 2010a). These measurements were carried out at the Slovenian National Building and Civil Engineering Institute, Ljubljana. A schematic diagram of the experimental set–up is shown in Figure 15. A cylindrical reactor (1.4 L in volume) covered by quartz glass was constructed and connected by Teflon tubes to the FT–IR spectrometer. The whole system was hermetically sealed. The light source was a 300 W Xe lamp (Newport Oriel Instrument, USA). The infrared part of the spectrum was blocked by means of an adequate filter. The samples were prepared in the shape of a thin layer of powder with constant mass (50 mg) – and thus more or less constant thickness – in a Petri dish with 6 cm in diameter. The working distance between the Petri dish and the Xe lamp was 6 cm. Such an arrangement resulted in a light intensity of $\sim 30 \text{ W m}^{-2}$ in the UV range. Due to a strong influence of relative humidity on photocatalytic activity (Einaga et al. 2002; Maggos et al., 2007), the relative humidity at 23 °C in the system prior to the experiment was kept within the range of 25–30 %. It was regulated by means of a flow of air passing through the molecular sieves until a pre–defined humidity was attained. Temperature and relative humidity were measured by thermo– and hydro–meter, respectively, which were placed into the reactor.

4.4.2.2. Photocatalytic degradation of isopropanol

The model organic compound, isopropanol was oxidized to acetone upon irradiation and then into several further degradation products. Each experiment was performed by injecting 5 μL of liquid isopropanol (~ 1100 ppm in a gas phase) into the reacting system through a septum. The total reaction time was set at 20 h. The lamp was turned on after a certain period of time to allow for equilibration of the adsorption of isopropanol onto the powder. The isopropanol degradation and acetone formation/degradation processes were followed by monitoring the calculated area of their characteristic peaks at 951 and 1207 cm^{-1} , respectively, in the IR spectra measured by a FT–IR spectrometer (Perkin–Elmer Spectrum BX, USA). The

photocatalytic activity of the samples was evaluated as the rate constant of the initial acetone formation. At room temperature the photocatalytic oxidation of isopropanol to acetone is fast, whereas the subsequent oxidation of acetone to CO₂ and H₂O is slower (Larson et al., 1995). At very short times the slope is proportional to the formation rate constant (Senthilkumaar et al., 2005). In addition, being the first intermediate of isopropanol degradation (Ohko et al., 1998), the formation of acetone is a process that can easily be distinguished from the subsequent degradation process occurring during isopropanol photo-oxidation. A kinetic model was used to fit the experimental data in the range of acetone formation, enabling the calculation of acetone formation rate constants.

A photo of photoreactor set-up for in-situ FT-IR gaseous system is presented in Figure 16.

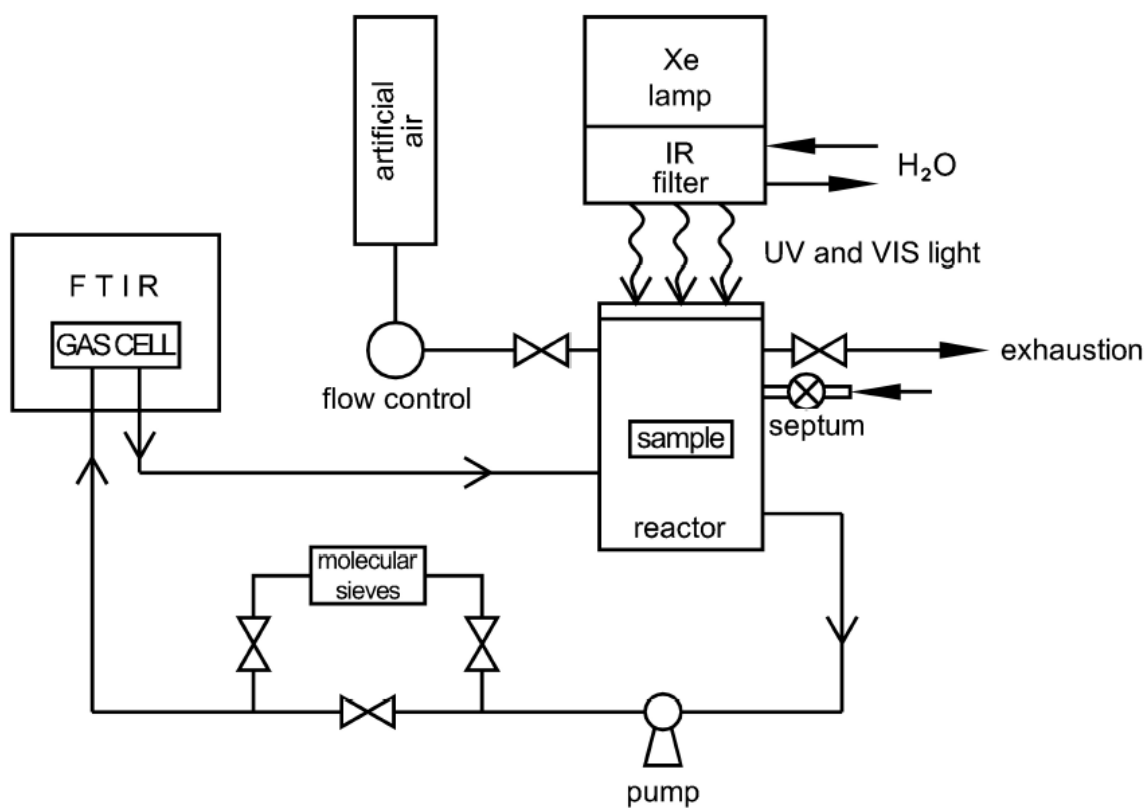


Fig 15: Schematic diagram of the experimental set-up for in-situ FT-IR gaseous system

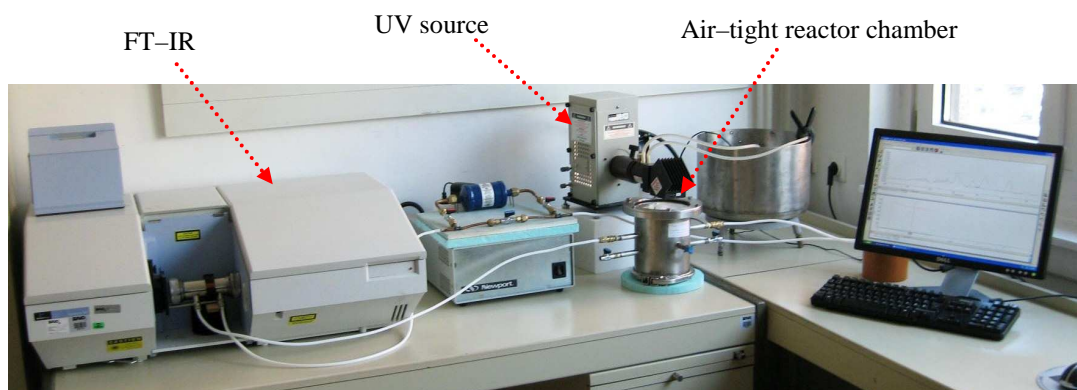


Fig 16: A photo of photoreactor set-up for in-situ FT-IR gaseous system (provided by Slovenian National Building and Civil Engineering Institute, Ljubljana)

4.4.3. Determination of photocatalytic activities in gas–solid system with in–situ GC–MS

4.4.3.1. Photoreactor set–up

The schematic diagram of the photoreactor system that was constructed for the in–situ GC–MS photocatalytic experiments is shown in Figure 17 (Tasbihi et al., 2010b). The first part provides the feed for the reaction which consists of an air cylinder, two mass flow meters/controllers (Aalborg AFC 26), a mixing chamber and a syringe pump (TSE System). The second part represents a reaction loop, which includes a flow meter (Aalborg), two compact diaphragm pumps (Sensortech GmbH), first for circulation of the mixed gas flow through the set–up and second for circulation of the mixed gas flow through the on–line GC–MS, a sampling port, a reactor cell, a 1 L reservoir vessel, a water bath (IKA, ET basic) and a chromatographic on–line GC–MS analyzer (Varian). Pure synthetic air (purity = 5.5) was used as a source of oxygen. The mixing chamber consists of a 30 cm long Duran glass tube with 3 cm outer diameter. The compact photoreactor (Rayonet reactor, model RPR–100) has dimensions of 35.5 cm × 35.5 cm × 20.5 cm. The reactor chamber consists of six low–pressure mercury fluorescent lamps which were used as a UVA radiation source (15 W, 265 mm × 16 mm, Philips CLEO; broad maximum at 355 nm) and the reflective surface of polished aluminum which is placed behind the lamps. An incident intensity of 36.5 W m⁻² was determined at the photoreactor cell surface using photometry Xenocal UV–sensor. The reaction cell was made from a Duran glass tube (10 mm inner diameter, 27 cm height) and was positioned vertically in the center of the photoreactor. A porous frit at the bottom of the reactor cell allowed distributing finely the inlet gaseous mixture through the catalyst powder. Another frit in the upper part of the reactor cell prevented the photocatalyst powders for escaping with the gas stream out of the photoreactor cell. All the connections, valves and tubes in this set–up were made of Teflon.

4.4.3.2. Photocatalytic degradation of toluene

In a typical test, the regulated air stream was divided into two paths. One served for the humidification of the air and the other one for transportation of dry air. The humidification was achieved by bubbling air through a glass bottle containing deionized water. Both air flows were regulated by mass flow meters/controllers. The

flow rates of both dry and humidified air were adjusted to 0.2 L min^{-1} to obtain the total air flow 0.4 L min^{-1} containing 45–50 % relative humidity. Toluene was injected using a syringe pump in the vertical mixing chamber. The flow rate of liquid toluene was $0.25 \mu\text{L min}^{-1}$. The mixed feed consisted of dry air, humidified air and toluene. The 0.1 g of photocatalyst powder was loaded into the reactor cell for each run. During the preparation period of the mixed gas stream, it flowed from the mixing chamber to the reservoir vessel, through the flow meter and the vent. After steady-state conditions were achieved the feed and the vent were closed and the pump for circulation of the gas stream through the second part of the photoreactor was switched on. The internal flow rate was increased until the catalyst particles were fluidized inside the photoreactor cell. An internal flow rate was usually between 1000 to 1400 mL min^{-1} . The UVA irradiation was started after achieving the adsorption/desorption equilibrium. To prevent heating of the gas stream in the course of photocatalytic reaction, the reservoir was thermostated by a water bath. The temperature of the circulating gas stream was maintained at $22 \pm 5 \text{ }^\circ\text{C}$ during each run of 10 h. The concentration of toluene was measured in constant time intervals of reaction. A sample of the gas mixture circulated by a diaphragm pump was injected by an automatic gas valve of the on-line GC-MS. The temperature and relative humidity were measured by the thermometer and the humidity meter, respectively (A1-SD1 Sensoren).

4.4.3.3. Gas chromatography-mass spectrometry (GC-MS) analysis

The concentration of the toluene was determined on-line by gas chromatography (GC) (Varian 3900) coupled with the mass spectrometer (Varian Saturn 2100 T) operating in an electron impact (EI) mode. The gas samples were injected through a six-port external injection GC valve (Varian CP740641) with a $250 \mu\text{L}$ automatic sample loop. Then the samples were transferred into a column (Varian CP-Porabound U with the diameter of 0.32 mm and length of 25 m). The gas chromatograph was equipped with a split injector. The flow rate of helium as a carrier gas was 1 mL min^{-1} . The injector was held at $250 \text{ }^\circ\text{C}$, the oven started at $30 \text{ }^\circ\text{C}$ and the temperature was increased with a gradient of $20 \text{ }^\circ\text{C min}^{-1}$ up to $150 \text{ }^\circ\text{C}$ and finally maintained constant for 10 min.

Two photos of the photoreactor set-up for in-situ GC-MS gaseous photocatalysis are presented in Figure 18.

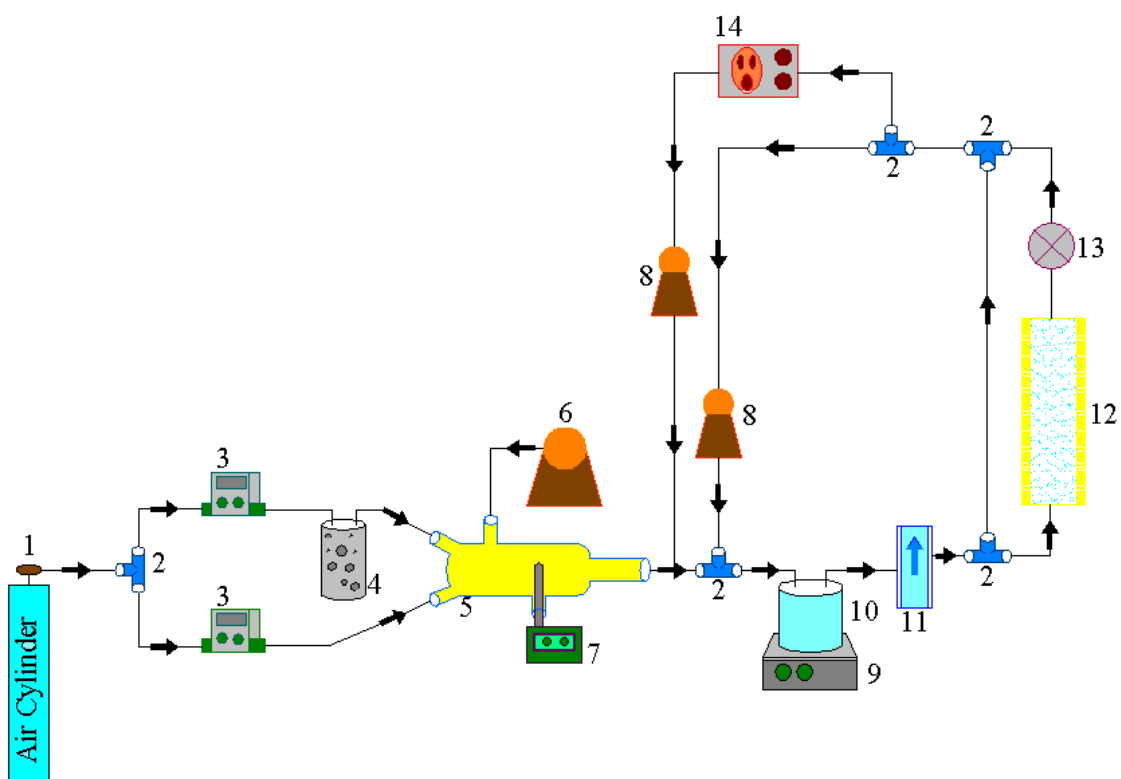
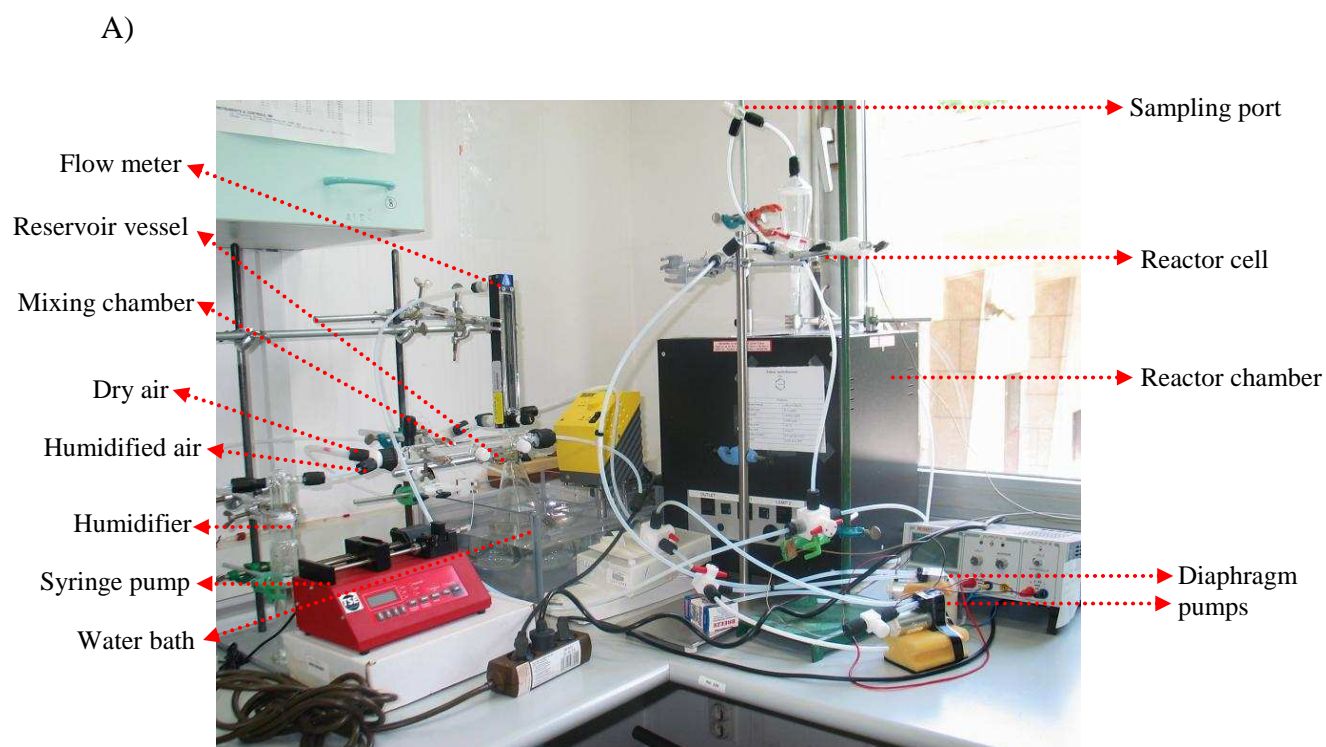


Fig 17: Schematic diagram of the set-up for in-situ GC-MS gaseous photocatalysis: (1) gas regulator, (2) 3-way valve, (3) mass flow meter/controller, (4) humidifier, (5) mixing chamber, (6) syringe pump, (7) thermometer and humidity meter, (8) diaphragm pump, (9) water bath, (10) reservoir vessel, (11) flow meter, (12) reactor cell with surrounding UVA lamps, (13) sampling port, (14) GC-MS



B)



Fig 18: (A) A photo of the photoreactor set-up for in-situ GC-MS gaseous photocatalysis; (B) GC-MS instrument

V. Results and discussion

5.1. Unsupported titania materials

5.1.1. XRD analysis

First, the X-ray diffraction analysis was performed on the raw TiO_2 sample before subjected to reflux treatment and without using any peptizing agent (acid) (Figure 19). As it can be seen, the composition of the white precipitate of neutralized TiCl_4 with ammonia solution is a mixture of mainly amorphous phase of TiO_2 with a small amount of anatase phase. The diffraction peaks with low intensity at $2\theta = 25.4^\circ$, 38.2° , 47.6° , 54.5° associated with (1 0 1), (1 1 2), (2 0 0) and (1 0 5) anatase reflections indicate a weak crystallinity of the powder.

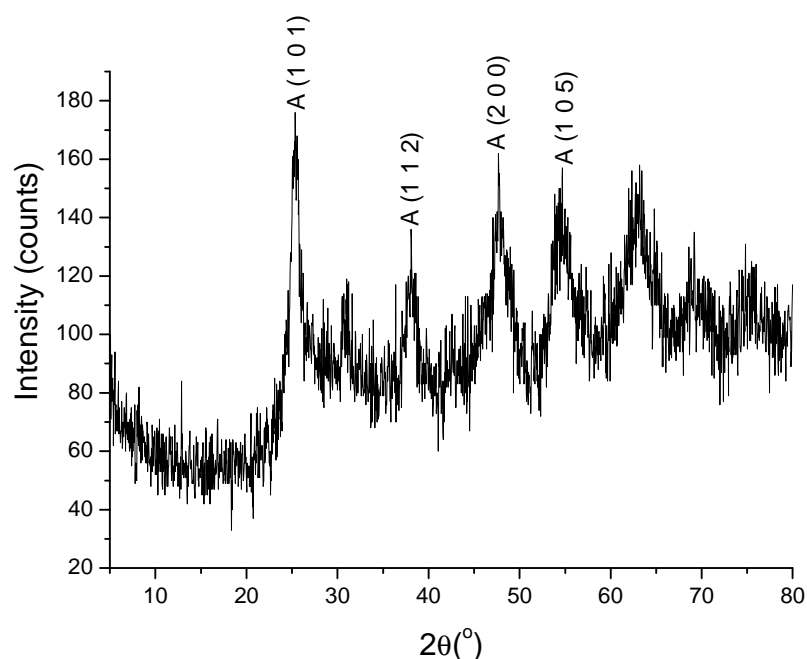


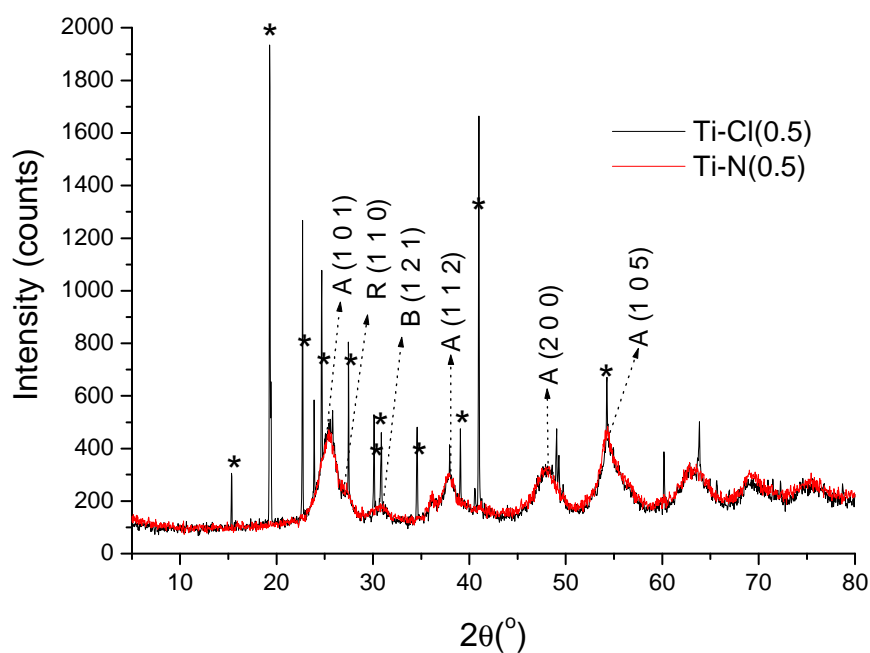
Fig 19: X-ray diffraction pattern of the precipitate obtained after neutralization of TiCl_4 and washing with water (A = anatase)

5.1.1.1. Impact of peptizing agent (acid)

The crystalline phases grow gradually by using acid and reflux in treatment of TiO_2 powders. The effect of the type of the acid, HNO_3 and HClO_4 , and the effect of the amount of $[\text{H}^+]$ ions on the crystallinity of pure TiO_2 were investigated. The X-ray

diffraction patterns in Figure 20 illustrate that the TiO_2 crystalline structures of Ti–N and Ti–Cl powders are quite similar although the sample prepared using HClO_4 contains additional sharp peaks of $\text{TiO}(\text{ClO}_4)_2 \cdot 6\text{H}_2\text{O}$ (JCPDS powder diffraction file 000–18–1410) superimposed on the broader anatase peaks. The existence of the peaks of $\text{TiO}(\text{ClO}_4)_2 \cdot 6\text{H}_2\text{O}$ originates from the interaction between $\text{Ti}(\text{OH})_4$ and HClO_4 . Ti–N(0.5) powders consist of anatase crystalline phase and small portion of rutile (evident by the shoulder peak at $2\theta = 27.1^\circ$) while for Ti–N(2.5) powder mainly anatase crystalline phase is evident. In addition, the small peak of brookite at $2\theta = 30.8^\circ$ appears in the patterns of all as-prepared powders (Figure 20).

a)



b)

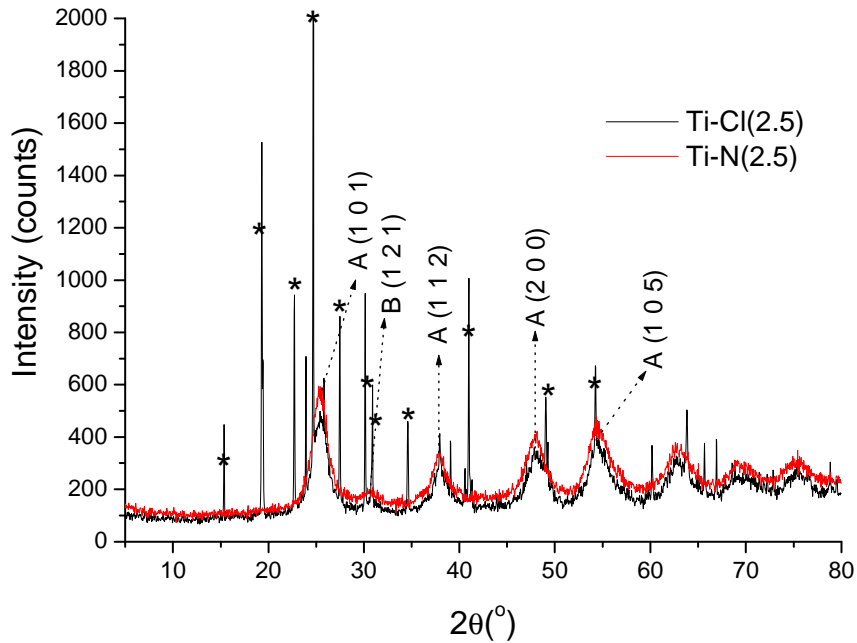
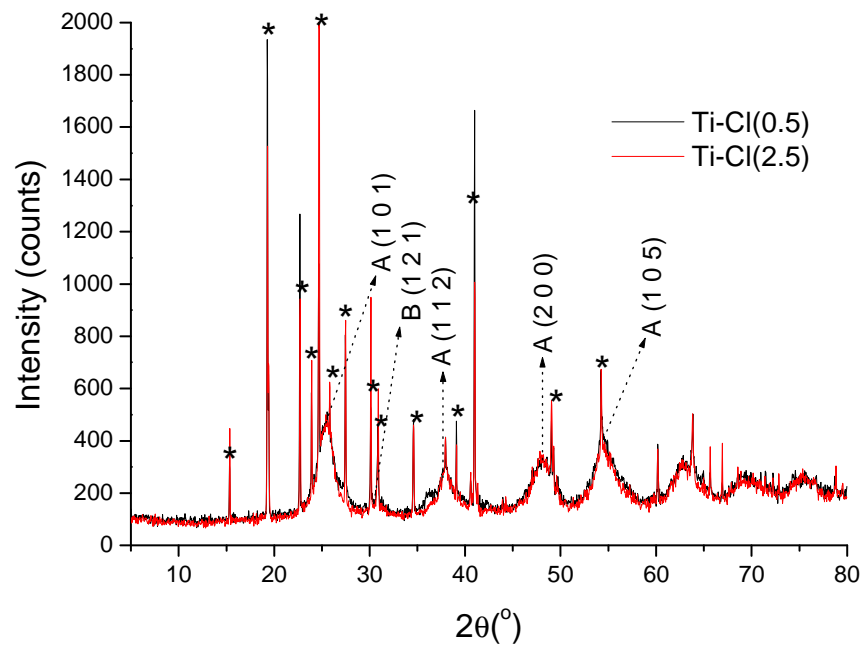


Fig 20: X–ray diffraction patterns of as–prepared samples Ti–N and Ti–Cl at the (a) $[\text{Ti}]/[\text{H}^+] = 0.5$; (b) $[\text{Ti}]/[\text{H}^+] = 2.5$ ratios (A = anatase, R = rutile, B = brookite, * = $\text{TiO}(\text{ClO}_4)_2 \cdot 6\text{H}_2\text{O}$)

5.1.1.2. Impact of the $[\text{Ti}]/[\text{H}^+]$ ratio

The X–ray diffraction patterns concerning the effect of the amount of acid (HNO_3 and HClO_4) used for peptizing the TiO_2 precipitate are shown in Figure 21. As it was shown previously, in HClO_4 –prepared powders, there is mainly anatase crystalline phase with small peak of brookite at $2\theta = 30.8^\circ$. The amount of $[\text{H}^+]$ ions had no significant effect on the crystal structure of the TiO_2 , except that some peaks of $\text{TiO}(\text{ClO}_4)_2 \cdot 6\text{H}_2\text{O}$ are sharper with $[\text{Ti}]/[\text{H}^+] = 0.5$ because of using higher amount of the acid. HNO_3 –prepared powders mostly consist of an anatase phase, however, by increasing the amount of acid (Ti–N(0.5) powder) the small portion of rutile phase becomes evident (shoulder peak at $2\theta = 27.1^\circ$).

a)



b)

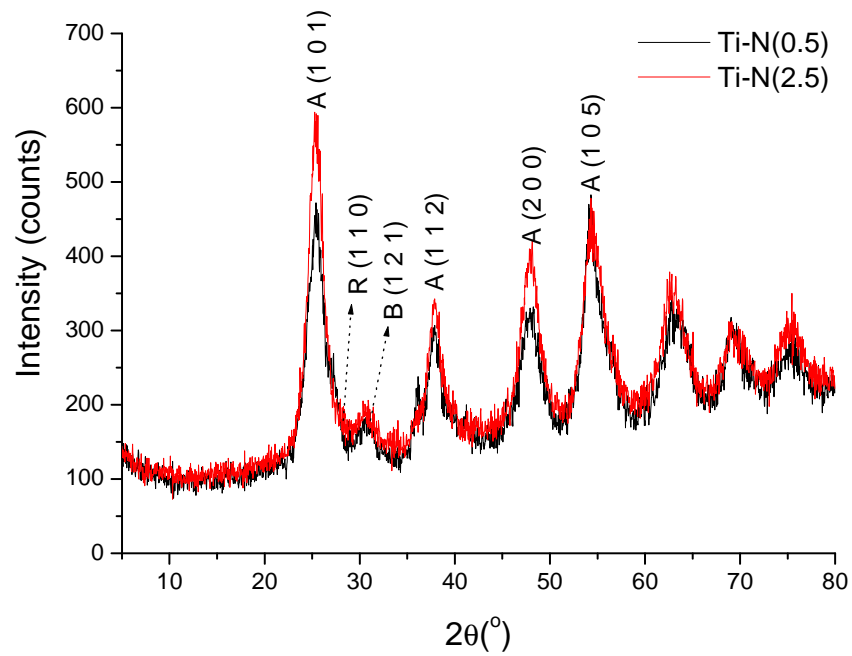
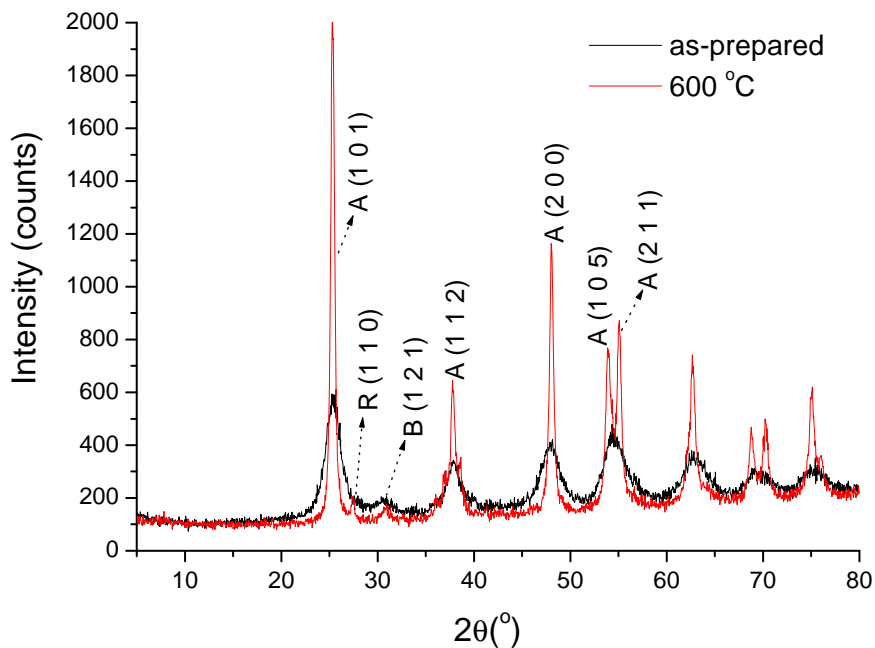


Fig 21: X-ray diffraction patterns of as-prepared samples (a) Ti-Cl(0.5), Ti-Cl(2.5); (b) Ti-N(0.5), Ti-N(2.5) (A = anatase, R = rutile, B = brookite, * = $\text{TiO}(\text{ClO}_4)_2 \cdot 6\text{H}_2\text{O}$)

5.1.1.3. Impact of calcination temperature

The X-ray diffraction patterns for as-prepared and calcined TiO₂ powders are shown in Figures 22 and 23. As expected, the crystalline phases grow by heat treatment. Ti-N(2.5) powders consist of a very small portion of rutile phase after calcination at 600 °C. However, Ti-N(0.5) powders with higher amount of acid consist of the mixture of anatase and rutile phases while the peaks are gaining in intensity with the heat treatment. The phase transformation from anatase to rutile for the Ti-N(0.5) powder started even at lower calcination temperature (400 °C). In fact, thermal analysis (TGA-DSC) of Ti-N(0.5) shows that after heat treatment above 400 °C the weight remained constant, however, DSC shows a broad exothermic peak which is ascribed to the phase transformation from anatase to rutile (section 5.1.6.). The small peak of brookite at $2\theta = 30.8^\circ$ is evident in all diffraction patterns which intensity is not increased by calcination.

a)



b)

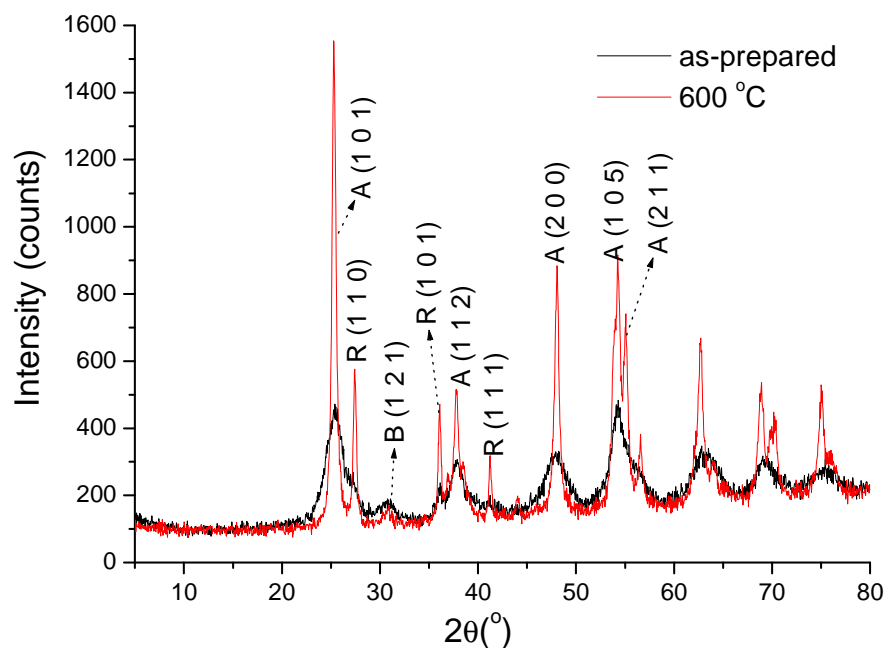
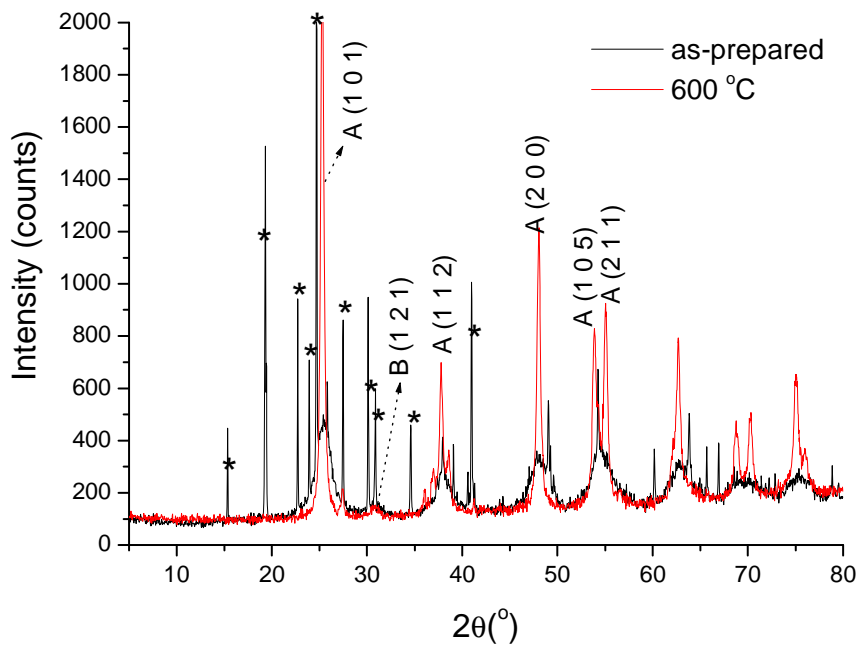


Fig 22: X-ray diffraction patterns of samples before and after calcination at 600 °C (a) Ti-N(2.5); (b) Ti-N(0.5) (A = anatase, R = rutile, B = brookite)

In HClO_4 -prepared samples the TiO_2 crystallinity gradually grows by calcination treatment as in the case of HNO_3 -prepared powders. Ti-Cl powders consist of mainly anatase phase even after heat treatment (the small peak of brookite phase is evident at $2\theta = 30.8^{\circ}$) however, by increasing the amount of acid, Ti-Cl(0.5) powder, the intensity of the small peak of rutile is increased by calcination treatment. Calcination treatment has significant effect on $\text{TiO}(\text{ClO}_4)_2 \cdot 6\text{H}_2\text{O}$ peaks. By using high calcination temperature, this compound is decomposed and corresponding peaks disappeared as well (Figure 23).

a)



b)

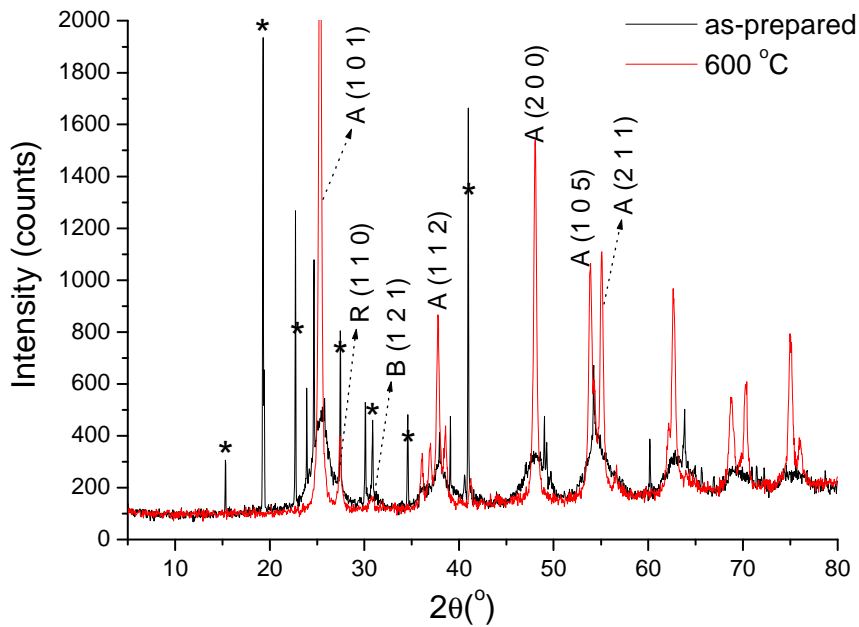


Fig 23: X-ray diffraction patterns of samples before and after calcination at 600 °C (a) Ti-Cl(2.5); (b) Ti-Cl(0.5) (A = anatase, R = rutile, B = brookite, * = $\text{TiO}(\text{ClO}_4)_2 \cdot 6\text{H}_2\text{O}$)

The crystallite sizes of unsupported TiO₂ samples determined by the Scherrer's equation are in the range from 4 to 8 nm for the as-prepared powders and in the range from 17 to 30 nm for calcined powders (Table 4). The grain sizes obtained by the Scherrer formula are actually the effective sizes of coherently scattering domains and the values in as-prepared samples are small and similar in size for different samples.

Table 4: Crystallite sizes (obtained by XRD) and particle sizes in solution (obtained by DLS)

Sample	Crystallite size before calcination (nm)	Crystallite size after calcination at 600 °C (nm)	Particle size of non-calcined powders in aqueous solution (nm)
Ti-Cl(0.5)	5	30	36
Ti-Cl(2.5)	8	25	32
Ti-N(0.5)	4	17	79
Ti-N(2.5)	6	20	–

5.1.2. Dynamic light scattering

The sizes of aggregated TiO₂ particles in the colloidal suspension solution were measured by DLS technique (Table 4). It has to be stressed that the particle sizes were measured under exactly the same conditions as they were used in a photocatalytic test, because a correlation between the particle size and the photocatalytic activity was tried to be found out. For this purpose, dried TiO₂ powder (at 150 °C) was dispersed in acidified water with pH value of 2.8 to obtain the concentration of TiO₂ in the measured sol equal to 1 g L⁻¹. The particle sizes of non-calcined powders in aqueous solution are evidently much bigger than the corresponding crystallite sizes, which were measured from XRD patterns and calculated by Scherrer's equation. The sizes of the particles from HClO₄-based TiO₂ sols were approximately twice smaller (between 32 to 36 nm) than the sizes of the particles from HNO₃-based sols (79 nm). Although the sizes of crystallites are similar in case of HNO₃ as well as in HClO₄ based TiO₂, we can conclude that the perchloric acid has better peptizing characteristics than nitric acid, because it resulted in solutions with less aggregated particles. The sizes of the measured particles did not depend much on the [Ti]/[H⁺] ratio, when the same acid was studied.

5.1.3. UV-vis spectra

5.1.3.1. UV-vis transmittance

Figure 24 presents the UV-vis transmittance spectra after Kubelka–Munk transformation of the sols used in photocatalytic experiments, i.e. the colloidal suspensions of dried TiO_2 powders in water with the concentration of TiO_2 set at 1 g L^{-1} . 1 mm quartz cell was used to present more clearly the optical characteristics of the sol. The transmittance spectra of Ti–N(2.5) and Ti–Cl(2.5) were skipped out of the figure, because they are almost identical to their counterparts with the different $[\text{Ti}]/[\text{H}^+]$ ratio. The Ti–Cl(0.5) sol scatters visible light just minorly. On the contrary, scattering of radiation can not be neglected in case of Ti–N(0.5) sol, which contains larger colloidal particles. The transmittance of the sol correlates well with the particle size. The decrease of transmittance below 400 nm belongs to the band gap of anatase TiO_2 . Lower transmittance of the Ti–N(0.5) sol in this range does not correspond to the red shift of the band gap of TiO_2 , but this difference between transmittances of both samples in this range belongs to the scattered and reflected radiation, which does not reach the detector of the spectrometer.

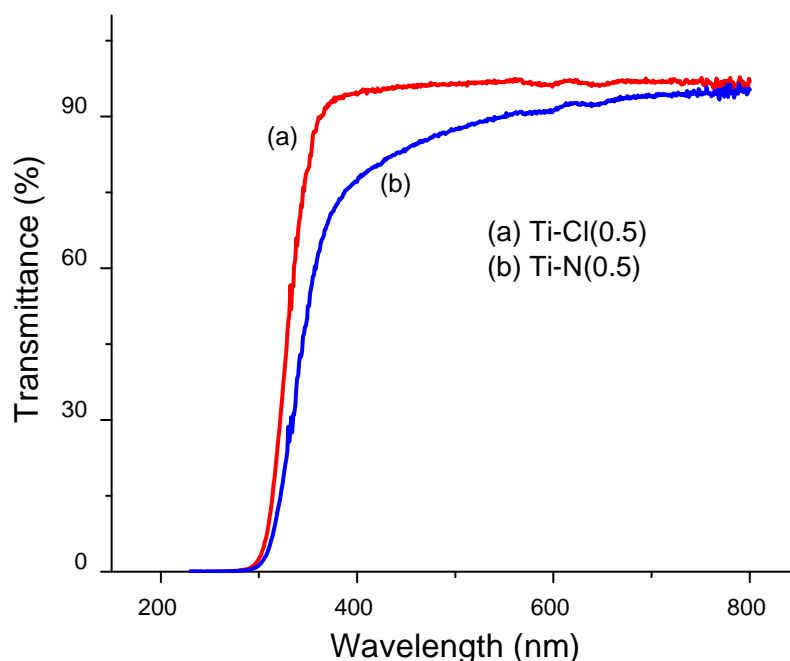
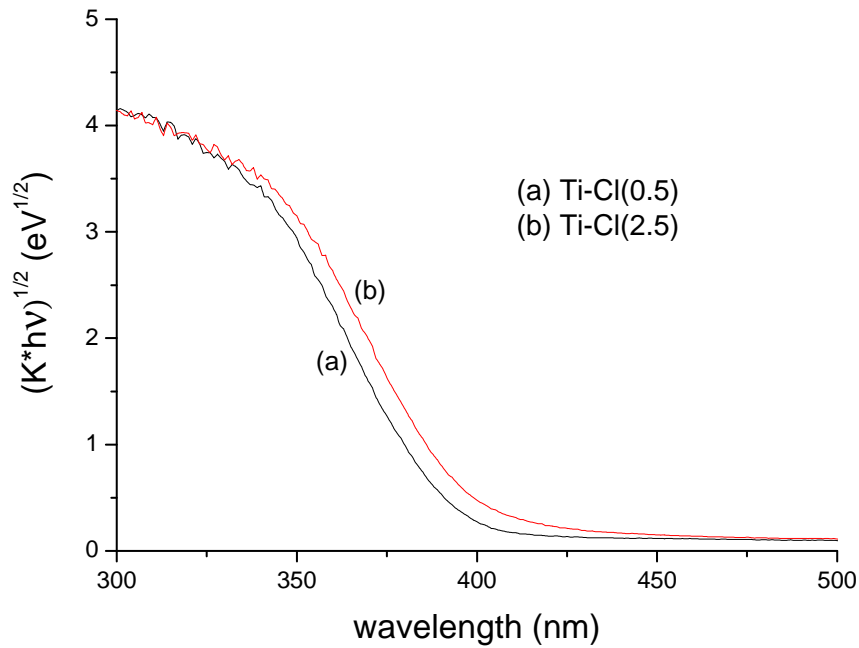


Fig 24: UV-vis transmittance spectra of the colloidal solutions (the same as used for the photocatalytic experiments) made from as-prepared powders: (a) Ti–Cl(0.5); (b) Ti–N(0.5)

5.1.3.2. UV-vis diffuse reflectance

The UV-vis diffuse reflectance spectra of HClO_4 -prepared powders are shown in Figure 25(a). As it is clearly observed, the spectra are red shifted by increasing the amount of $[\text{Ti}]/[\text{H}^+]$ from 0.5 to 2.5. By calcination treatment of $\text{Ti-Cl}(0.5)$ at 400°C and 600°C , as it is shown in Figure 25(b), the spectra are also red shifted. The band-gap energies determined for $\text{Ti-Cl}(0.5)$, $\text{Ti-Cl}(2.5)$ and calcined $\text{Ti-Cl}(0.5)$ at 400°C and 600°C are reported in Table 5. The results are well correlated with the crystallite sizes. When the $[\text{Ti}]/[\text{H}^+]$ ratio changed from 0.5 to 2.5, the crystallite sizes of Ti-Cl powders increased from 5 to 8 nm, subsequently the band-gap energies decreased from 3.16 to 3.11 eV. By calcination treatment of $\text{Ti-Cl}(0.5)$ the crystallite sizes are increased following a decrease of the band-gap energies from 3.16 to 3.05 eV.

a)



b)

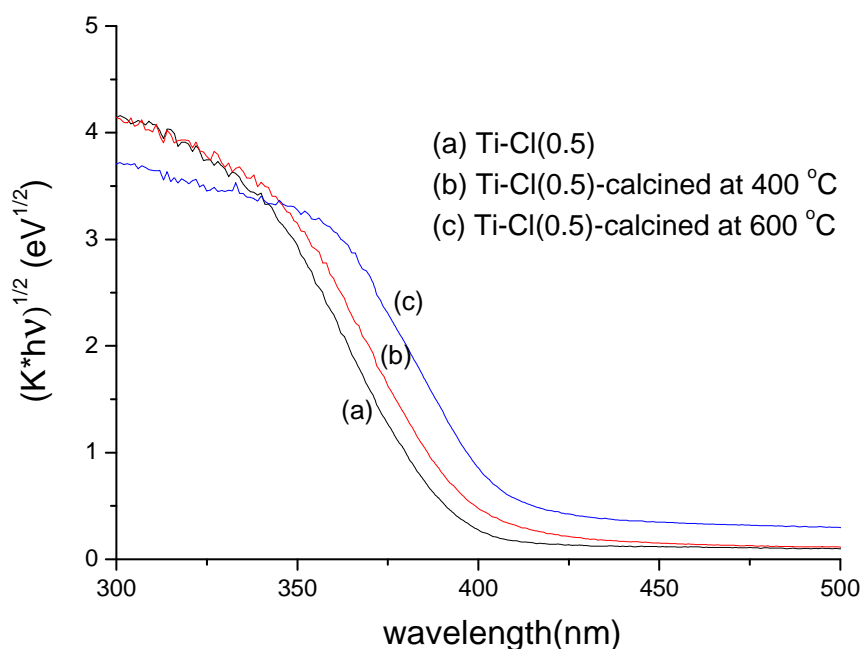


Fig 25: DR UV-vis spectra of (a) Ti-Cl(0.5) and Ti-Cl(2.5); (b) Ti-Cl(0.5), calcined Ti-Cl(0.5) at 400 °C and 600 °C

5.1.4. Nitrogen-sorption measurement

The surface area, pore volume and mean pore size of as-prepared and calcined powders are shown in Table 5. The TiO_2 powders after drying were used for the measurements. It is evident from Table 5 that for the powders with the same $[\text{Ti}]/[\text{H}^+]$ ratio the specific surface areas of HClO_4 -prepared powders are approximately two times higher ($98.0 \text{ m}^2 \text{ g}^{-1}$) than those of the HNO_3 -prepared powders ($46.4 \text{ m}^2 \text{ g}^{-1}$). The difference in the specific surface area of the samples prepared using the same acid, but a different $[\text{Ti}]/[\text{H}^+]$ ratio is not significant. The surface area results correlate well with the DLS results. If we assume that the colloid particles have spherical shapes, then the particles with the diameter two times larger will have half the surface area if the mass concentration, i.e. the density of the material, is the same and if the porosity is small. All conditions are fulfilled in our case and the comparison between the DLS and BET specific surface area indicate that even in the powder form the colloidal particles do not aggregate.

After calcination treatment at 400 °C, the surface area of the Ti-N powders was increased significantly but it is not the same for Ti-Cl powders. By increasing the

calcination temperature up to 600 °C, the surface area of the all powders decreased drastically.

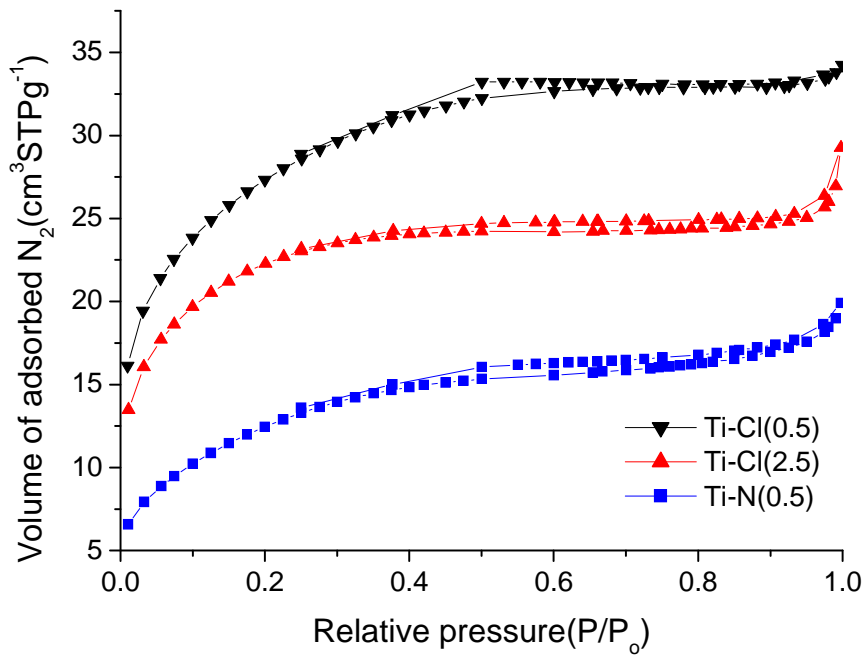
The adsorption–desorption isotherm curves for the as–prepared samples and calcined samples at 400 °C are shown in Figure 26. All isotherm curves can be classified as the type IV adsorption isotherm (Sing et al., 1985) indicating mesoporous structure for both types of samples. This type of isotherm is classified for materials without or with small part of micropores. The hysteresis loop for as–prepared samples is of the type H4 which is often associated with narrow slit–like pores. However, the hysteresis loop for the calcined samples is like H2 type that shows that the distribution of pore size and shape is not well defined (Sing et al., 1985).

Table 5: Surface area, pore volume, pore size and band–gap energy of as–prepared and calcined powders

Sample	Surface area (m ² g ⁻¹)	*Pore volume (cm ³ g ⁻¹)	Pore size (nm)	Band gap (eV)
Ti–Cl(0.5)	98	0.053	2.2	3.16
Ti–Cl(2.5)	80	0.045	2.3	3.11
Ti–N(0.5)	46	0.031	2.65	3.22
Ti–N(2.5)	158	0.137	3.5	–
Ti–Cl(0.5)(400 °C)	85	0.099	4.6	3.11
Ti–Cl(2.5)(400 °C)	94	0.103	4.3	–
Ti–N(0.5)(400 °C)	126	0.124	3.9	–
Ti–N(2.5)(400 °C)	117	0.111	3.8	–
Ti–Cl(0.5)(600 °C)	22	0.043	7.8	3.05
Ti–Cl(2.5)(600 °C)	30	0.053	7.1	–
Ti–N(0.5)(600 °C)	48	0.091	7.5	–
Ti–N(2.5)(600 °C)	41	0.123	12.0	–

*Single point adsorption total pore volume of pores less than 1343 nm at p/p° = 0.998578917.

a)



b)

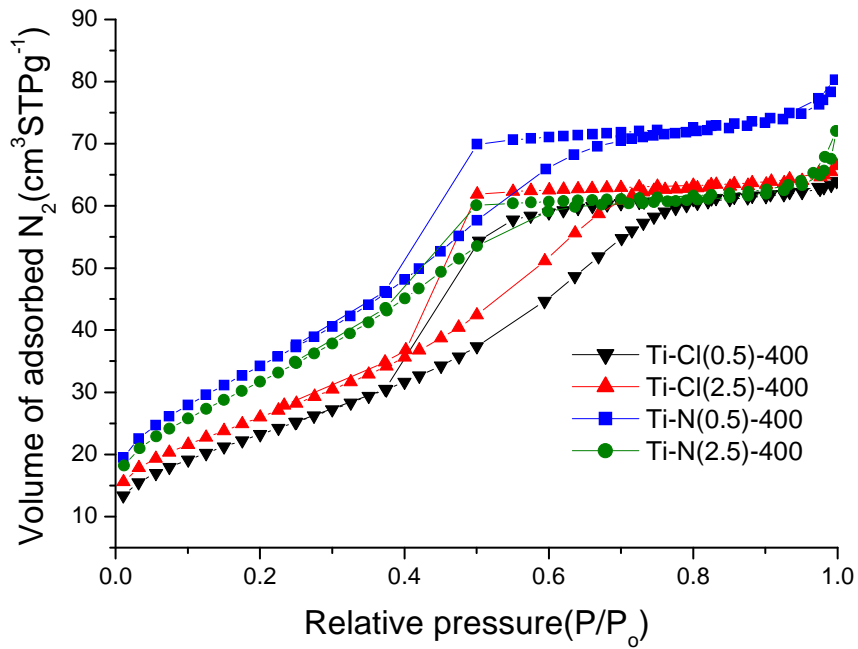
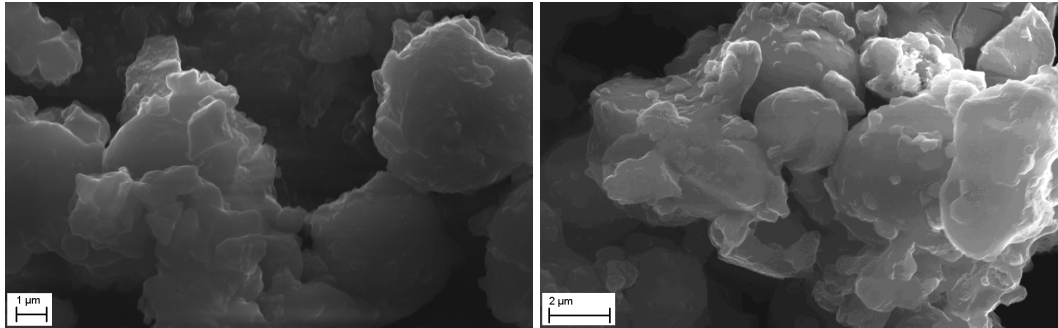


Fig 26: The adsorption–desorption isotherm curves for the titania samples; (a) before calcination; (b) calcined at 400 °C

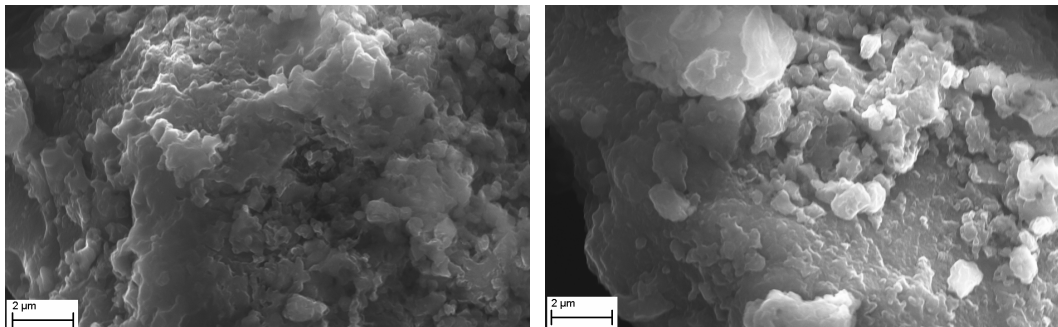
5.1.5. Scanning electron microscopy of titania powders

The morphology of the Ti-Cl(0.5), Ti-Cl(2.5) and Ti-N(0.5) powders are shown in Figure 27 while SEM micrographs for the Ti-Cl(0.5) and Ti-N(0.5) powders calcined at 400 °C are shown in Figure 28. As it is demonstrated, in all prepared powders (Ti-Cl and Ti-N) we deal with the aggregated particles. HClO₄-preped powders consist of formless particles which have been fused together. It seems that by increasing the amount of acid in HClO₄-prepared powders, the small particles agglomerate on the big particles (the powder consists of small and big particles). The sizes of the particles in Ti-Cl(2.5) powder are smaller compared to Ti-Cl(0.5) powder. However, by calcination the sizes of the particles do not differ significantly. In HNO₃-prepared powder, as it is shown, the size of the particles is grown after calcination while the particles are spherical before and after calcination. The important point is that the size of the particles dispersed in aqueous solution (Table 4) is much lower than the size of powder aggregates, which is due to the acid that provides charging of colloidal particles in solution.

a)



b)



c)

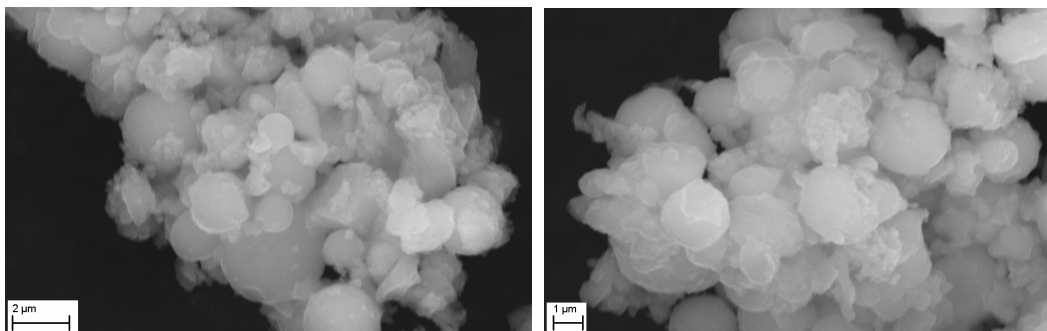
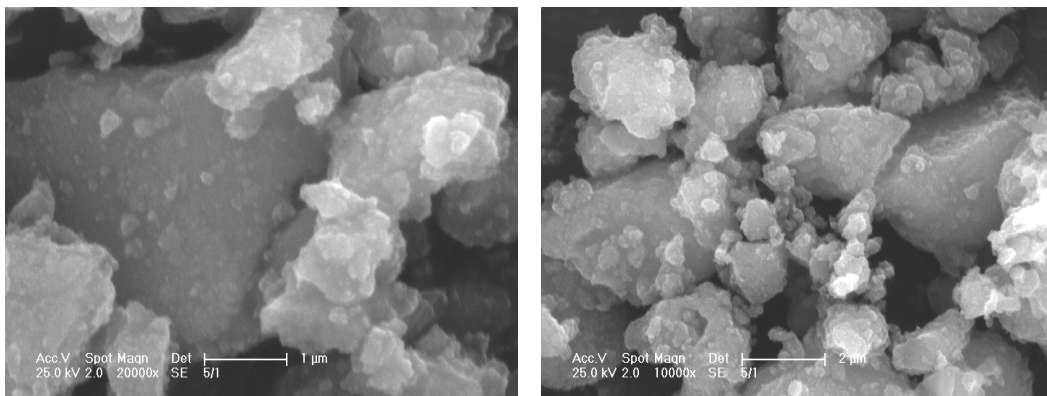


Fig 27: SEM micrographs of powders (a) Ti-Cl(0.5); (b) Ti-Cl(2.5); (c) Ti-N(0.5)

a)



b)

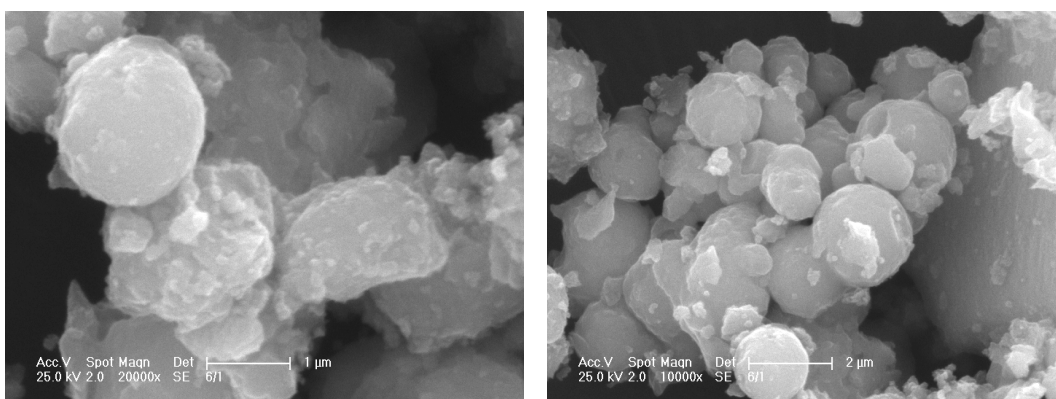


Fig 28: SEM micrographs of calcined powders at 400 °C (a) Ti-Cl(0.5); (b) Ti-N(0.5)

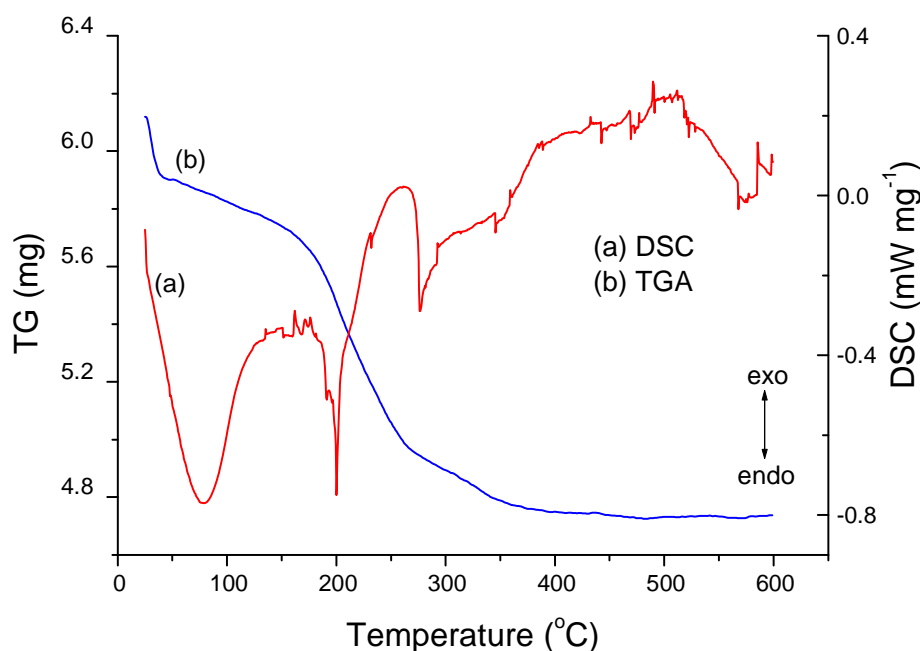
5.1.6. Thermal analysis (TGA-DSC)

TGA and DSC curves of Ti-N(0.5) and Ti-Cl(0.5) powders are shown in Figure 29. The first weight loss of the Ti-N(0.5) powder (approximately 5 %) takes place in the temperature range of 27–150 °C and is attributed to desorption and evaporation of

water molecules. In the DSC curve this process corresponds to an endothermic peak with a minimum positioned at 80 °C. The second weight loss of about 15 % occurs in the temperature range of 170–355 °C and coincides with two endothermic peaks in the DSC curve. In this temperature range nitrates thermally decompose. Above 400 °C the weight of the powder remains constant and a broad exothermic peak between 400 and 600 °C in the DSC curve is ascribed to the phase transformation from anatase to rutile (Figure 29(a)).

Ti-Cl(0.5) powder loses around 9 % of its weight when heated from room temperature up to 200 °C due to the loss of adsorbed water (Figure 29(b)). Additional weight loss of around 9 % takes place in the temperature range from 200 to 250 °C and can be ascribed to two simultaneous reactions, the dehydration of $\text{TiO}(\text{ClO}_4)_2 \cdot 6\text{H}_2\text{O}$ and the evolution of water molecules formed during condensation process. The sharp exothermic peak with a maximum at 330 °C in the DSC curve and the accompanying weight loss of ca. 19 % is attributed to the decomposition of $\text{TiO}(\text{ClO}_4)_2$. Upon releasing perchlorates, this compound should be transformed into TiO_2 and subsequently crystallized, but the associated exothermic process is very poorly expressed in the DSC curve.

a)



b)

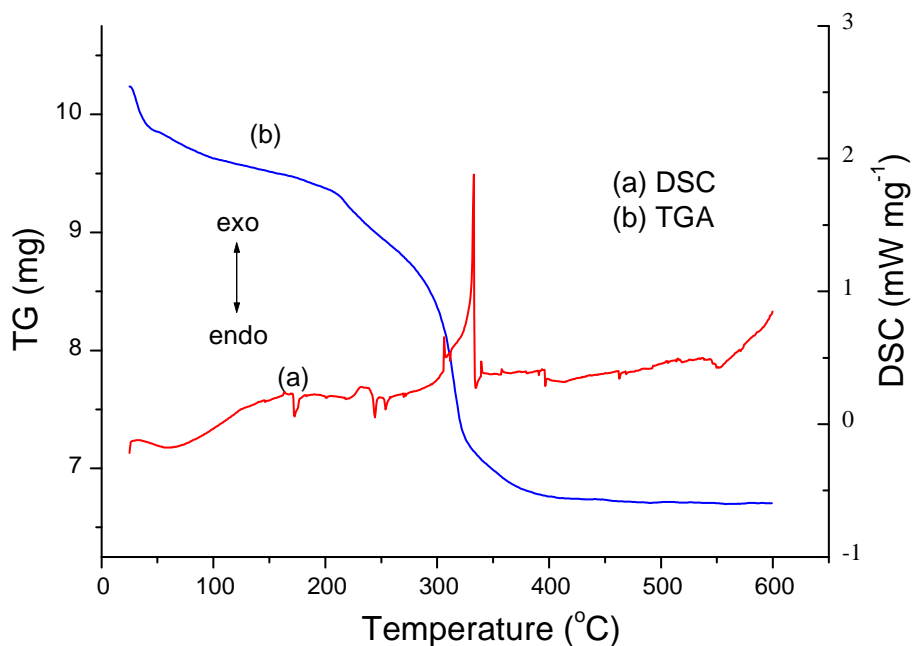


Fig 29: TGA–DSC analysis of (a) Ti–N(0.5); (b) Ti–Cl(0.5) powders

5.1.7. Photocatalytic degradation of phenol

Figure 30 shows the photocatalytic degradation of phenol in the presence of the TiO₂ colloids. As expected, there is no significant degradation of phenol for the experiments carried out in absence of catalyst under UV radiation. The disappearance curves indicate the zero–order degradation kinetics. It seems that the concentration of the phenol in solution is not the rate–determining in this case. If we suppose that the degradation of phenol occurs predominantly on the surface of TiO₂, the constant surface coverage (which is equal to 1) by phenol molecules is a prerequisite for the zero–order degradation kinetics. Obviously the dissolved concentration of phenol in our degradation experiments is high enough (it is above 15 mg L⁻¹) so that the coverage of the catalyst surface by phenol molecules is complete at least in the initial steps of degradation. This is confirmed also with the data in Figure 30, where the zero–order degradation kinetics is no longer obeyed after the phenol concentration drops below one third of the initial concentration (Tasbihi et al., 2009).

The zero-order degradation rate constants of phenol in the presence of different powders are listed in Table 6.

Table 6: The zero-order degradation rate constants of phenol in the presence of different powders

Sample	rate constant, k ($\text{mg L}^{-1} \text{min}^{-1}$)
Ti-Cl(0.5)	0.767
Ti-Cl(2.5)	0.645
Ti-N(0.5)	0.362
Ti-N(2.5)	0.436
Ti-Cl(2.5)(400 °C)-milled	0.228
Ti-Cl(2.5)(400 °C)-non-milled	0.205
Ti-N(0.5)(400 °C)-milled	0.213
Ti-N(0.5)(400 °C)-non-milled	0.229

It is evident from Figure 30 that the type of acid has a higher effect on the photocatalytic activity of the prepared samples than the $[\text{Ti}]/[\text{H}^+]$ ratio. The HClO_4 -prepared powders show approximately a 1.5 times higher photocatalytic activity than the HNO_3 -prepared powders regardless the $[\text{Ti}]/[\text{H}^+]$ ratio. It is known that the photocatalytic activity of TiO_2 is a function of many physico-chemical characteristics of the material (crystal structure, crystallite size, particle size, surface area...). The rate of degradation of the phenol molecule may differ if individual or aggregated anatase particles are involved in the photocatalysis. For instance, if the aggregated particles are involved then the charge transfer from the center to the surface of the particle is certainly facilitated in smaller aggregates with a smaller number of primary particles. The other difference is in the degradation kinetics results. The zero-order degradation rate indicates that the phenol has to be preadsorbed on the surface of the colloidal particles before it is degraded, which increases the importance of colloidal surface area and makes it an important parameter affecting the photocatalytic activity. Actually, the colloidal particle size could be the linking parameter in the studied system. Smaller colloidal particles lead to a higher surface area and consequently more phenol molecules can be adsorbed on the titania surface.

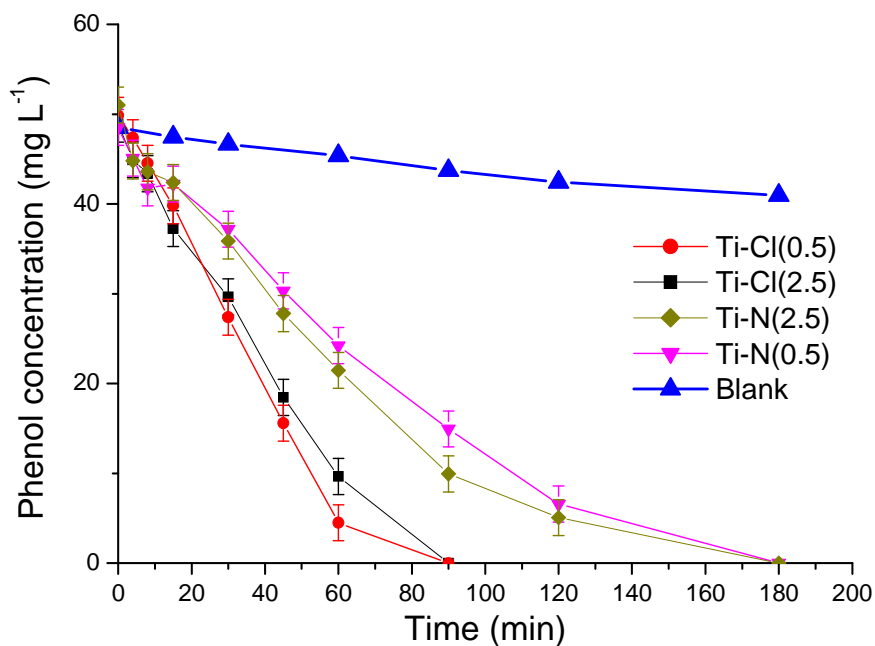


Fig 30: Photocatalytic degradation of phenol by using different as-prepared powders

The photocatalytic experiments were also done for the samples Ti-Cl(0.5) and Ti-Cl(2.5) calcined at 400 °C. The results showed that the photocatalytic activity of these powders (Figure 31) is lower as compared to the powders before calcination. This behavior could be related to the bigger particle size of powders (evident also from SEM micrographs (μm -sized particles) (Figure 28(a)) due to the sintering of the particles after calcination treatment. We tried to mill these calcined powders to make them finer as much as possible. Unfortunately, there were not significant differences between non-milled and milled powders as it is shown in Figure 31. It seems that physical milling of the particles cannot promote the photocatalytic activity.

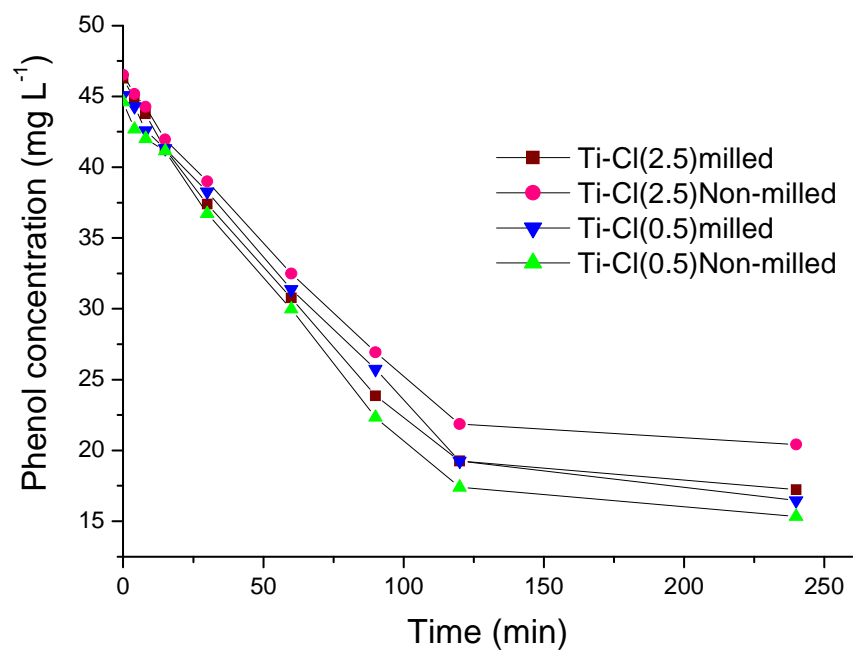


Fig 31: Photocatalytic degradation of phenol for HClO₄-prepared powders calcined at 400 °C

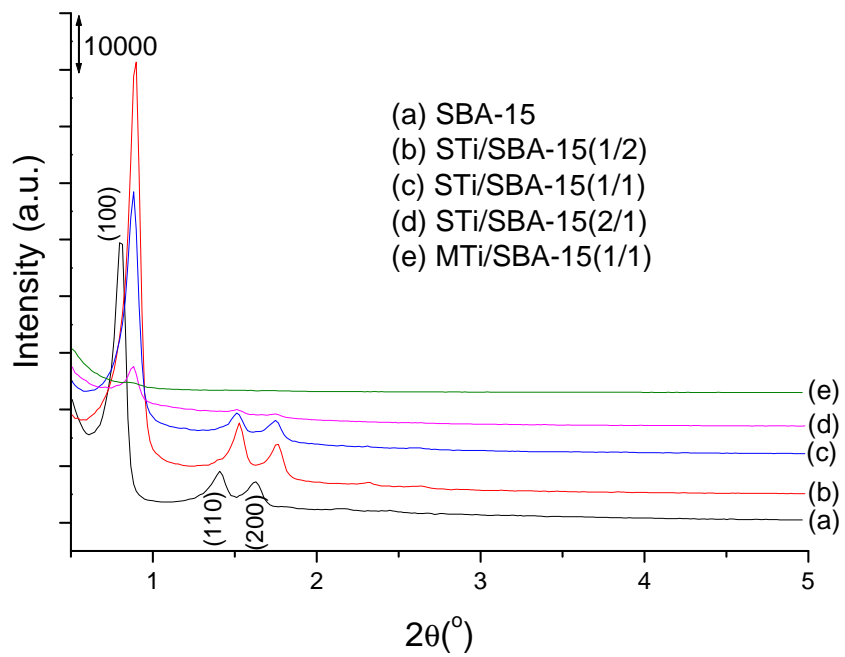
5.2. Titania/silica powders

5.2.1. XRD analysis

5.2.1.1. Small-angle XRD analysis

The maintenance of the support framework order upon impregnation of titania and the effect of increasing the molar ratio was studied by the analysis of the small-angle range XRD patterns. The small-angle X-ray powder diffraction patterns in the range of $0.5^\circ < 2\theta < 5^\circ$ are illustrated in Figure 32. In Figure 32(A) the SBA-15 diffractogram illustrates three diffraction peaks corresponding to the (1 0 0), (1 1 0) and (2 0 0) reflections typical for 2D-hexagonal pore arrangement with $p6mm$ symmetry. However, it can be seen in Figure 32(A) that after loading of titania on SBA-15 in samples STi/SBA-15(x), the diffraction peaks are still present and their 2θ values are only slightly shifted, indicating that the channels with good order are maintained during preparation procedure; though, the intensity of peaks is decreased by increasing the Ti/Si molar ratio and in the STi/SBA-15(2/1) it becomes low. It is believed that the presence of titania could lead to random collapse of the mesoporous channels (Busuioc et al., 2006). The most intense (1 0 0) diffraction peak was used to calculate the unit cell dimensions (Calleja et al., 2002; Ding et al., 2005; Wang and Song, 2006), which are reported in Table 7. The titania loading influences d_{100} and the unit cell dimensions for the STi/SBA-15(x) powders. However, the near retention of unit cell dimensions indicates that the structure of SBA-15 is maintained during the loading of titania, confirming that the hexagonal SBA-15 is stable (Grieken et al. 2002; Ding et al., 2005). For the MTi/SBA-15(1/1) powder, as it is shown in Figure 32(A), introduction of hydrolyzed Ti-isopropoxide strongly reduced the intensity of the low-angle diffraction peaks. Thus it can be assumed that this synthetic approach, which started from Ti-isopropoxide as a precursor and required an additional calcination step, was more detrimental to the silica framework structure (Busuioc et al., 2006; Grieken et al., 2002). This statement was also confirmed by SEM as it is shown in section 5.2.4. The low-angle XRD patterns of KIL-2, MTi/KIL-2(1/1) and STi/KIL-2(x), as shown in Figure 32(B), do not exhibit any peaks, indicating that the KIL-2 materials had a disordered mesoporous structure (Novak Tušar et al., 2010).

A)



B)

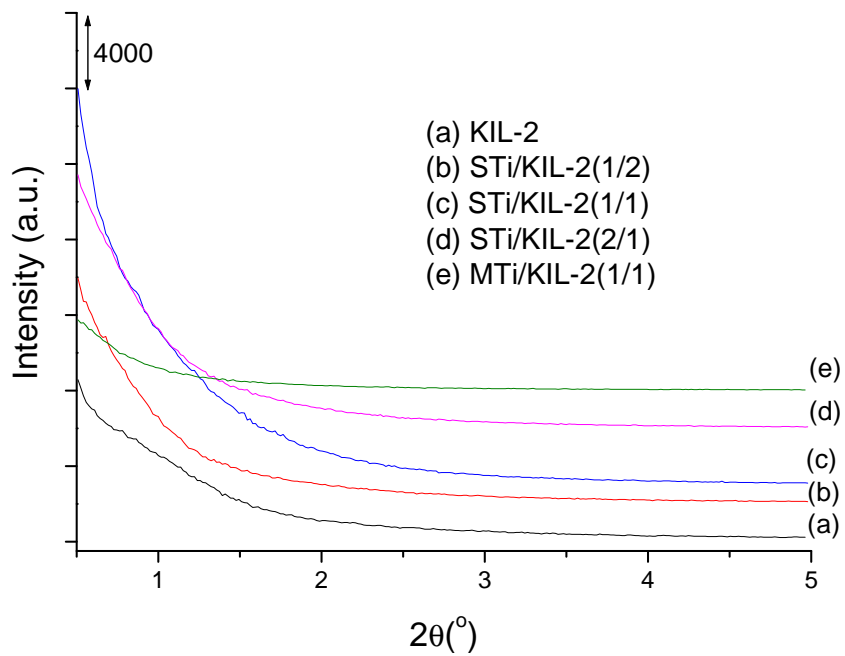
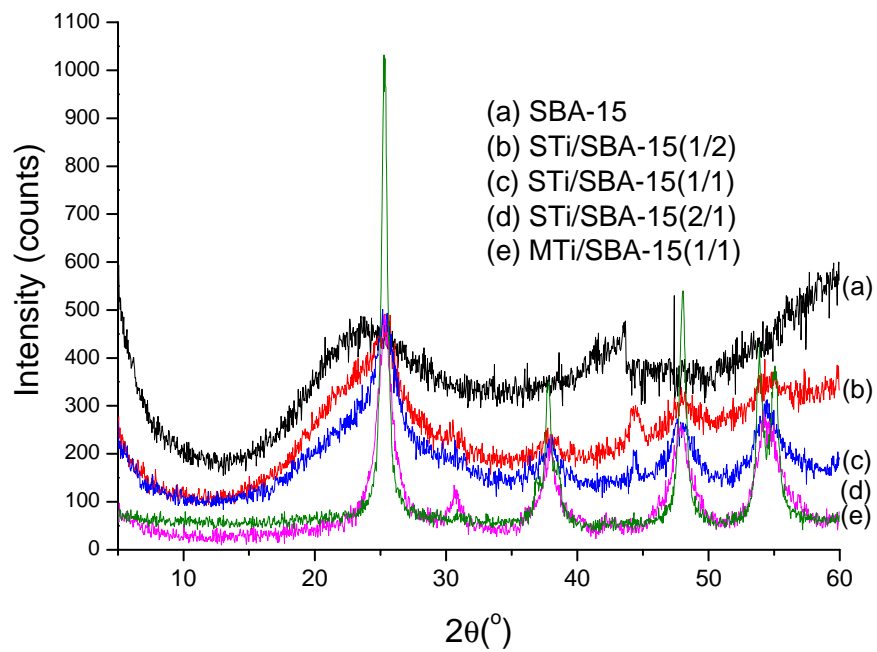


Fig 32: Small-angle X-ray powder diffraction (XRD): (A) SBA-15, STi/SBA-15(x), MTi/SBA-15(1/1); (B) KIL-2, STi/KIL-2(x), MTi/KIL-2(1/1)

5.2.1.2. Wide-angle XRD analysis

The X-ray diffractograms recorded in the wide-angle range ($5^\circ < 2\theta < 60^\circ$) are displayed in Figure 33. They confirm that in both types of mesoporous silica powders, SBA-15 and KIL-2, anatase is the major crystalline phase in all prepared powders, as indicated by the peaks emerging at $2\theta = 25.3^\circ, 37.8^\circ, 48.1^\circ, 53.9^\circ, 55.1^\circ$ associated with (1 0 1), (0 0 4), (2 0 0), (1 0 5), (2 1 1) anatase diffractions, respectively. The wide-angle XRD spectra of SBA-15 and KIL-2 possess one broad peak at 2θ around 23° corresponding to glass-like amorphous silicate nanoparticles while the crystalline titania phase is growing gradually by incorporation of titania. As can be seen in Figures 33(A) and (B), the intensity of peaks is increased by increasing the Ti/Si molar ratio. It is important to mention that there is no difference in the position of the anatase peaks between the unsupported titania and silica-titania powders. In addition, by increasing the amount of titania, the presence of a brookite phase with a small peak at $2\theta = 30.8^\circ$ becomes evident (Lavrenčič Štangar et al., 2006). For the MTi/SBA-15(1/1) and MTi/KIL-2(1/1) powders, the anatase peaks are the strongest and sharpest compared to the other prepared samples which is a consequence of the different preparation procedure. In this case the grafting and growth of crystalline titania is obviously less disturbed by the host sites and additionally it forces the SBA-15 meso-ordered structure to collapse or it blocks the mesopores to such an extent that the low-angle diffraction peaks no longer appear (Figure 33(A)). It is worthwhile mentioning that we did X-ray measurements for the STi/SBA-15(1/1) and STi/KIL-2(1/1) samples after calcination at 300°C for 6 h as well. There was no significant difference noted between non-calcined and calcined samples (Figure 34).

A)



B)

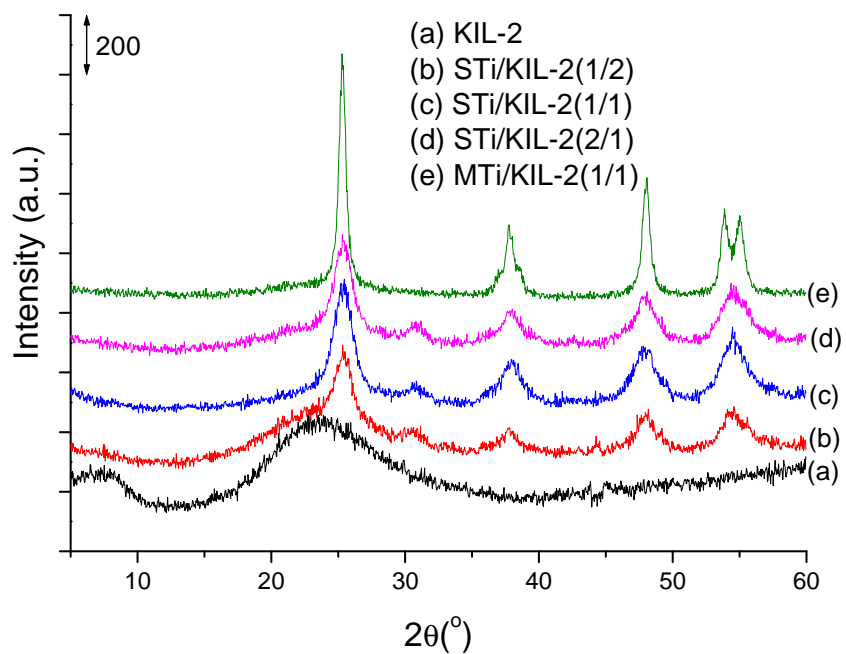
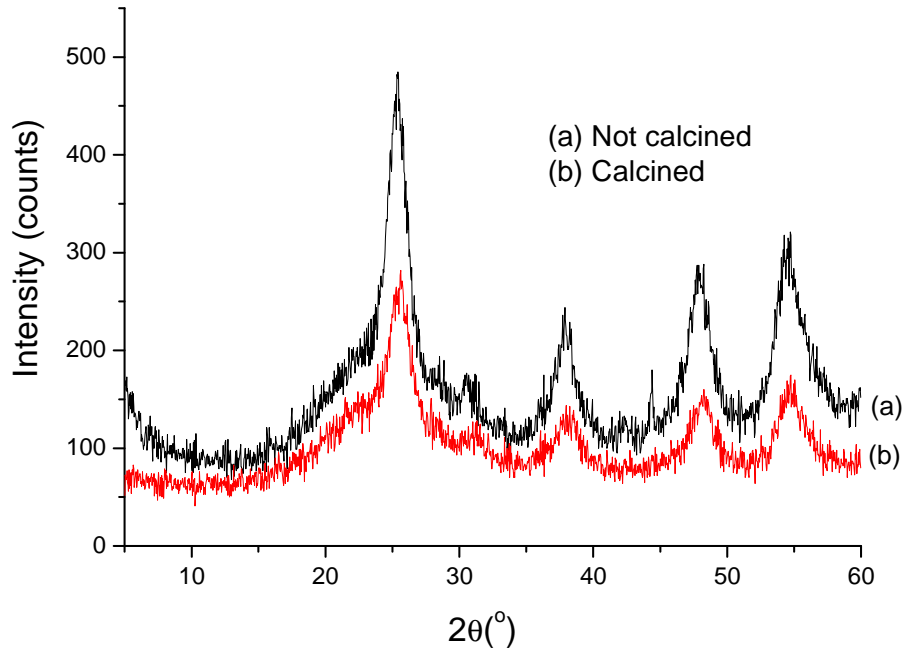


Fig 33: Wide-angle X-ray powder diffraction (XRD): (A) SBA-15, STi/SBA-15(x), MTi/SBA-15(1/1); (B) KIL-2, STi/KIL-2 (x), MTi/KIL-2(1/1)

A)



B)

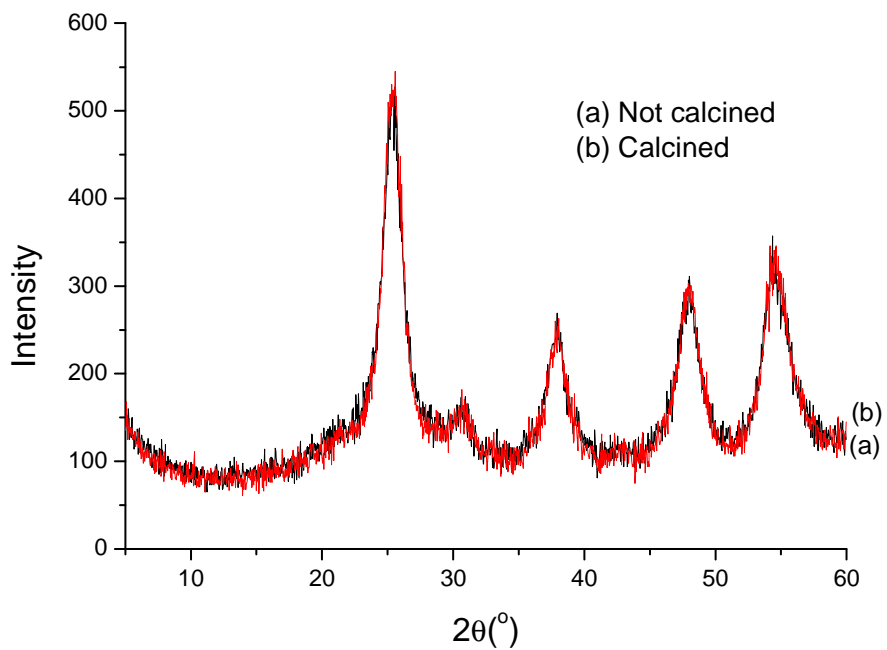


Fig 34: Wide-angle X-ray powder diffraction (XRD): (A) STi/SBA-15(1/1); (B) STi/KIL-2(1/1)

The average crystallite sizes were determined from the Scherrer's equation using the broadening of the (1 0 1) anatase peak reflection with the usual assumption of

spherical crystallites (Table 7). We did not calculate the crystallite size of anatase in the samples with lower titania loading (STi/SBA-15(1/2), STi/SBA-15(1/1) and STi/KIL-2(1/2)) because there the anatase (1 0 1) peak interferes with the broad silica peak, making the determination of the half-height peak width difficult. As expected, the anatase nanocrystallites are much bigger in case of MTi/SBA-15(1/1) and MTi/KIL-2(1/1) samples, confirming that the titania source (pre-crystallized colloidal solution or hydrolyzed Ti-isopropoxide solution) has an important effect on the structure of silica-titania composites.

Table 7: Structural parameters of titania/silica powders determined from XRD

Sample	Anatase crystallite size (nm)	d_{100} (Å)	Unit cell (nm)	Wall thickness (nm)
SBA-15	–	111	12.73	7.73
STi/SBA-15(1/2)	–	98	11.28	4.28
STi/SBA-15(1/1)	–	100	11.52	6.52
STi/SBA-15(2/1)	12	100	11.52	6.52
MTi/SBA-15(1/1)	23	–	–	–
KIL-2	–	–	–	–
STi/KIL-2(1/2)	–	–	–	–
STi/KIL-2(1/1)	5	–	–	–
STi/KIL-2(2/1)	7	–	–	–
MTi/KIL-2(1/1)	19	–	–	–
Ti-Cl(2.5)	8	–	–	–
Millennium PC500	5–10	–	–	–

The value of d_{100} is derived from XRD measurements. The unit cell dimension for hexagonal structure was calculated as: $2d_{100}/\sqrt{3}$

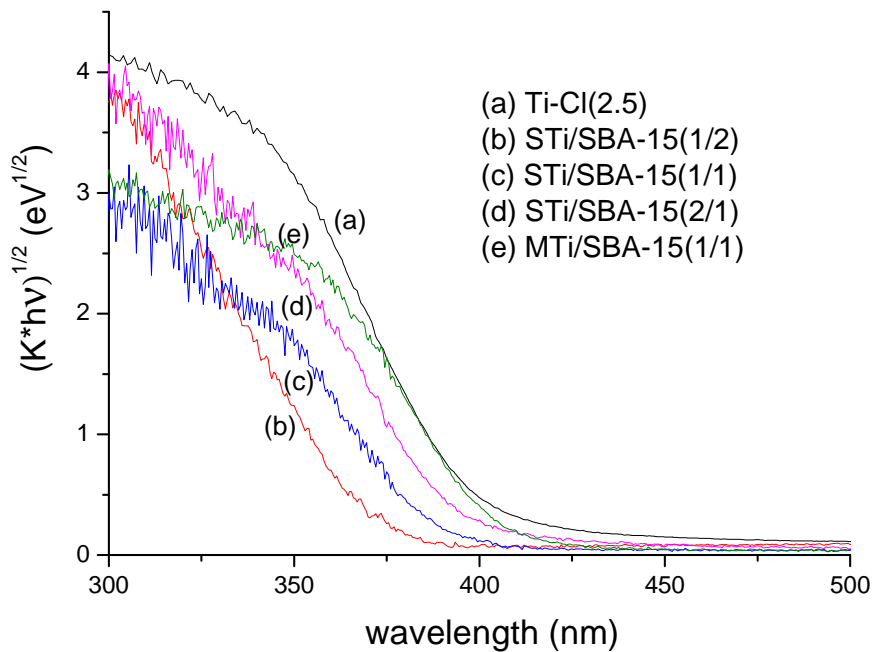
5.2.2. UV-vis diffuse reflectance

The UV-vis diffuse reflectance spectra of Ti-Cl(2.5), STi/SBA-15(x), STi/KIL-2(x), MTi/SBA-15(1/1) and MTi/KIL-2(1/1) are shown in Figure 35. The presence of broad absorption band at 330 nm confirms the existence of the nanocrystalline titania in the STi/SBA-15(x) and STi/KIL-2(x) powders. The spectra are blue shifted by incorporation of titania within mesoporous silica in both types of used supports (SBA-15 and KIL-2). However the spectra are red shifted by increasing the amount of titania from 1/2 to 2/1 in STi/SBA-15(x) and STi/KIL-2(x) powders.

The band-gap energies determined for all the synthesized powders are reported in Table 8. The band-gap energy of titania, where the growth of anatase crystallites is unperturbed, is 3.11 eV for Ti-Cl(2.5) powder. However, it changes when impregnated within silica support. By increasing the Ti/Si molar ratio from 1/2 to 2/1, the band-gap energy decreases from 3.39 to 3.14 eV in STi/SBA-15(x) and from 3.26 to 3.15 eV in STi/KIL-2(x) powders.

These results are correlated with the crystallite size of the anatase, being smaller at lower loadings due to their fit in the open pores of the silica support and formation of plugged mesopores, where anatase nanocrystallites with a limited size can be accommodated. By increasing the particle size, the band-gap energy decreases. The band-gap energies of MTi/SBA-15(1/1) and MTi/KIL-2(1/1) are 3.07 and 3.11 eV, respectively, resembling the values characteristic of titania.

A)



B)

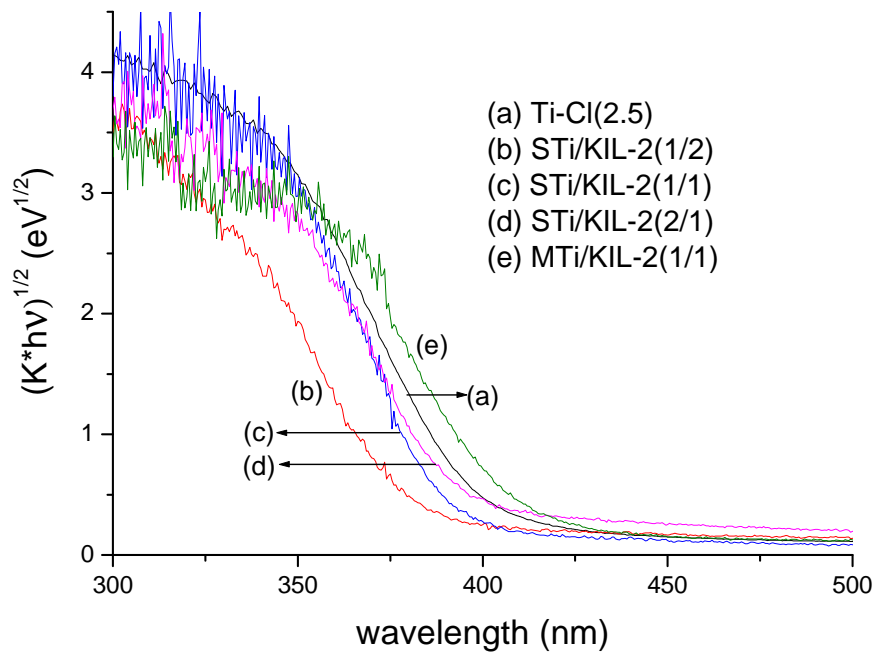
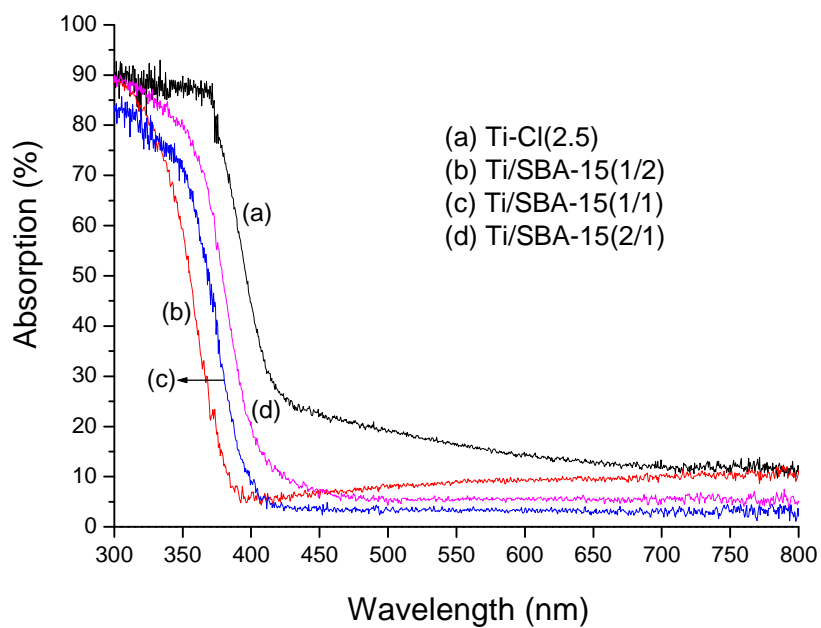


Fig 35: DR UV-vis spectra of (A) STi/SBA-15(x), MTi/SBA-15(1/1), Ti-Cl(2.5); (B) STi/KIL-2(x), MTi/KIL-2(x), Ti-Cl(2.5)

The UV-vis absorption spectra of the samples are shown in Figure 36. It can be observed that the absorption band-gap energy of STi/SBA-15(x) and STi/KIL-2(x) in comparison with Ti-Cl(2.5) powder is notably blue shifted indicating smaller anatase crystalline size for STi/SBA-15(x) and STi/KIL-2(x) powders. The results confirm that by incorporation of titania within silica mesoporous powders, the particles are not agglomerated together resulting in preparation of separated nanocrystalline titania particles (Yang et al. 2006). In STi/SBA-15(x) and STi/KIL-2(x) powders by decreasing the amount of titania (decreasing the Ti/Si molar ratio from 2/1 to 1/2) the absorption band-gap energies are blue shifted, in good agreement with the values of band-gap energy (Table 8).

A)



B)

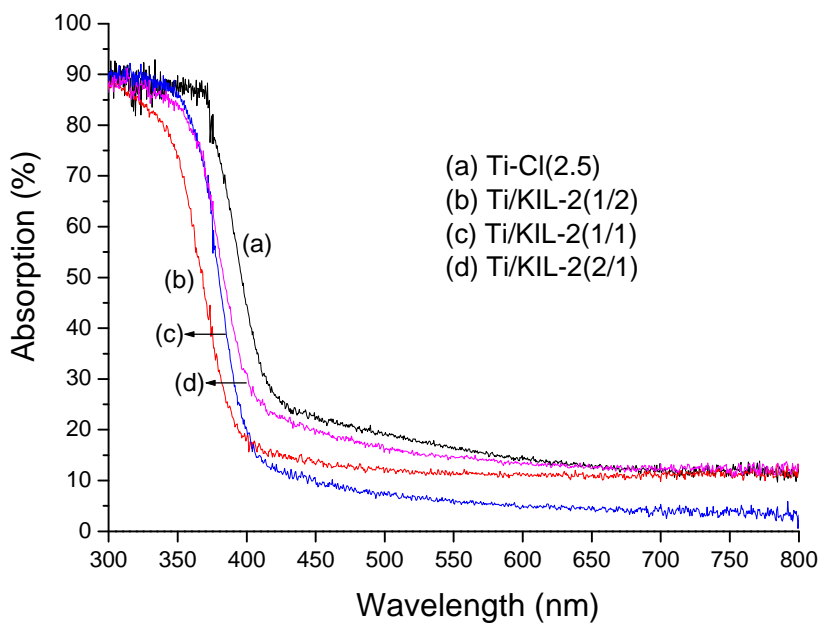


Fig 36: Absorption spectra of (A) Ti-Cl(2.5), STi/SBA-15(x); (B) Ti-Cl(2.5), STi/KIL-2(x)

Table 8: Band-gap energies of the powders determined with different amount of Ti

Sample	Ti/Si nominal molar ratio	Theoretical amount of TiO ₂ in the powder (wt.%)	Theoretical amount of Ti (wt.%)	Amount of Ti by elemental analysis (wt.%)	Band gap (eV)
SBA-15	–	–	–	–	–
STi/SBA-15(1/2)	1/2	40	24	8	3.39
STi/SBA-15(1/1)	1/1	58	35	29	3.20
STi/SBA-15(2/1)	2/1	74	44	38	3.14
MTi/SBA-15(1/1)	1/1	–	–	–	3.07
KIL-2	–	–	–	–	–
STi/KIL-2(1/2)	1/2	40	24	12	3.26
STi/KIL-2(1/1)	1/1	58	35	27	3.17
STi/KIL-2(2/1)	2/1	74	44	36	3.15
MTi/KIL-2(1/1)	1/1	–	–	–	3.04
Ti-Cl(2.5)	–	73	44	–	3.11
Millennium PC500	–	100	–	–	–

The concentration of Ti in different samples was measured by elemental analysis (Table 8). Results show that by increasing the Ti/Si nominal molar ratio, experimental amount of Ti were increased accordingly, however, the values are lower compared to the theoretical amount of Ti. The difference is obviously due to the some loss of Ti during the synthesis procedure.

5.2.3. Nitrogen-sorption measurement

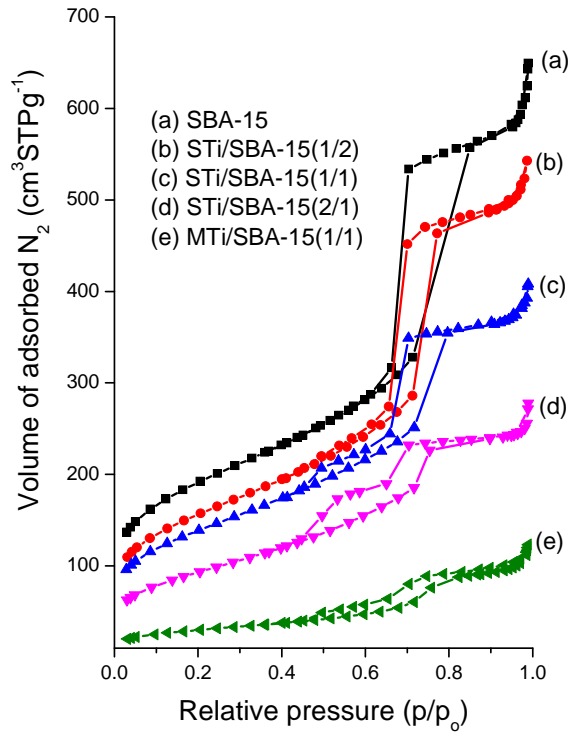
Nitrogen-sorption isotherms for SBA-15, MTi/SBA-15(1/1) and STi/SBA-15(x) powders are shown in Figure 37(A), whereas structural parameters determined on the basis of these isotherms are listed in Table 9. SBA-15 sample exhibited adsorption isotherm typical for SBA-15 silica, that is, with relatively narrow hysteresis loop of H1 type (Sing et al., 1985). It can clearly be observed that the presence of TiO₂ in SBA-15 leads to a marked change in the shape of the hysteresis loop. The hysteresis loop of all samples is closing down at lower relative pressure values in comparison to the original support (SBA-15), which indicates that the pores are partially narrowed with titania nanoparticles. The increase of the amount of the deposited TiO₂ nanoparticles on SBA-15 prepared by aqueous TiO₂ sol not only led to a decrease of

specific surface area (from 589 to 336 m² g⁻¹), total pore volume (from 0.903 to 0.378 cm³ g⁻¹), primary mesopore volume (from 0.682 to 0.303 cm³ g⁻¹), and pore diameter (from 11.2 to 8.6 nm) but also resulted in an appreciable widening and tailing of hysteresis loops and in a two-step desorption, thus evidencing the formation of PHTS-like material (Celer et al., 2006; Meynen et al., 2004; Meynen et al., 2007). N₂ sorption isotherms of PHTS are of type IV according to the IUPAC classification (Sing et al., 1985), showing a one-step capillary condensation, indicating the filling of the uniform mesopores and two-step desorption. The first step is similar with desorption in pure SBA-15 and is assigned to desorption of nitrogen from the open pores; the second desorption step can be attributed to the nanoparticles (plugs) within the mesopores (the narrowed mesopores) (Van der Voort et al., 2002; Kruh et al., 2003). The second step on the desorption branch indicates the existence of plugged mesopores. This two-step desorption is similar to that of the PHTS materials with amorphous microporous silica nanoparticles (plugs) in the mesopores (Kruh et al., 2003; Mazaj et al., 2009; Meynen et al., 2004). It can be concluded that the titania nanoparticles have been dispersed inside the channels of SBA-15 thereby narrowing parts of the mesopores. Therefore, desorption is postponed to lower relative pressures resulting in the second desorption step. Further increase of the titania amount results in a more pronounced growth of the titania nanoparticles causing a significant decrease of the open pores volume and in the change of the second desorption step. When titania loading is further increased the growth of the titania particles on the external surface is expected. The decrease of the interparticle (textural) porosity (given by the small hysteresis at P/P₀ = 0.95–1) suggests the growth of the TiO₂ nanoparticles on the outer surface, filling the voids between SBA-15 particles. The shape of isotherms of samples STi/SBA-15(1/1) and MTi/SBA-15(1/1) (Figure 37(A)) are different due to a different precursor. The primary mesopore volume and pore diameter of MTi/SBA-15(1/1) are significantly lower than for STi/SBA-15(1/1). The preparation method using Ti-isopropoxide as titania source also caused the destruction of ordered mesostructure, which is in agreement with the XRD pattern of this material.

Pore size distribution of the different mesoporous materials has been determined using the BJH model widely used for these types of sample (Lukens et al., 1999). Although this model often underestimates pore sizes (Tanev et al., 1993), it is

appropriate for comparative purposes. Figure 37(B) displays the pore size distribution determined from adsorption isotherms. It is clear that after impregnation two maxima appear representing the open mesopores located at the mesopore mouths and the narrowed pores in which the pore radius has shifted to lower values (Busuioc et al., 2006), while pore size distribution of pure SBA-15 shows only one maximum. As it can be observed, the maxima characteristic to open mesopores shift to lower pore sizes (Landau et al., 2005), are less intense and become broader with the growth of the titania plugs located inside the channels. At the same time, the maxima characteristic for narrowed pores shift to lower pore size values and are broader. Impregnating higher amounts of titania results in a lower amount of open pores present in the material. These results match with previous observations, where the pore size distribution shifted to lower pore diameters (Landau et al., 2005). The difference between two types of precursor is also evidenced from the pore size distribution of MTi/SBA-15(1/1) sample, where only one broad maximum appears.

A)



B)

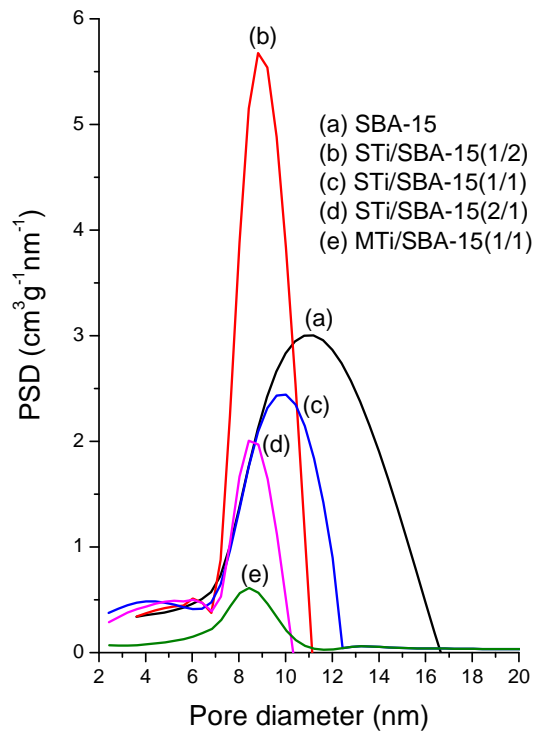


Fig 37: (A) Nitrogen-sorption isotherms; (B) pore size distribution of SBA-15, STi/SBA-15(x), MTi/SBA-15(1/1)

Table 9: Structural parameters of powders determined from N₂ sorption measurements

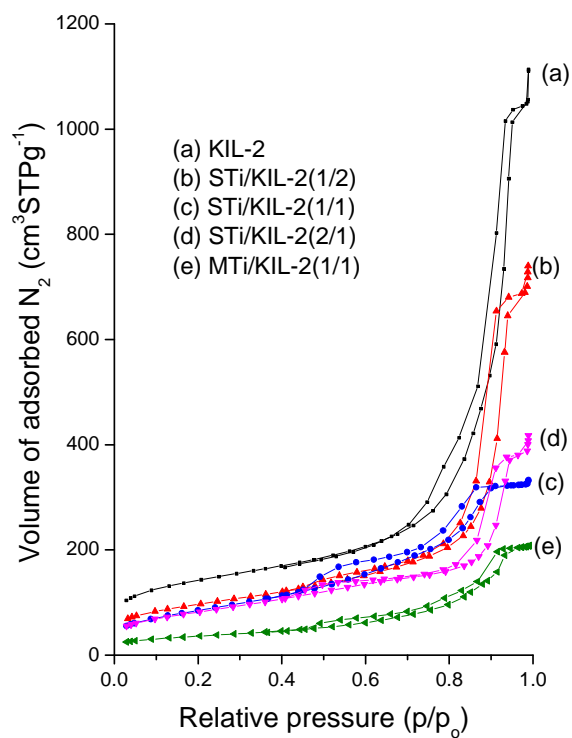
Sample	S _{BET} (m ² g ⁻¹)	V _t (cm ³ g ⁻¹)	V _{me} (cm ³ g ⁻¹)	S _{ex} (m ² g ⁻¹)	S _{me} (m ² g ⁻¹)	w _{BJH(1)} (nm)	w _{BJH(2)} (nm)
SBA-15	589	0.903	0.682	114	488	11.2	–
STi/SBA-15(1/2)	560	0.779	0.580	87	447	8.9	6.0
STi/SBA-15(1/1)	498	0.578	0.491	58	410	9.3	4.2
STi/SBA-15(2/1)	336	0.378	0.303	51	310	8.6	5.2
MTi/SBA-15(1/1)	107	0.154	0.097	37	90	8.4	–
KIL-2	504	1.561	1.337	122	324	31.6	13.7 18.2
STi/KIL-2(1/2)	345	1.016	0.728	157	278	27.9	5.5
STi/KIL-2(1/1)	309	0.499	0.488	8	322	14.2	5.5
STi/KIL-2(2/1)	296	0.577	0.501	52	287	27.4	3.8
MTi/KIL-2(1/1)	130	0.306	0.303	9	115	27.4	6.6 13.7
Ti-Cl(2.5)	80	0.045	–	–	–	–	–
Millennium PC500	300	–	–	–	–	–	–

S_{BET}: the BET surface area; V_t: total pore volume evaluated from adsorption isotherm at the relative pressure about 0.96; V_{me}: primary mesopore volume evaluated by the α_s-method; S_{ex}: external surface area evaluated by α_s-method; S_{me}: mesoporous surface area evaluated by α_s-method; w_{BJH}: mesopore diameters at the maximum (maxima) of the BJH pore size distribution.

Nitrogen adsorption isotherms for KIL-2, MTi/KIL-2(1/1) and STi/KIL-2(x) powders are shown in Figure 38(A), whereas structural parameters determined on the basis of these isotherms are listed in Table 9. KIL-2 sample exhibited an adsorption isotherm typical for KIL-2 silicas (Novak Tušar et al., 2010), that is, with relatively narrow hysteresis loop of type IV (Sing et al., 1985). It can be clearly observed that the introduction of titania into KIL-2 also leads to a marked change in the shape of the hysteresis loop. Again, the hysteresis loop of all samples is closing down at lower P/P₀ values in comparison to the original support, which indicates that the pores are partially narrowed with titania nanoparticles. Increase of the amount of the deposited titania nanoparticle on KIL-2 led to a decreased specific surface area (from 504 to 296 m² g⁻¹), total pore volume (from 1.561 to 0.499 cm³ g⁻¹), primary mesopore volume (from 1.337 to 0.488 cm³ g⁻¹), and pore diameter (from 31.6 to 14.2 nm). Beside these changes an appreciable widening and tailing of hysteresis loops and/or a two-step desorption were observed, thus evidencing the formation of materials with plugs in pores. The first step is similar with desorption in pure KIL-2 and is assigned to desorption of nitrogen from the open pores; the second desorption step can be

attributed to the nanoparticles (plugs) within the mesopores (the narrowed mesopores) (Van der Voort et al., 2002; Kruh et al., 2003). A second step on the desorption branch indicates the existence of plugged mesopores. Therefore, it can be concluded that the titania nanoparticles have been dispersed inside the pores of KIL-2 thereby narrowing parts of the mesopores. Further increase of the titania amount results in a significant decrease of the open pore volumes and in the change of the second desorption step. Higher titania loading caused the growth of titania particles on the external surface. This evidence is clearly seen in a relative pressure range from 0.95 to 1, where hysteresis loops due to textural porosity become smaller. The pore size distribution determined from adsorption isotherms of KIL-2 shows 3 distinguished maxima (Figure 38(B)). Pore size distributions of STi/KIL-2(x) samples show only 2 maxima, while pore size distribution of MTi/KIL-2(1/1) sample shows 3 maxima. As it can be observed, the maxima characteristic to open mesopores and to narrowed pores shift to lower pore sizes, are less intense and become broader with the growth of the titania plugs located inside the channels.

A)



B)

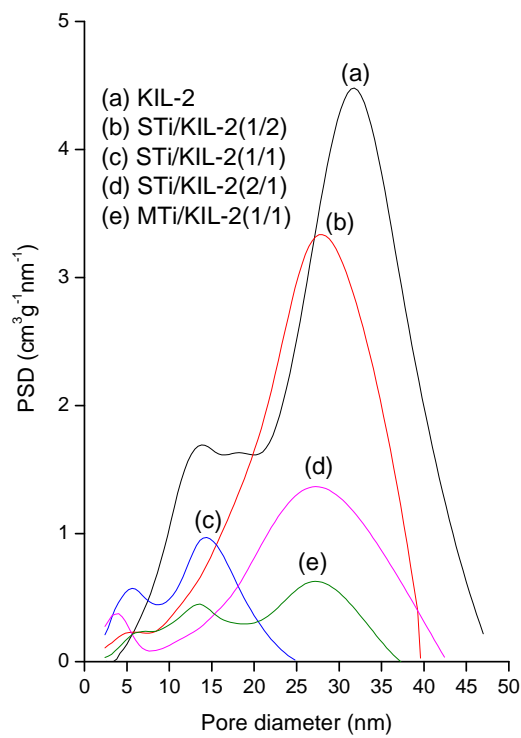
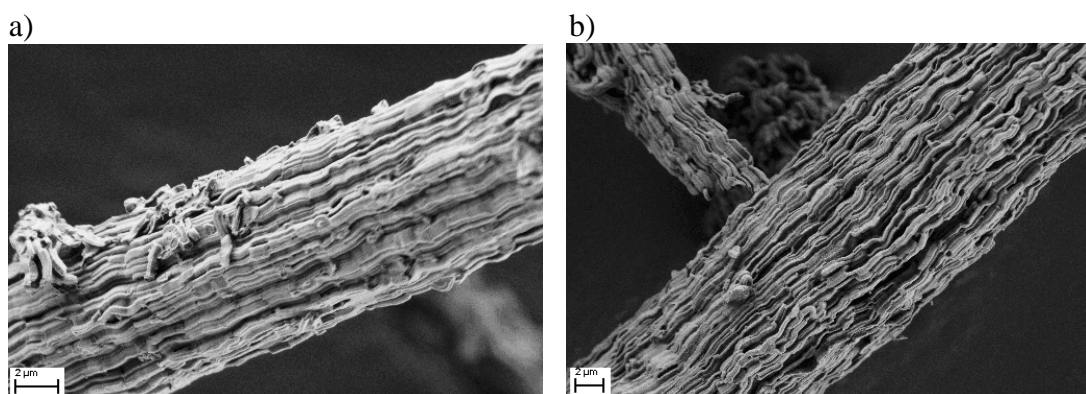


Fig 38: (A) Nitrogen-sorption isotherms; (B) pore size distribution of KIL-2, STi/KIL-2(x), MTi/KIL-2(1/1)

5.2.4. Scanning electron microscopy

The SEM micrographs of all the various samples are shown in Figures 39 and 40. The SEM image of pure SBA-15 presented in Figure 39(a) shows curved rod-like particles of relatively uniform size with a quite smooth surface (Mazaj et al., 2009). In the STi/SBA-15(1/2) and STi/SBA-15(1/1) powders, as evidenced from Figures 39(b) and (c), these powders show a homogenous distribution of the titania on the internal surface of SBA-15 powder and the morphology of samples does not change compared to pure SBA-15. However, at higher titania loading in the STi/SBA-15(2/1) powder, the external surface of SBA-15 is filled significantly by titania (Figure 39(d)), which is in accordance with the nitrogen-sorption results. In the MTi/SBA-15(1/1) sample (Figure 39(e)), impregnation of hydrolyzed Ti-isopropoxide changed the morphology of SBA-15 drastically, again well in accordance with the results discussed above.

As it is shown in Figure 40(a), the SEM micrograph of KIL-2 powder is characterized by the porous and rough surface. In fact these powders suggest the main type of porosity, which is so-called interparticle or textural porosity (Novak Tušar et al., 2010). The roughness in the surface of KIL-2 increases by adding titania. Thus by increasing the Ti/Si molar ratio from 1/2 to 2/1 in the STi/KIL-2(x) powders, the roughness increases considerably (Figures 40(b)–(d)). In the MTi-KIL-2(1/1) sample, as it is represented in Figure 40(e), the roughness of KIL-2 seems to decrease resulting in a less textured surface.



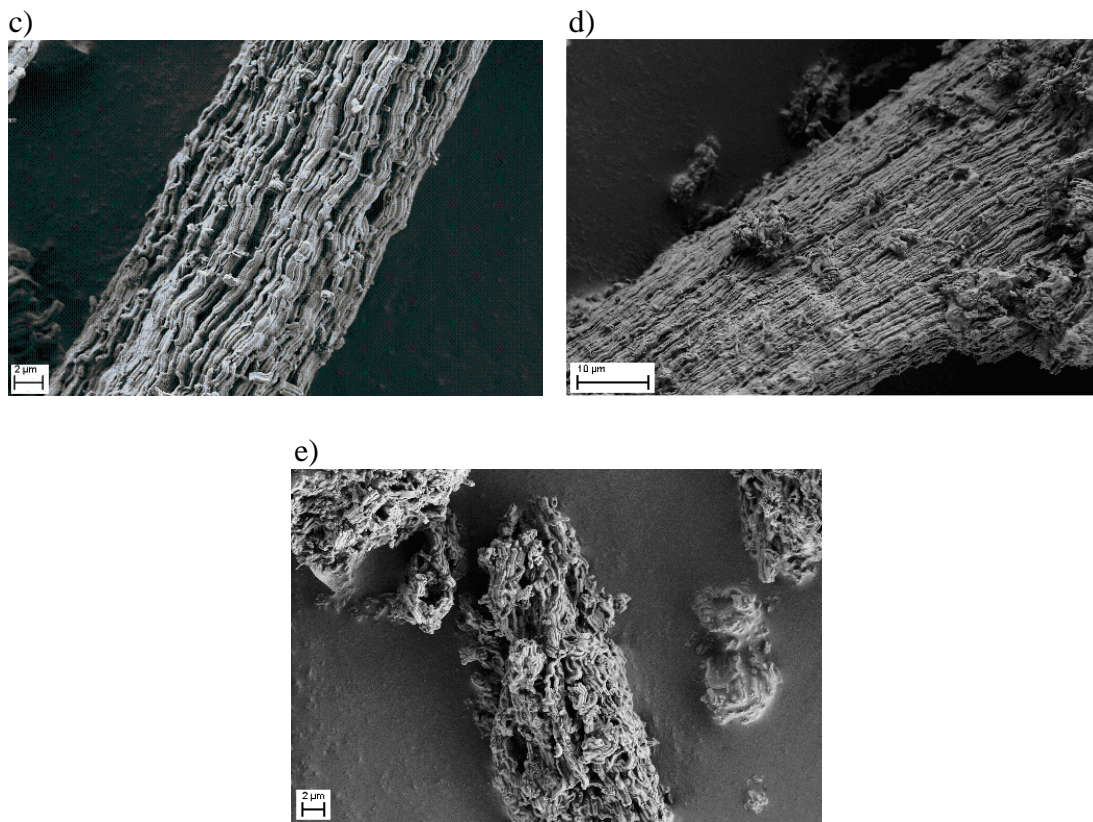
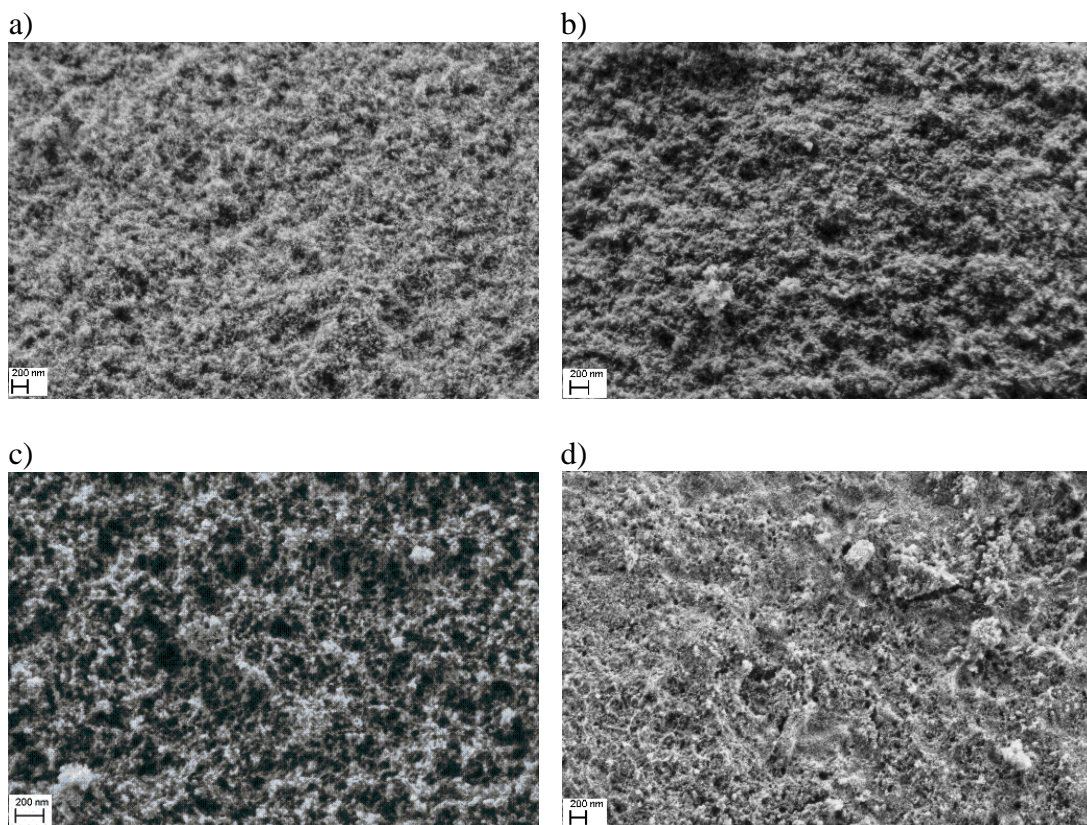


Fig 39: SEM images of (a) SBA-15; (b) STi/SBA-15(1/2); (c) STi/SBA-15(1/1); (d) STi/SBA-15(2/1); (e) MTi/SBA-15(1/1)



e)

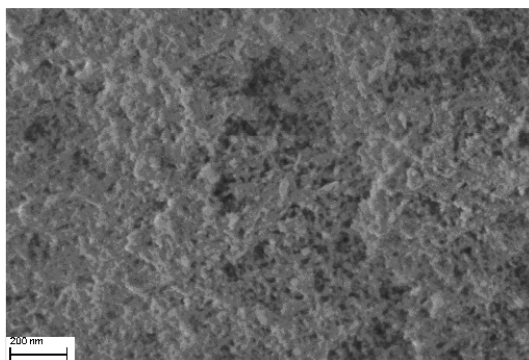


Fig 40: SEM images of (a) KIL-2; (b) STi/KIL-2(1/2); (c) STi/KIL-2(1/1); (d) STi/KIL-2(2/1); (e) MTi/KIL-2(1/1)

It is useful to mention that we did SEM measurements for the STi/SBA-15(1/1) and STi/KIL-2(1/1) samples after calcination at 300 °C for 6 h as well (Figure 41). There was no significant difference noted between non-calcined and calcined samples as it was already shown with the wide-angle XRD measurements.

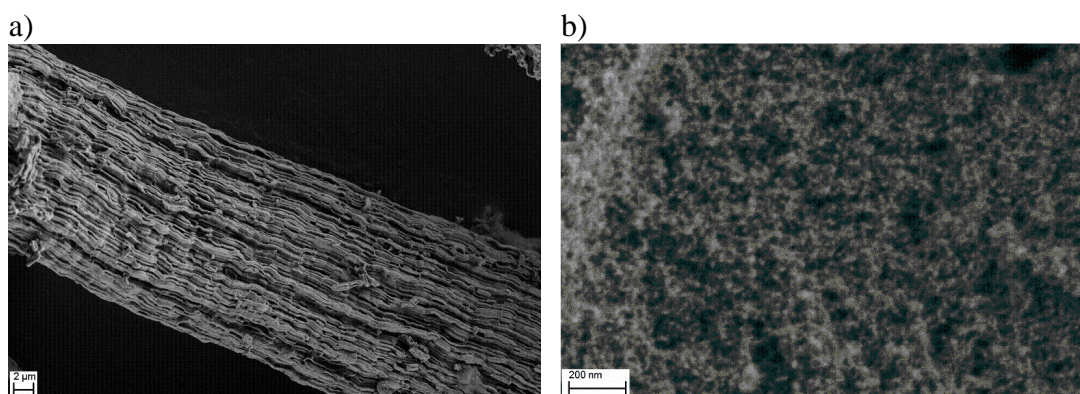


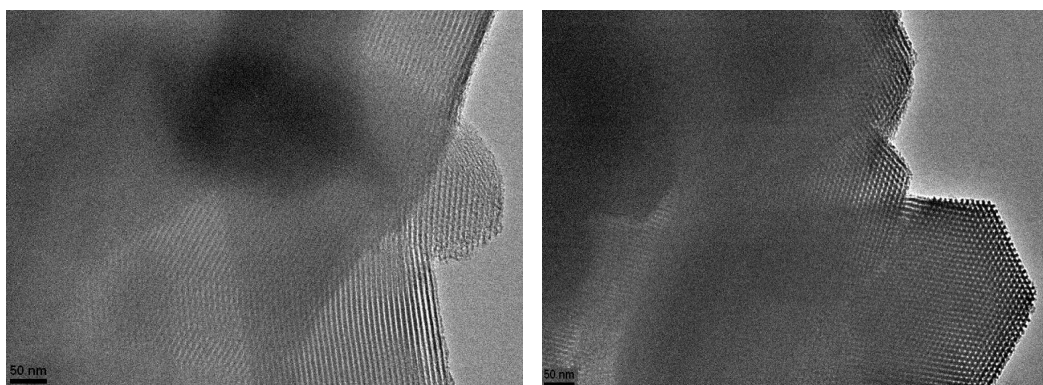
Fig 41: SEM images of (a) STi/SBA-15(1/1); (b) STi/KIL-2(1/1) after calcination at 300 °C

5.2.5. High resolution transmittance electron microscopy (HR-TEM)

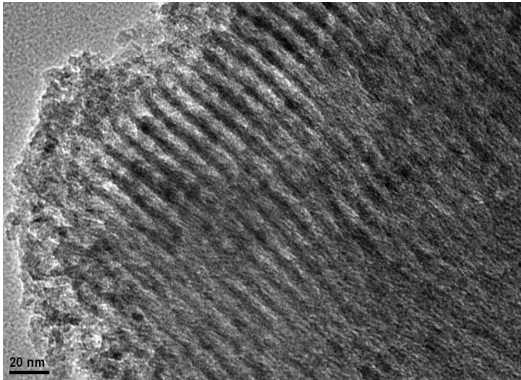
Figure 42 illustrates the HR-TEM micrographs of SBA-15 and STi/SBA-15(x). Figure 42(a) evidences the presence of the parallel nanotubular channels of SBA-15 mesoporous silica. The introduction of titanium does not alter the regular order array of SBA-15 and the ordered mesostructure of SBA-15 is kept quite unaffected by incorporation of the titania into the channels (Figures 42(b)-(d)). Indeed, the HR-TEM micrographs of STi/SBA-15(x) show the mesoporous structure of the SBA-15 with the black spots corresponding to the TiO₂ nanoparticles inside the channels. This is in good agreement with low-angle XRD measurement of SBA-15 and STi/SBA-15(x) (section 5.2.1.1.). Left images in Figure 42(b)-(d) show STi/SBA-15(x) matrix along (1 1 0) channel directions. The images at higher magnification

reveal the presence of anatase nanoparticles with the size between 5 and 10 nm, slightly lower than estimated by XRD measurements (Table 7). Figure 42(d) at the highest magnification shows the lattice image of anatase (PDF 21–1272) confirmed with the d spacing of 3.52 Å corresponding to (1 0 1) plane and tetragonal TiO₂ type cell with space group I4₁/amd. The fact that anatase nanoparticles are densely distributed throughout the silica walls with random orientation suggests that they are deposited on the surface of mesoporous silica matrix rather than incorporated within the silica walls. Wittmann et al. (2005) confirmed that the crystalline titania particles appeared on the silica structure when the Ti/Si molar ratio was higher than 0.05. Furthermore, these results are in agreement with nitrogen–sorption measurements (section 5.2.3.). As it is mentioned there, the incorporation of titania into SBA–15 led to more narrow pores and decreased surface area of the silicate materials. An increase of Ti/Si molar ratio resulted in a decrease of the surface area of SBA–15 (Table 9). We observed that titania nanoparticles were dispersed inside the channels of SBA–15 when Ti/Si molar ratio was 1/2. Further increase of titania content resulted in a more pronounced growth of titania nanoparticles causing a significant decrease of the open pores. For the Ti/Si molar ratio 2/1, nanocrystalline titania particles grew also on the external surface of SBA–15.

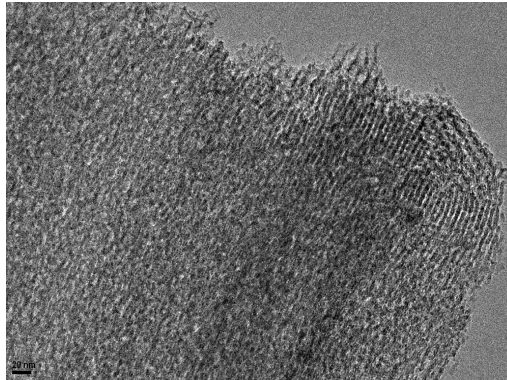
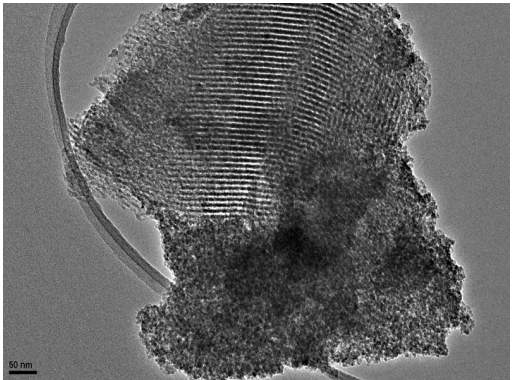
a)



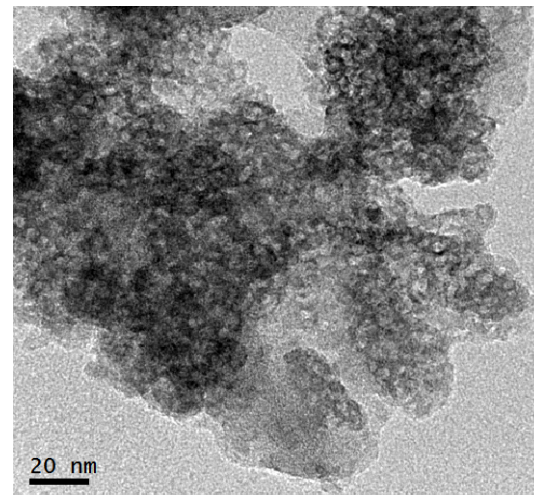
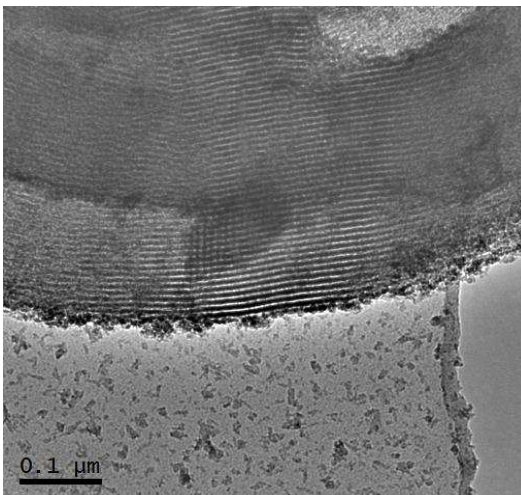
b)



c)



d)



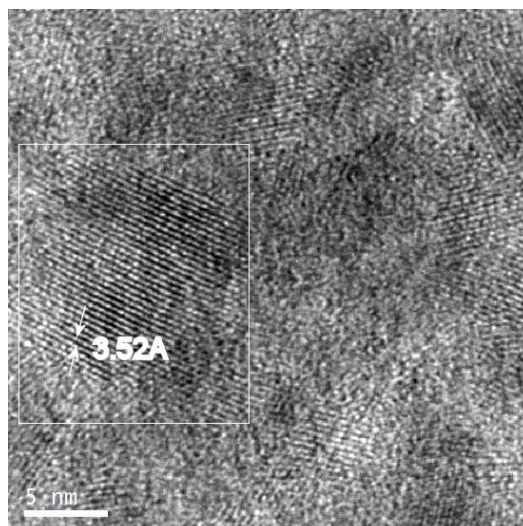
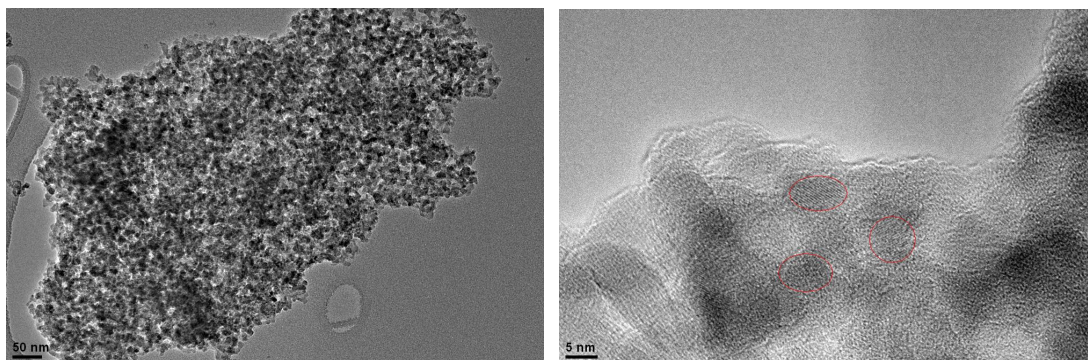


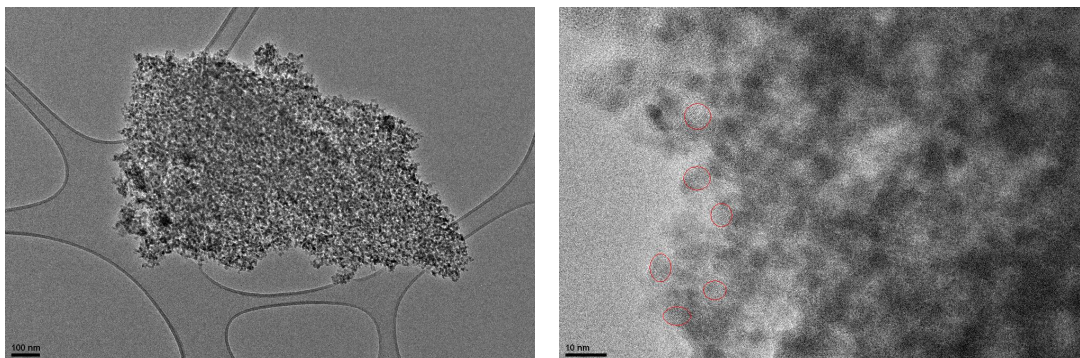
Fig 42: HR-TEM micrographs of (a) SBA-15; (b) STi/SBA-15(1/2); (c) STi/SBA-15(1/1); (d) STi/SBA-15(2/1) at different magnifications

Figure 43 demonstrates HR-TEM micrographs of mesoporous silica STi/KIL-2(x) powders with textural (interparticle) porosity. The image at higher magnification reveals the presence of anatase nanoparticles with the estimated size of 5 nm, confirmed also by XRD measurements (Table 7). Anatase nanoparticles seem to be deposited on the silica nanoparticles causing only partial blocking of mesopores. This result is also in good agreement with nitrogen-sorption measurements (section 5.2.3.). It was concluded that the titania nanoparticles were dispersed inside the pores of KIL-2. this causes narrowing of the pores and decreasing of the surface area of KIL-2. For the Ti/Si molar ratio of 2/1, the nanocrystalline titania particles grew also on the external surface of KIL-2 silica similar to our observation with SBA-15 silica.

a)



b)



c)

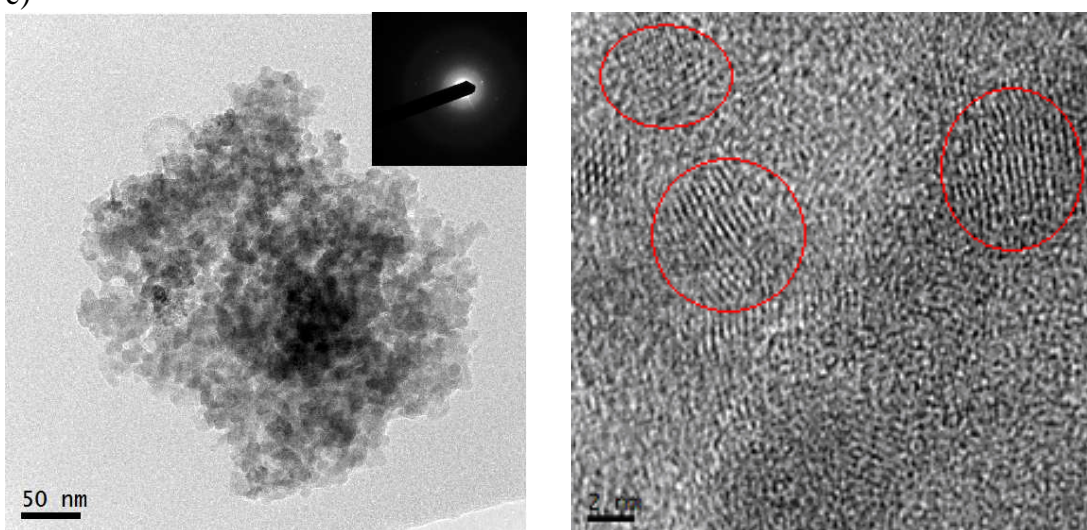
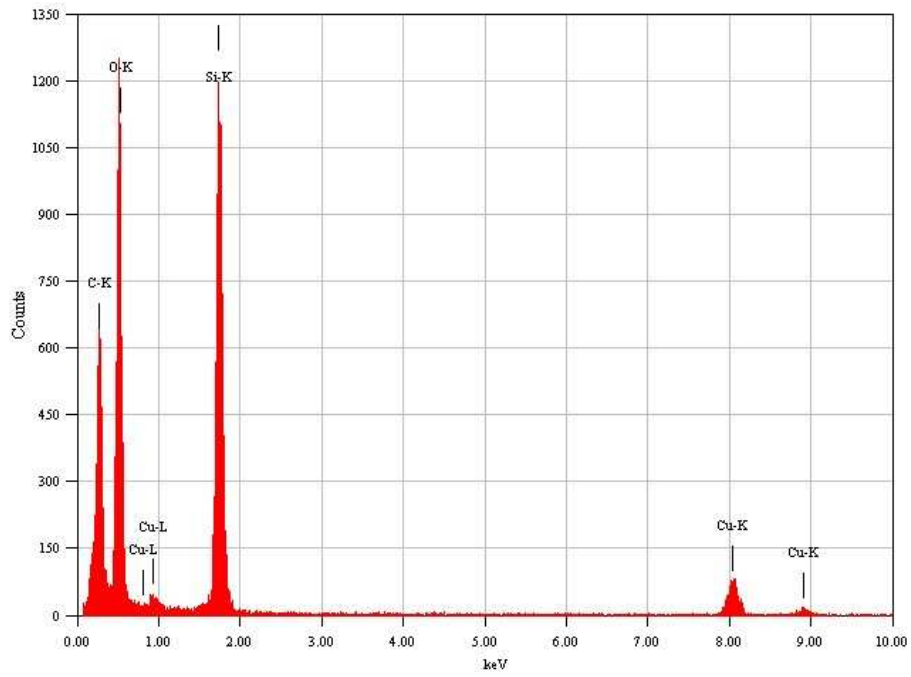


Fig 43: HR-TEM micrographs of (a) STi/KIL-2(1/2); (b) STi/KIL-2(1/1); (c) STi/KIL-2(2/1) at different magnifications and inset ED pattern of STi/KIL-2(2/1)

The local EDX analysis results of Ti/SBA-15(1/1) and Ti/KIL-2(1/1) are shown in Figures 44 and 45, respectively. As it is seen in Figures 44(A) and 45(A) there is no titania evident in these two specific points which could be associated to an empty part of the silica pore (channel), while in Figures 44(B) and 45(B) the presence of titania is obvious. In fact, the local EDX results reveal that the titania nanoparticles are not homogeneously distributed within the mesoporous pores (channels).

A)



B)

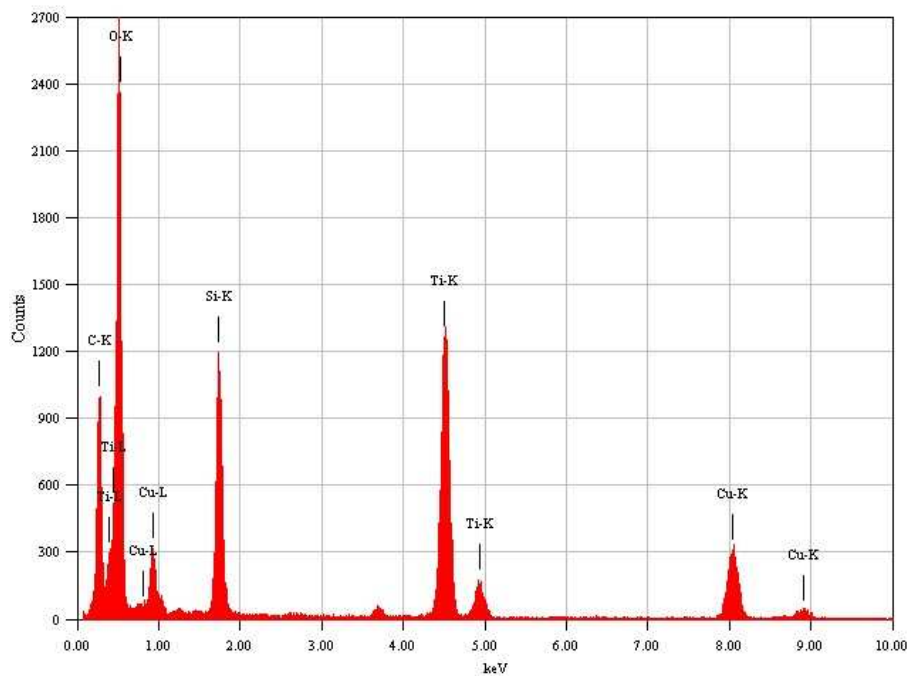
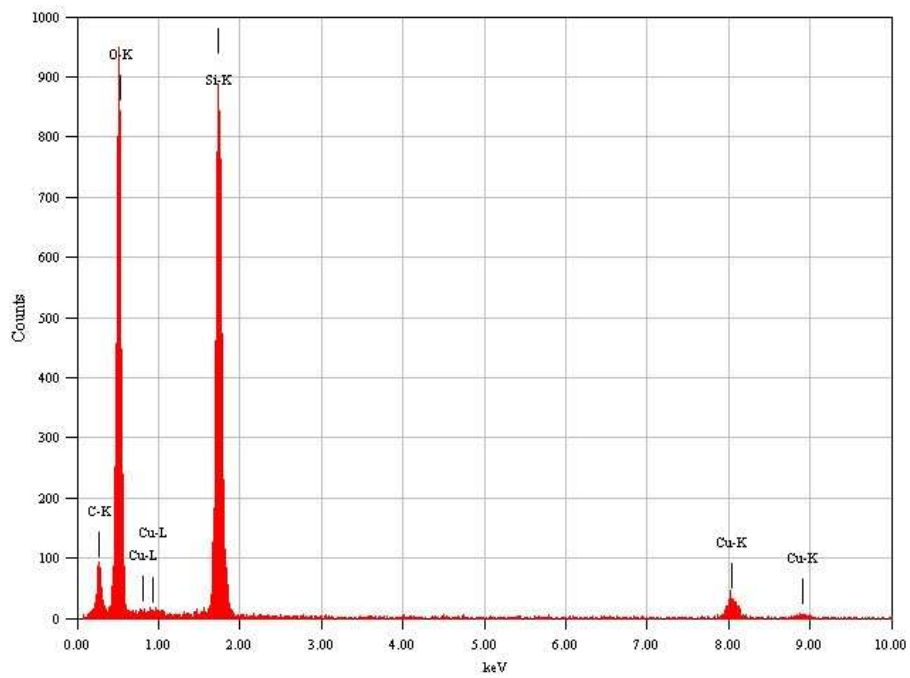


Fig 44: EDX analysis of STi/SBA-15(1/1) (A) at point without presence of Ti; (B) at point with presence of Ti

A)



B)

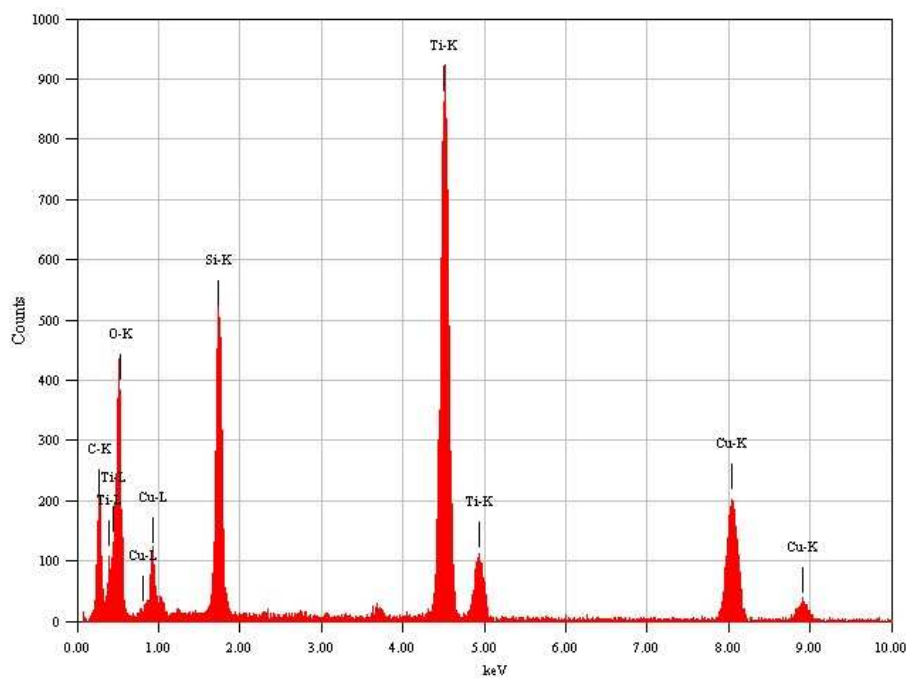


Fig 45: EDX analysis of STi/KIL-2(1/1) (A) at point without presence of Ti; (B) at point with presence of Ti

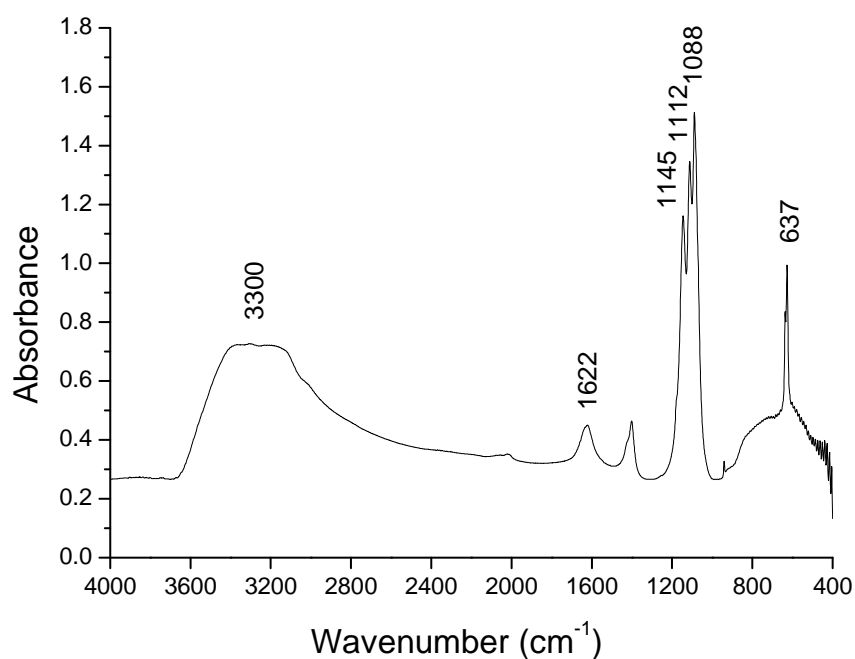
5.2.6. Fourier transform infrared spectroscopy (FT-IR)

Figure 46 illustrates FT-IR spectra of all powders. Figure 46(A) shows the FT-IR spectrum of the Ti-Cl(0.5) powder prepared from nanocrystalline aqueous titania sol. The broad band centred at around 3300 cm^{-1} is assigned to the O-H stretching vibration of Ti-OH groups and H₂O molecules (Kanna et al. 2008). The band at 1622 cm^{-1} belongs to O-H bending vibration of surface adsorbed water (Nag et al. 2007). All the sharp bands positioned at 1145 cm^{-1} , 1112 cm^{-1} , 1088 cm^{-1} and 637 cm^{-1} relate to perchlorate (Janik et al. 1969) and its interaction with titania (TiO₂-perchlorate) (McQuillan et al. 2001), which is in agreement with XRD results (section 5.1.1.) confirming the presence of TiO(ClO₄)₂·6H₂O (Tasbihi et al., 2009). Namely, perchloric acid was used as a peptizing mediator in the synthesis of titania sol (section 4.2.1.). The broad band below 800 cm^{-1} is assigned to the stretching mode of Ti-O-Ti (Velasco et al., 1999).

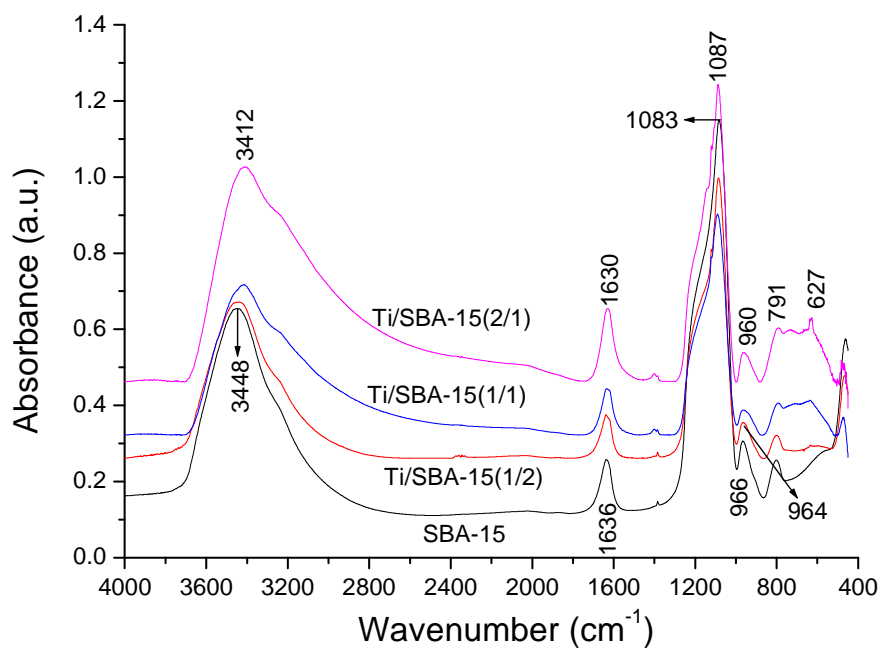
FT-IR spectra of SBA-15, STi/SBA-15(x) are shown in Figure 46(B) while spectra of KIL-2, STi/KIL-2(x) in Figure 46(C). Spectra of all these samples look similar without any significant differences, however, some features can be figured out. In the pure silica samples, the broad band centered at 3448 cm^{-1} and 3449 cm^{-1} is assigned to O-H stretching vibration of water molecules and Si-OH groups of SBA-15 and KIL-2, respectively. After loading titania, these peaks shift gradually to lower frequencies (3412 cm^{-1} for STi/SBA-15(2/1) and 3415 cm^{-1} for STi/KIL-2(2/1)) due to interaction of silanols with titania. The O-H stretching vibration of Ti-OH groups should also appear at lower frequencies (Kanna et al., 2008; Ding et al., 2005). The bands around 1090 cm^{-1} and 800 cm^{-1} are attributed to asymmetric and symmetric stretching vibration of the Si-O-Si framework, respectively (Ding et al., 2005). On the Si-O-Si stretching vibration at around 1090 cm^{-1} in the samples with titania loading, the peaks of perchlorate ions are superimposed. This indicates that perchlorates were not completely removed by washing in the preparation procedure of composite materials. Spectra of SBA-15 and KIL-2 show bands at 966 cm^{-1} and 970 cm^{-1} , respectively, which are attributed to Si-O stretching vibration of Si-OH groups (silanol groups in the mesoporous materials) (Perathoner et al., 2006). Similarly to the shift of O-H stretching vibration describe above, also Si-OH vibration is gradually shifted to lower frequencies with increasing Ti/Si molar ratio from, for example from 964 cm^{-1} to 960 cm^{-1} and from 967 cm^{-1} to 959 cm^{-1} in

STi/SBA-15(x) and STi/KIL-2(x), respectively. These peaks might also correspond to titanol (Ti-OH) and/or the interaction of titania with silanol groups forming Si-O-Ti groups (Perathoner et al., 2006; Boccuti et al., 1989). In the case of samples with the higher Ti/Si molar ratio (1/1 and 2/1), a broad Ti-O stretching vibration appeared while for lower Ti/Si molar ratio it was not observed. It could be due to the fact that the growth of titania on external silica surface was promoted after the titania species had been anchored inside the pores of silicate materials (see also discussion above).

A)



B)



C)

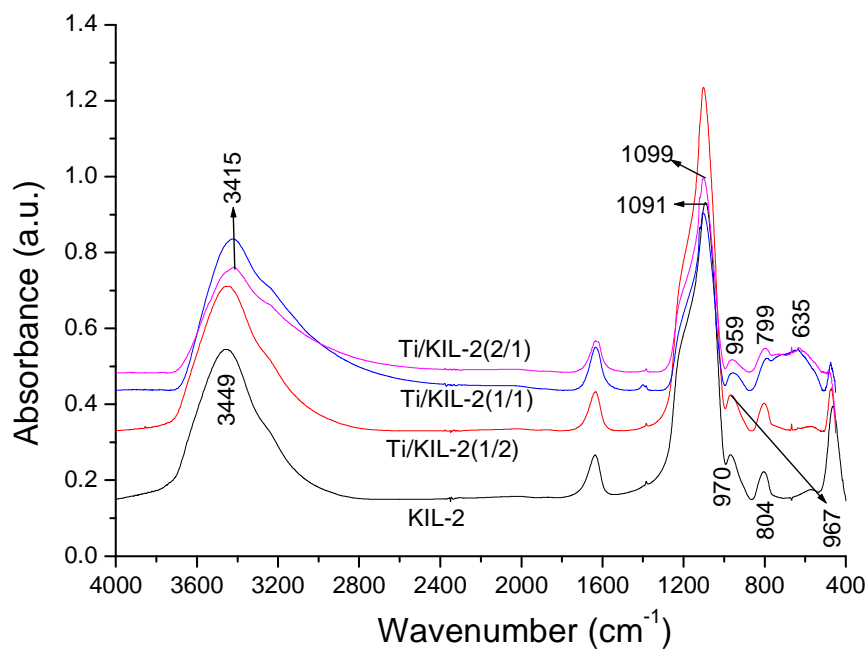


Fig 46: FT-IR spectra of (A) Ti-Cl(2.5); (B) SBA-15, STi/SBA-15(x); (C) KIL-2, STi/KIL-2(x)

5.2.7. The photocatalytic activity towards gaseous isopropanol degradation

Figures 47 and 48 illustrate the adsorption capacity and the formation of acetone during the photocatalytic degradation of isopropanol in the presence of different samples. Additionally, the profiles of acetone and isopropanol in the absence of a photocatalyst (blank) were included in the graphs. In all tests at the beginning of the experiment the UV lamp was switched off to achieve an adsorption–desorption equilibrium. The adsorption–desorption equilibrium times were not the same for various samples. Some adsorption took place also in the absence of a photocatalyst sample (onto the surfaces of the reactor system). In Figures 47(A) and 48(A) the time zero represents the point when the UV lamp was switched on. Before that, there was no detectable degradation of isopropanol in the dark but nevertheless the isopropanol concentration decreased, mostly due to the adsorption of isopropanol on the catalyst powders. In the case of SBA–15, MTi/SBA–15(1/1) and STi/SBA–15(x) (Figure 47(A)) the adsorption capacity of SBA–15 was the highest, which corresponds to the highest surface area of SBA–15 powders. By loading with titania, the adsorption capacity of the samples decreased, roughly in accordance with the decreasing specific surface area (Table 9). For example, the surface area decreased from 560 to 336 m² g⁻¹ for STi/SBA–15(1/2) and STi/SBA–15(2/1), respectively. The adsorption capacity of Ti–Cl(2.5) is very low which is not surprising due to its relatively low surface area (80 m² g⁻¹). The photocatalytic activity of the powders was assessed according to the value of the rate constant (k_1) representing the oxidation of isopropanol into acetone. The analysis of data was based on the following two–step oxidation mechanism:



where k_1 and k_2 are the corresponding rate constants. As regards the order of these two steps, the first step is usually considered a zero–order reaction (Munuera et al., 1971; Bickley et al., 1973) while the second step can be assumed to be a first–order reaction. These assumptions lead to the following equation for the concentration of acetone as a function of time ($C_{acet}(t)$)

$$C_{acet}(t)(zero) = \frac{k_1}{k_2} \left(1 - e^{-k_2 t} \right) \quad (36)$$

According to this simplified model, at the time $t(\text{peak})$ all isopropanol has been consumed and the acetone curve exhibits a peak (maximum concentration). However, it has been shown that the interpretation of the appearance of peak might be much more complex than indicated by Eqs. (35) and (36). Besides being created due to the exhaustion of the supply of isopropanol vapour to the irradiated titania surface, one needs to take into account the re-adsorption of the acetone vapour upon the titania. In fact, the process of acetone re-adsorption might even be a decisive step, especially because the degradation rate of acetone might be relatively slow. Larson et al. (1995) studied the photocatalytic oxidation of isopropanol on the thin TiO_2 P-25 photocatalyst film in the annular reactor. The photocatalytic oxidation of isopropanol to form acetone is rapid but subsequently oxidation of acetone to CO_2 and H_2O is slower. The rate of the photocatalytic oxidation to form acetone is essentially independent of O_2 concentration above 1 % O_2 , apparently because lattice oxygen is involved in the reaction. The results also showed that during steady-state reaction, the degree of partial oxidation to acetone is expected to depend on the concentration of water vapor. Thermal oxidation of isopropanol first formed acetone which oxidized faster than isopropanol, so that isopropanol oxidation to CO_2 and H_2O is limited by the initial oxidation to acetone. In any case, the initial slope of the curve is independent of these further complications, so the data obtained from this initial slope are usually quite reliable. In our case, we use these data mainly for rough comparison of different catalysts without attempting to find exact absolute values for rate constants or exact underlying mechanisms. The trends in k_I for different catalysts prepared in this study are seen from Table 10.

As expected, SBA-15 did not show any photocatalytic activity. However, the photocatalytic activity of STi/SBA-15(x) increased by increasing the Ti/Si ratio from 1/2 to 1/1 (STi/SBA-15(1/2) and STi/SBA-15(1/1)), but in STi/SBA-15(2/1) it decreased significantly. As shown in XRD results (section 5.2.1.), the crystallinity and the number of anatase nanoparticles increased when the Ti/Si molar ratio was raised from 1/2 to 1/1 resulting in the high photocatalytic activity. However, by increasing the Ti/Si molar ratio further to 2/1 in the STi/SBA-15(2/1) powder, the

partial blocking of mesopores occurred and the external surface of SBA-15 began to fill with the high amount of titania, as it is demonstrated above from nitrogen-sorption measurements (section 5.2.3.) and SEM results (section 5.2.4.). Therefore, the photocatalytic activity was the highest in the presence of the STi/SBA-15(1/1) powders. In MTi/SBA-15(1/1) powder, having the same nominal Ti/Si molar ratio as STi/SBA-15(1/1), the adsorption capacity and photocatalytic activity were very low. It is reported in Table 9 that the MTi/SBA-15(1/1) sample has the lowest surface area compared to other supported samples, whereas it has the most developed anatase crystalline structure (Figure 33(A)). As shown by XRD and SEM results, the structure of SBA-15 support was completely destroyed by using Ti-isopropoxide as a titania precursor. It should be pointed out that the high crystallinity in MTi/SBA-15(1/1) sample is also due to the calcination treatment at 300 °C for 6 h during the synthesis procedure.

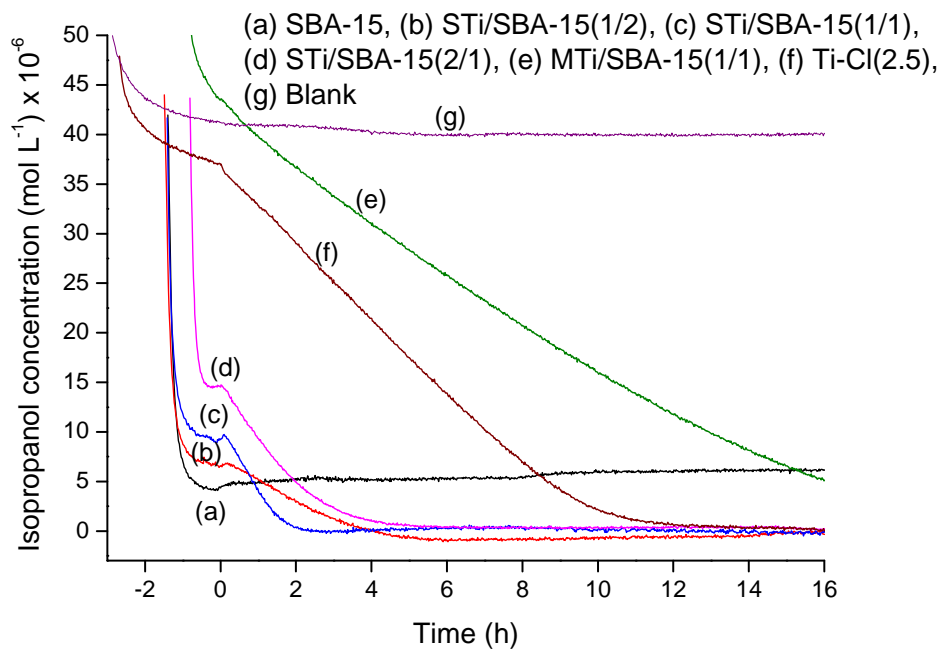
In the case of KIL-2, MTi/KIL-2(1/1) and STi/KIL-2(x) (Figure 48) there are some important differences in comparison with samples using SBA-15 support. First, the adsorption capacity of KIL-2 was lower than SBA-15 due to its lower surface area in comparison to SBA-15 materials. The adsorption capacity of the STi/KIL-2(x) samples decreased as the Ti/Si ratio increased from 1/2 to 1/1 (samples STi/KIL-2(1/2) and STi/KIL-2(1/1)). However, it slightly increased for STi/KIL-2(2/1) even though its surface area was slightly lower than STi/KIL-2(1/1). This can be due to the interparticle or textural properties of KIL-2 materials. The acetone formation rate (Figure 48(B)) increased significantly by increasing the amount of titania from STi/KIL-2(1/2) to STi/KIL-2(1/1), while at the highest titania loading, STi/KIL-2(2/1), it remained approximately the same. However, in the presence of the MTi/KIL-2(1/1) sample, the adsorption capacity was very low due to the low surface area but interestingly, the photocatalytic activity of this sample was comparable to the activity of STi/KIL-2(1/1) powder. Here, the structure of the support was not destroyed upon using the Ti-isopropoxide as a precursor (Figure 40(e)), also the hysteresis loop in the nitrogen-sorption measurements is well evident (Figure 38(A)).

Note that the powders that were prepared using SBA-15 as a support had a higher adsorption capacity. This can directly be explained by their higher surface area.

Regarding the photocatalytic activity (acetone formation), when the Ti/Si molar ratio was 1/2 and 1/1, the samples which were prepared using SBA-15 showed higher photocatalytic activity. This means that the photocatalytic activity of STi/SBA-15(1/2) and STi/SBA-15(1/1) is higher than the photocatalytic activity of STi/KIL-2(1/2) and STi/KIL-2(1/1). But when the Ti/Si molar ratio was 2/1, the photocatalytic activity of the STi/KIL-2(2/1) sample was comparable to the activity of STi/SBA-15(2/1) (similar acetone formation rate constant). The acetone formation rate constants are summarized for all studied samples in Table 10. As it is reported, the acetone formation rate was the highest in the presence of the STi-SBA-15(1/1) powder, indicating the importance of maintaining high mesostructural order of the silica support upon titania loading and its influence of keeping the titania nanoparticles relatively separated and accessible.

We obtained the above results in our specific photocatalytic test condition, however, Ohko et al. (1998) studied the effect of the initial concentration of isopropanol and UV intensity on the degradation of gaseous isopropanol using TiO₂ film photocatalyst in a batch reactor. The incident UV intensity and initial isopropanol concentration were varied from 35 to 60 mW cm⁻² and from 0.1 to 100 ppmv, respectively. They have mapped out a vast range of experimental condition, covering 6 order of magnitude of reactant concentration and 8 orders of magnitude of light intensity, in the terms of mass transport vs, light intensity control.

A)



B)

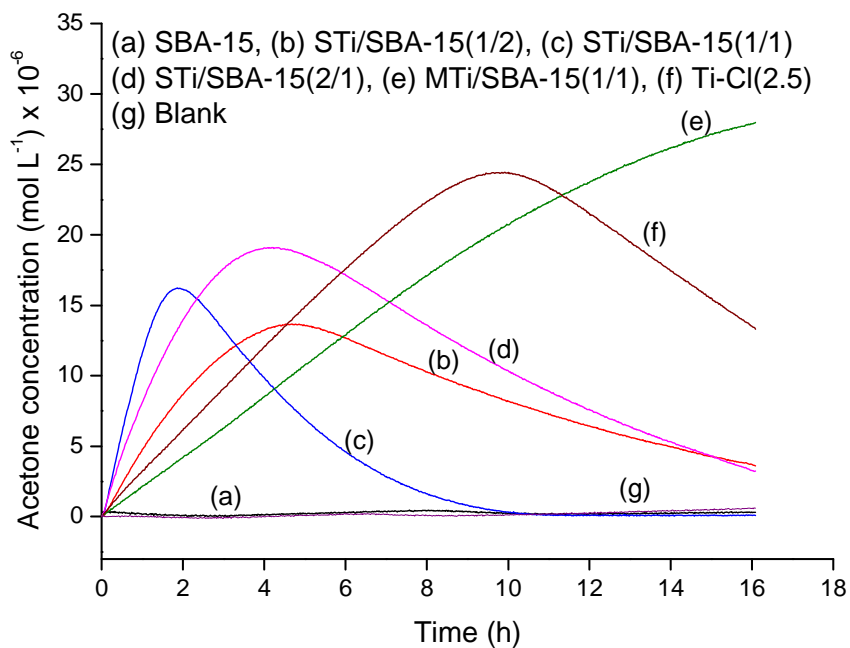
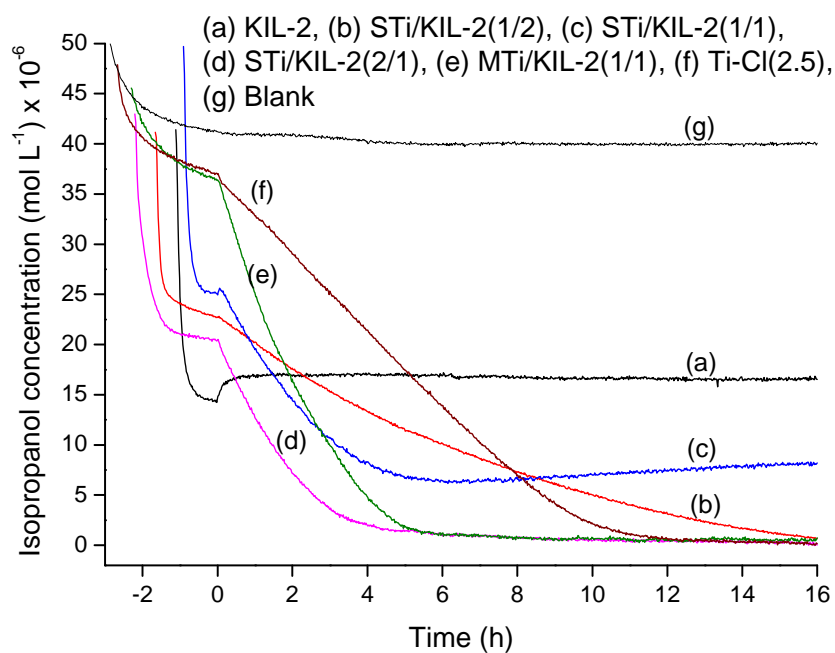


Fig 47: (A) Dark adsorption of isopropanol (negative illumination times) and its photocatalytic disappearance; (B) acetone formation curves in presence of SBA-15, STi/SBA-15(x), MTi/SBA-15(1/1), Ti-Cl(2.5), blank

A)



B)

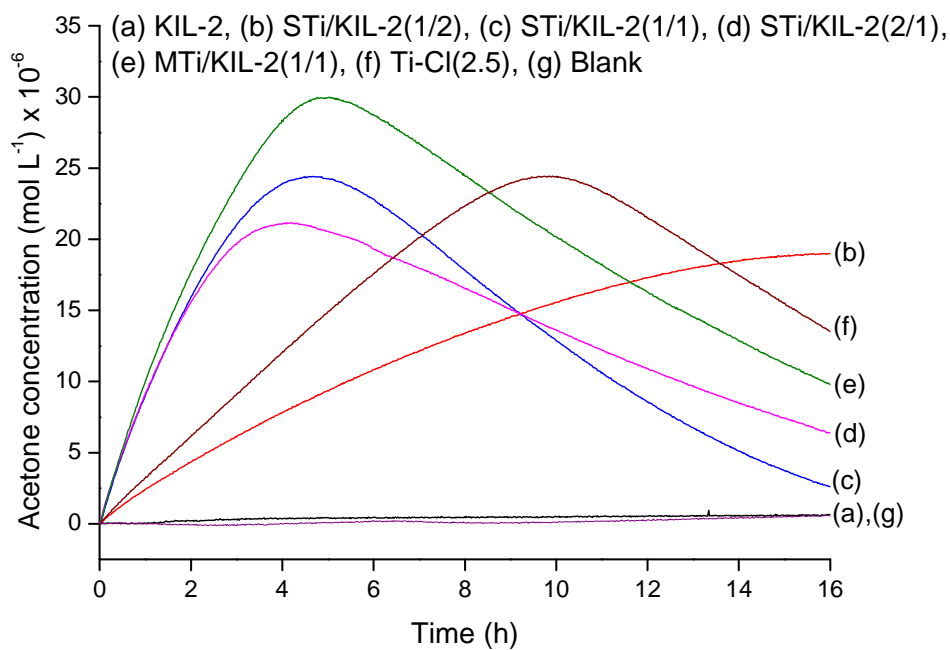


Fig 48: (A) Dark adsorption of isopropanol (negative illumination times) and its photocatalytic disappearance; (B) acetone formation curves in presence of KIL-2, STi/KIL-2(x), MTi/KIL(1/1), Ti-Cl(2.5), blank

Table 10: The acetone formation rate in the presence of different powders

Sample	Acetone formation rate constant, k_I ($\times 10^{-5}$ mol L ⁻¹ h ⁻¹)
SBA-15	–
STi/SBA-15(1/2)	1.07
STi/SBA-15(1/1)	2.68
STi/SBA-15(2/1)	1.19
MTi/SBA-15(1/1)	0.25
KIL-2	–
STi/KIL-2(1/2)	0.32
STi/KIL-2(1/1)	1.06
STi/KIL-2(2/1)	1.20
MTi/KIL-2(1/1)	1.02
Ti-Cl(2.5)	0.50

Note: The values for k_I were calculated from k_I (zero) = $C_0 / t(\text{peak})$. For all samples, the value of C_0 is taken as equal to the injected concentration that is 5×10^{-5} mol L⁻¹.

5.2.8. The photocatalytic activity towards gaseous toluene degradation

The course of adsorption and the photocatalytic degradation of toluene on the synthesized samples are shown in Figure 49. During the initial dark periods indicated by a negative time scale, adsorption/desorption processes were equilibrated. The rapid disappearance of toluene in the first 30 min corresponded to its adsorption on the surface of particular sample. As one can see in Figure 49, adsorption properties of different powders were different. In the case of SBA-15 nearly 53 % of the available toluene was adsorbed while only 8 % to 20 % for STi/SBA-15(x) samples. The highest observed capacity of SBA-15 correlates with the highest surface area of SBA-15 and probably also with its lower polarity compared to Ti/Si samples (Table 9). Adsorption capacities of STi/SBA-15(x) were decreasing with increasing Ti/Si molar ratio. This corresponds well with the observed negative trend of surface area, which decreased from 560 to 336 m² g⁻¹ by increasing the Ti/Si nominal molar ratio from 1/2 to 2/1 (Table 9). Adsorption capacity of KIL-2 was also higher compared to the STi/KIL-2(x) powders and it was again decreasing with increasing Ti/Si molar ratio (Figure 49(B)). However, adsorption capacity of KIL-2 was lower than that of SBA-15 (approximately 50 %) which correlates with their specific surface area (Table 11). Also adsorption capacities of STi/SBA-15(1/2) and STi/SBA-15(1/1) were slightly higher than those of STi/KIL-2(1/2) and STi/KIL-2(1/1), respectively,

in correspondence with their surface areas (Table 11). However, adsorption capacity of STi/SBA-15(2/1) and STi/KIL-2(2/1) were found similar even though the surface area of STi/SBA-15(2/1) was slightly higher than that of STi/KIL-2(2/1). Also adsorption capacities of unsupported TiO₂ (Ti-Cl(2.5) powder) and STi/SBA-15(2/1) were similar that does not correlate with their surface areas. It can be concluded that the deposition of titania on mesoporous silica lowers surface area of the resulting materials and at the same time specifically affects adsorption of toluene on the surface.

Figure 49 also shows the photocatalytic period of the experiments (after switching on UVA irradiation at time 0). The concentrations of toluene were decreasing according to first-order reaction (the corresponding rate constants are given in Table 11).

There was no significant disappearance of toluene in the dark experiment carried out without photocatalyst under UV irradiation (blank curve). The small observed decrease of concentration was probably due to a constant leakage of the toluene from the closed loop of the photoreactor system. As expected, the samples of bare mesoporous silica SBA-15 and KIL-2 did not show any photocatalytic activities. There was no absorption of UVA radiation by pure silica as well as no absorption of photons by toluene molecules, therefore no photochemical reactions were possible. As soon as a photocatalyst was added to the system, the photodegradation of toluene occurred. Photocatalytic degradation of toluene on Ti-Cl(2.5) proceeded more slowly compared to titania immobilized on silica. As an example, Ti-Cl(2.5) and STi/SBA-15(2/1) can be compared. They showed similar dark adsorption but the photocatalytic degradation of toluene proceeded 11 times faster in case of immobilized titania (STi/SBA-15(2/1)). The results of photocatalytic measurements can not be simply explained by taking into account only the amount of titania present in the reactor cell (the calculated amount of titania for the particular samples is reported in Table 8). In photocatalysis not only the amount of the powder is important, but many other parameters prevail. The observed lower photocatalytic activity of unsupported titania could be caused by the aggregation of titania nanoparticles in the absence of the silica support that might reduce the direct contact of gaseous molecules of toluene on the surface of TiO₂ nanoparticles. In this way the realized immobilization was found beneficial for our gaseous photocatalytic system.

In the case of SBA-15 and KIL-2 supports, the highest photocatalytic performance was found for samples with the Ti/Si molar ratio 1/1. It should be remembered in this respect that a constant amount of 0.1 g of the photocatalyst powder was loaded into the reactor cell for each experiment regardless of the Ti/Si molar ratio. It means at the same time that the amounts of TiO₂ present in the reaction system depended on the Ti/Si molar ratio as given in Table 8. In spite of this fact, the following explanation of the observed trend could be proposed. The silica surface was not completely covered by titania in 1/2 composites. That is why their photoactivity was lower compared to 1/1 composite, where the covering of silica surface by titania was higher. When the amount of titania was additionally increased in the 2/1 composite, aggregation of titania on silica surface already occurred causing the observed reduction of the photocatalytic performance. One could expect that the photoactivity would become similar to that of unsupported titania (Ti-Cl(2.5)) if more titania is additionally loaded. Kuo et al. (2009) studied the photocatalytic removal of gaseous toluene in the fluidized-bed reactor using TiO₂-coated activated carbon (AC/TiO₂) as a fluidizing medium. The toluene concentration was between 200 and 1000 ppm. The amount of the TiO₂ coating on AC was changed from 0 to 20 wt. %. When the TiO₂ loading increased from 0 to 13 wt. %, the toluene removal efficiency at steady state increased. However, when the TiO₂ loading increased from 13 to 20 wt. %, the toluene removal efficiency decreased. They found out that by increasing the amount of TiO₂, too many TiO₂ particles were coated on AC surface and hence suppressed the adsorption of toluene transferring to TiO₂ for photoreaction. In their photocatalytic reaction test conditions, the best toluene removal efficiency was found when the loading of TiO₂ on the AC was 13 % and the relative humidity was 30 %. Méndez-Román and Cardona-Martínez (1998) also studied the various oxidation products on the surface of TiO₂ P-25 and 8 % SiO₂-TiO₂ binary catalyst in the photocatalytic oxidation of gaseous toluene using in-situ FT-IR spectroscopy. SiO₂-TiO₂ binary oxide was prepared by co-fuming the Si and Ti chlorides and contained only 8 wt. % SiO₂ and 92 wt. % TiO₂ P-25. The adsorption capacity of toluene was also increased in the presence of a binary SiO₂-TiO₂ photocatalyst. They have shown that the SiO₂-TiO₂ photocatalyst was more active and deactivated slower than TiO₂ especially in the presence of water vapor.

The intermediates which are adsorbed on the surface of photocatalyst in the photocatalytic degradation of toluene depend on the reaction parameters, especially the relative humidity (RH) of the reaction environment. Sleiman et al. (2009) found that benzaldehyde, benzoic acid, and traces of benzene and formic acid are formed on the surface of TiO₂ PC500 (100 % anatase) at high and low RH level. In our case the only gaseous by-product, which was detected, was CO₂, which is the final degradation product of toluene oxidation, but the quantitative measurements of evolved CO₂ were not done.

The color of the powders was changed after photocatalytic reaction tests. It was probably associated with an accumulation of polycondensed aromatic intermediates on the photocatalyst surface according to the results published in (Barraud et al., 2005). The color of STi/SBA-15(1/2) and STi/KIL-2(1/2) changed less than that of STi/SBA-15(1/1) and STi/KIL-2(1/1), which became a light yellow. The color of samples with the Ti/Si molar ratio 2/1 was even more yellowish despite the slower toluene photodegradation. To obtain more detailed information, an analysis of the organics deposit needs to be performed. The color of the Ti-Cl(2.5) catalyst changed from cream to light brown upon irradiation that might also be due to accumulation of polycondensed aromatic intermediates (Barraud et al., 2005). One of the possible explanations for differences in color appearance could be the presence of silica. The deposited intermediates degraded faster on titania, which is in a close proximity to silica (maybe silica prevents the deposition of multilayers of organic intermediates). Therefore the unsupported titania (sample Ti-Cl(2.5) and 2/1 supported titania changed the color the most dramatically.

Guo et al. (2008) studied the photocatalytic degradation of toluene on the TiO₂ P-25 and TiO₂-activated carbon fibers (TiO₂-ACFs) in a stainless steel environmental condition controlled chamber. The effect of the various relative humidity (RH) levels (15 %, 30 %, 45 % and 60 %) on the catalyst deactivation was studied. Interestingly, no catalyst deactivation was observed under any RH conditions. The exposed ACFs served as adsorption centers of the toluene, water and intermediates, allowing intermediates to accumulate on the catalyst surface without hindering the interaction between toluene and water. They believed that lacking active sites is the reason for deactivation of catalysts and the negative effect of water under high RH.

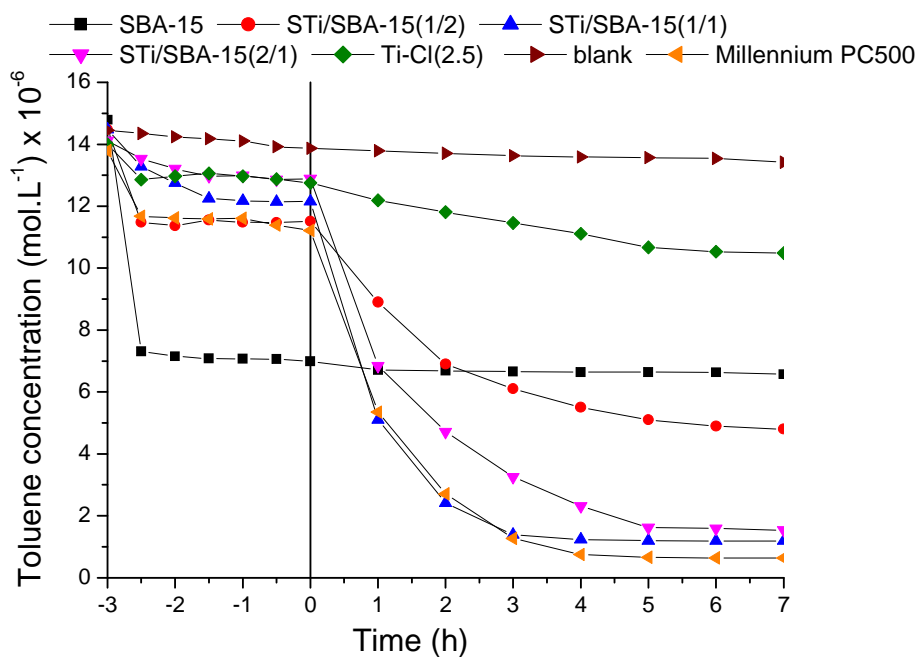
Pengyi et al. (2003) studied the degradation of the low-level gaseous toluene in the O₃/UV, TiO₂/UV and O₃/TiO₂/UV processes. The effects of the inlet concentration of toluene (1-20 ppmv), flow rate (1-5 L min⁻¹), relative humidity (20-60 %) and UV light wavelength (254 nm and 365 nm) on the conversion of toluene in the three processes were examined. The TiO₂/UV and O₃/TiO₂/UV processes were slightly affected by the relative humidity in the range of 20-55 %, the optimal humidity was around 35 % under experimental conditions studied. The TiO₂ photocatalyst film used in this study was prepared by a modified sol-gel method. The results obtained have shown that the O₃/TiO₂/UV process was the more efficient one than the O₃/UV, TiO₂/UV processes and was the most steady and applicable process among them, avoiding photocatalyst deactivation and reducing residual ozone concentration.

For comparison of our samples with commercial photocatalysts, a Millennium PC500 was chosen since it had a comparable BET surface area and similar fluidization behavior in the reactor cell as our materials. Adsorption capacity of Millennium PC500 was comparable to that of our samples with Ti/Si molar ratio 1/2, however, its photocatalytic performance was as high as for the samples which were prepared by Ti/Si molar ratio 1/1. It should be mentioned that PC500 is, as a highly crystalline material, a better photocatalyst than our unsupported titania prepared by a low-temperature synthesis. Therefore its faster reaction of toluene degradation compared to low-temperature prepared titania was not surprising. Nevertheless, we showed that even low-temperature titania can become highly photoactive when adsorbed to an appropriate substrate.

Table 11: Dark adsorption capacities and photocatalytic rate constants of used powders

Sample	Dark adsorption capacity (% of adsorbed toluene)	Rate constant of photocatalytic degradation of toluene k (h^{-1})
SBA-15	52.7	–
STi/SBA-15(1/2)	20.5	0.216
STi/SBA-15(1/1)	16.1	0.724
STi/SBA-15(2/1)	8.7	0.399
KIL-2	49.4	–
STi/KIL-2(1/2)	17.6	0.183
STi/KIL-2(1/1)	14.6	0.574
STi/KIL-2(2/1)	8.7	0.397
Ti-Cl(2.5)	8.9	0.034
Millennium PC500	18.6	0.685

A)



B)

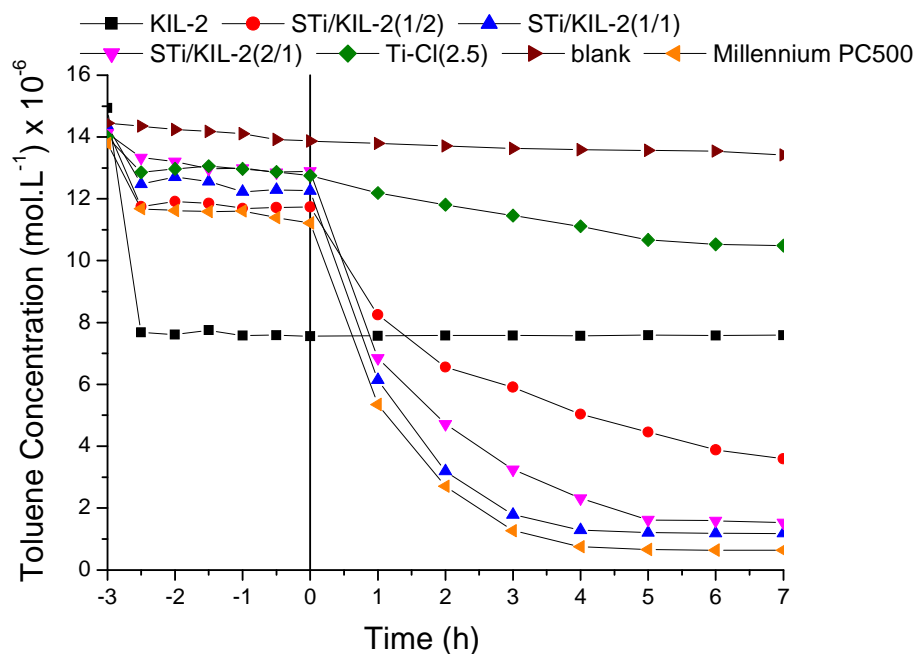


Fig 49: Concentration of toluene measured prior to and after turning on the UV lamp for (A) blank, Ti-Cl(2.5), SBA-15, STi/SBA-15(x), Millennium PC500; (B) blank, Ti-Cl(2.5), KIL-2, STi/KIL-2(x), Millennium PC500

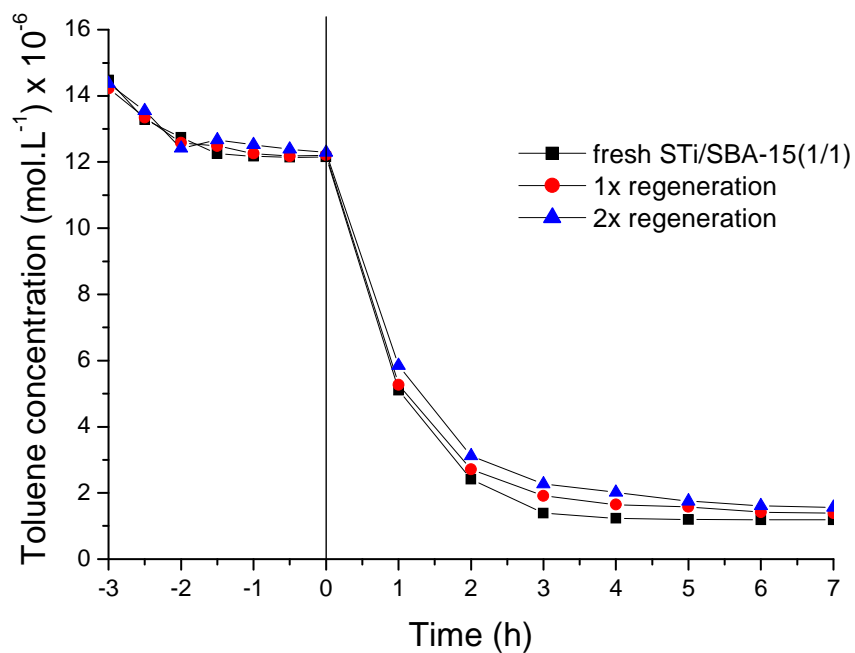
5.2.9. Regeneration of the partially deactivated photocatalyst

As it is mentioned in section 5.2.8., the color of the STi/SBA-15(1/1) and STi/KIL-2(1/1) changed from white to light yellow after the reaction, indicating that the catalysts were partially deactivated. The changed color of used photocatalysts is directly associated with the accumulation of intermediates on the surface of the photocatalysts.

In the regeneration process, the used photocatalysts were exposed to the UV in uncontaminated flowing air for 2 h (the same flow rate which was used for photocatalytic degradation of toluene, 0.2 L min^{-1}). Figure 50 shows the adsorption and photocatalytic degradation of toluene on the fresh and regenerated STi/SBA-15(1/1) and STi/KIL-2(1/1) powders. In the Figure 50, fresh, once regenerated and twice regenerated samples are compared.

As it is indicated, the differences of the adsorption capacity and photocatalytic activity of fresh and regenerated STi/SBA-15(1/1) powders were not significant. However, the photocatalytic activity of STi/KIL-2(1/1) powder decreased by regeneration. It is believed that the formed intermediates during the reaction can not be completely removed from the surface of the photocatalysts, which might be due to the different structure of the KIL-2 supporting materials and hence possibly stronger interaction with the intermediates.

A)



B)

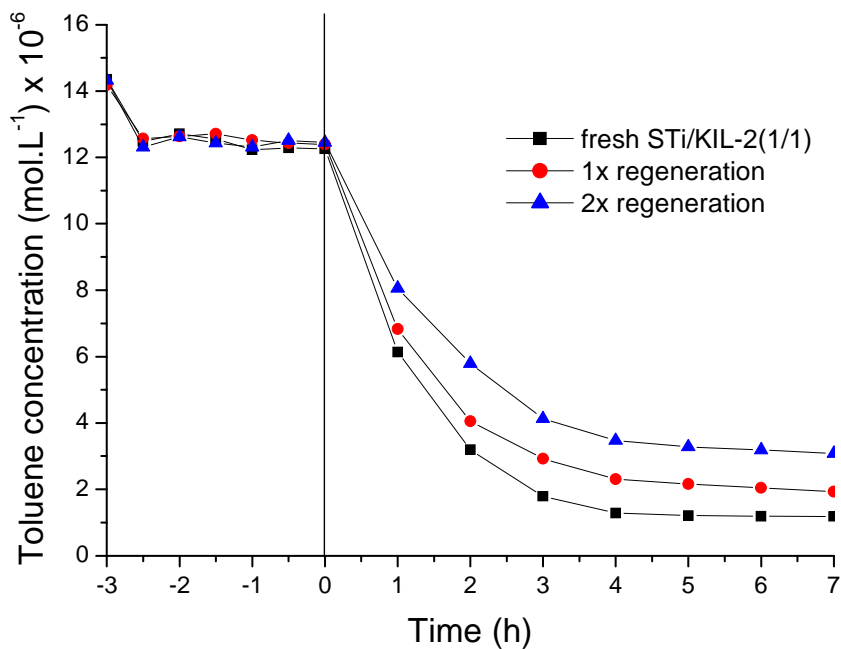


Fig 50: Concentration of toluene measured prior to and after turning on the UV lamp for (A) fresh STi/SBA-15(1/1), 1x regenerated STi/SBA-15(1/1), 2x regenerated STi/SBA-15(1/1); (B) fresh STi/KIL-2(1/1), 1x regenerated STi/KIL-2(1/1), 2x regenerated STi/KIL-2(1/1)

VI. Conclusions

The nanocrystalline TiO₂ sol and powders were prepared from titanium tetrachloride by using the low-temperature sol-gel method. After obtaining the refluxed sol, the solvent (water) was evaporated and the final powder consisted of TiO₂ with some amount of the acid. The remaining acid in the powder prevents the aggregation of synthesized TiO₂ particles; therefore the as-prepared samples can be dispersed freely in the aqueous solution obtaining stable, translucent and even transparent sols also in concentration of TiO₂ as high as 2 mol L⁻¹. The properties of the prepared samples depend mainly on the type of the acid and less on its quantity. Using HClO₄ instead of HNO₃ as the peptizing agent resulted in approximately two times smaller colloidal particles of TiO₂ in the obtained sol. This correlates well with BET results, where the surface area of Ti-Cl powders was approximately twice higher than the surface area of the Ti-N powders. The photocatalytic activity of TiO₂ prepared by using HClO₄ was approximately 1.5 times higher than the activity of similar catalysts prepared by using HNO₃. Due to the fact that the anatase crystallite size was similar in powders prepared with HClO₄ and in powder prepared with HNO₃, it is supposed that a smaller size of aggregated colloidal particles in aqueous solution presents the main reason for better photocatalytic activity of HClO₄-based TiO₂.

Afterwards, in order to increase the photocatalytic activity of the as-prepared TiO₂ powder in gaseous phase, titania-containing ordered and disordered mesoporous silica (SBA-15 and KIL-2) have been synthesized with different Ti/Si nominal molar ratios (1/2, 1/1, 2/1) using sol-gel impregnation method. Aqueous nanocrystalline titania sol was used as a source of titania (photoactive component) while silica mesoporous materials were employed as a high-surface area supports. For comparison, titanium isopropoxide in acidic solution was also used as a source of titania. The adsorption capacity and photoactivity of powders were investigated towards photocatalytic degradation of gaseous toluene in a fluidized-bed photoreactor which was constructed for this purpose. The properties of the prepared samples depend on titania precursor, preparation conditions and the type of the framework of the mesoporous silica materials.

The results reveal that ordered mesoporous SBA-15 type and disordered mesoporous KIL-2 type with textural porosity has a major effect on the structural properties and

photocatalytic activity. It can be seen that the order of the SBA-15 framework was maintained upon impregnation with nanocrystalline titania sol while it was destroyed by using Ti-isopropoxide. The increase of Ti/Si molar ratio led to decrease of the surface area and random dispersion of titania nanoparticles inside the channels of SBA-15 thus narrowing parts of the mesopores of SBA-15. Further increase of titania amount results on the growth of the titania particles on the external surface of the silica support. The adsorption capacities of the titania containing SBA-15 powders are in concurrence with the surface area which is decreasing by increasing the titania amount (the growth of anatase plugs inside the channels of SBA-15 materials). Thus the total capacity to adsorb toluene is the highest in the presence of SBA-15, which is in agreement with the highest surface area of SBA-15 and decreases with the growth of the titania nanoparticles due to partial blocking of the mesopores. The adsorption capacities of titania containing KIL-2 powders shows the behavior similar to the titania containing SBA-15, with an exception of powder that was prepared with Ti/Si molar ratio 2/1 and supported (immobilized) on KIL-2, where the adsorption capacity was higher than expected. The photocatalytic activity depends on the accessibility and the number of titania nanoparticles. In powder that was prepared with Ti/Si molar ratio 1/1 and supported (immobilized) on SBA-15, the loading of titania was not too high to decrease accessibility and not too low to ensure sufficient quantity of active nanoparticles for reaction, therefore among all the investigated samples the photocatalytic activity was the highest in the presence of the powder which was prepared with Ti/Si molar ratio 1/1 and SBA-15 as a support.

The photocatalytic degradation of isopropanol in gaseous medium results show that the adsorption capacity of isopropanol is the highest in the presence of the SBA-15-supported materials. The photoactivity results indicate that the powder which are prepared using SBA-15 and a nominal Ti/Si molar ratio of 1/1 are the most active toward isopropanol oxidation.

As a conclusion the photocatalytic activity results obtained from two different solid-gas photoreactor systems confirm the beneficial influence of the mesoporous support on the low-temperature prepared titania for the removal of an organic contaminant from the gaseous phase, in the dark adsorption as well as in the photocatalytic stage of the process.

The main results of my Ph.D. work were published within three original scientific articles in the peer-reviewed international journals:

- 1- Tasbihi M., Lavrenčič Štangar U., Černigoj U., Kogej K. 2009. Low-temperature synthesis and characterization of anatase TiO₂ powders from inorganic precursors. *Photochem. Photobiol. Sci.*, 8: 719–725.
- 2- Tasbihi M., Lavrenčič Štangar U., Sever Škapin A., Ristić A., Novak Tušar N. 2010. Titania-containing mesoporous silica powders: structural properties and photocatalytic activity towards isopropanol degradation. *J. Photochem. Photobiol. A: Chem.*, 216: 167-178.
- 3- Tasbihi M., Lavrenčič Štangar U., Černigoj U., Jirkovsky J., Bakardjievac, S. Novak Tušar N. 2010. Photocatalytic oxidation of gaseous toluene on titania/mesoporous silica powders in a fluidized-bed reactor. *Catalysis Today*, doi:10.1016/j.cattod.2010.08.015.

VII. References

- Addamo M., Augugliaro V., Di Paola A., Garcia-Lopez E., Loddo V., Marc G., Palmisano L. 2005. Preparation and photoactivity of nanostructured TiO₂ particles obtained by hydrolysis of TiCl₄. *Coll. Surf. A. Physicochem. Eng. Aspect*, 265: 23–31.
- Ambrus Z., Mogyrosi K., Szalai A., Alapi T., Demeter K., Dombi A., Sipos P. 2008. Low temperature synthesis, characterization and substrate-dependent photocatalytic activity of nanocrystalline TiO₂ with tailor-made rutile to anatase ratio. *Appl. Catal. A. General*, 340: 153–161.
- Andersson S.L.T. 1986. Reaction networks in the catalytic vapor/phase oxidation of toluene and xylenes. *J. Catal.*, 98: 138–149.
- Augugliaro V., Coluccia S., Loddo V., Marchese L., Martra G., Palmisano L., Schiavello M. 1999. Photocatalytic oxidation of gaseous toluene on anatase TiO₂ catalyst: mechanistic aspects and FT-IR investigation. *Appl. Catal. B. Environ.*, 20: 15–27.
- Bagshaw S.A., Prouzet. E., Pinnavaia T.J. 1995. Templating of mesoporous molecular sieves by nonionic polyethylene oxide surfactants. *Science*, 269: 1242–1244.
- Barraud E., Bosc F., Edwards D., Keller N., Keller V. 2005. Gas phase photocatalytic removal of toluene effluents on sulfated titania. *J. Catal.*, 235: 318–326.
- Barrett E.P., Joyner L.G., Halenda P.P. 1951. The determination of pore volume and area distributions in porous substances. I. Computations from nitrogen isotherms. *J. Am. Chem. Soc.*, 73: 373–380.
- Bickley R.I., Munuera G., Stone F.S. 1973. Photoadsorption and photocatalysis at rutile surfaces. II. Photocatalytic oxidation of isopropanol. *J. Catal.*, 31: 398–407.

Blount M.C., Falconer J.L. 2002. Steady-state surface species during toluene photocatalysis. *Appl. Catal. B. Environ.*, 39: 39–50.

Boccuti M.R., Rao K.M., Zecchina A., Leofanti G., Petrini G. 1989. Spectroscopic characterization of silicalite and titanium-silicalite. *Stud. Surf. Sci. Catal.*, 48: 133–144.

Bouzaza A., Vallet C., Laplanche A. 2006. Photocatalytic degradation of some VOCs in the gas phase using an annular flow reactor, determination of the contribution of mass transfer and chemical reaction steps in the photodegradation process. *J. Photochem. Photobiol. A. Chem.*, 77: 212–217.

Brinker C. J., Scherer G.W. 1990. *Sol-gel science*, Academic Press, Inc.

Brunauer S., Emmett P.H., Teller E. 1938. Adsorption of gases in multimolecular layers. *J. Am. Chem. Soc.*, 60: 309–319.

Burgeth G., Kisch H. 2002. Photocatalytic and photoelectrochemical properties of titania-chloroplatinate(IV). *Coord. Chem. Rev.*, 230: 41–47.

Busca G., Berardinelli S., Resini C., Arrighi L. 2008. Technologies for the removal of phenol from fluid streams: a short review of recent developments. *J. Hazard. Mater.*, 160: 265–288.

Busuioc A.M., Meynen V., Beyers E., Mertens M., Cool P., Bilba N., Vansant E. F. 2006. Structural features and photocatalytic behaviour of titania deposited within the pores of SBA-15. *Appl. Catal. A. General*, 312: 153–164.

Calleja G., van Grieken R., Garcia R., Melero J.A., Iglesias J. 2002. Preparation of titanium molecular species supported on mesostructured silica by different grafting methods. *J. Mol. Catal. A: Chem.*, 182–183: 215–225.

Carey J.H., Lawrence J., Tosine H.M. 1976. Photodechlorination of PCB's in the presence of titanium dioxide in aqueous suspensions. *Bull. Environ. Contam. Toxicol.*, 16: 697–701.

Carp O., Huisman C.L., Reller A. 2004. Photoinduced reactivity of titanium dioxide. *Progress Solid State Chem.*, 32: 33–177.

Celer E.B., Kruk M., Zuzek Y., Jaroniec M. 2006. Hydrothermal stability of SBA–15 and related ordered mesoporous silicas with plugged pores. *J. Mater. Chem.*, 16: 2824–2833.

Černigoj U., Lavrenčič Štangar U., Trebše P. 2007. Evaluation of a novel carberry type photoreactor for the degradation of organic pollutants in water. *J. Photochem. Photobiol. A. Chem.*, 188: 169–176.

Chen D., Ray A.K. 1999. Photocatalytic kinetics of phenol and its derivatives over UV irradiated TiO₂. *Appl. Catal. B. Environ.*, 23: 143–157.

Chen W., Zhang J.S., Zhang Z. 2005. Performance of air cleaners for removing multiple volatile organic compounds indoor air. *ASHRAE Transactions*.

Chen Y., Huang Y., Xiu J., Han X., Bao X. 2004. Direct synthesis, characterization and catalytic activity of titanium–substituted SBA–15 mesoporous molecular sieves. *Appl. Catal. A. General*, 273: 185–191.

D'Hennezel O., Pichat P., Ollis D.F. 1998. Benzene and toluene gas–phase photocatalytic degradation over H₂O and HCl pretreated TiO₂: by–products and mechanisms. *J. Photochem. Photobiol. A. Chem.*, 118: 197–204.

De Lasa H., Serrano B., Salaices M. 2005. Photocatalytic reaction engineering, Springer.

De Witte K., Cool P., De Witte I., Ruys L., Rao J., Tendeloo G.V., Vansant E.F. 2007. Multistep loading of titania nanoparticles in the mesopores of SBA-15 for enhanced photocatalytic activity. *J. Nanosci. Nanotechnol.*, 7: 1-5.

Ding H., Sun H., Shan Y. 2005. Preparation and characterization of mesoporous SBA-15 supported dye-sensitized TiO₂ photocatalyst. *J. Photochem. Photobiol. A: Chem.*, 169: 101-107.

Durgakumari V., Subrahmanyam M., Subba Rao K.V., Ratnamala A., Noorjahan M., Tanaka K. 2002. An easy and efficient use of TiO₂ supported HZSM-5 and TiO₂+HZSM-5 zeolite combine in the photodegradation of aqueous phenol and *p*-chlorophenol. *Appl. Catal. A. General*, 234: 155-165.

EC directive 1999/13/EC (Solvent Emissions Directive).

Einaga H., Futamura S., Ibusuki T. 2002. Heterogeneous photocatalytic oxidation of benzene, toluene, cyclohexene and cyclohexane in humidified air: comparison of decomposition behavior on photoirradiated TiO₂ catalyst. *Appl. Catal. B: Environ.*, 38: 215-225.

Enriquez R., Agrios A.G., Pichat P. 2007. Probing multiple effects of TiO₂ sintering temperature on photocatalytic activity in water by use of a series of organic pollutant molecules. *Catal. Today*, 120: 196-202.

Esplugas S., Gimenez J., Contreras S., Pascual E., Rodriguez M. 2002. Comparison of different advanced oxidation processes for phenol degradation. *Water Res.*, 36: 1034-1042.

Fuertes A.B. 2004. Synthesis of mesostructured silica with tailorable textural porosity and particle size. *Mater. Lett.*, 58: 1494-1497.

Fujishima A., Honda K. 1972. Electrochemical photolysis of water at the semiconductor electrode. *Nature*, 238: 37-38.

Gao B., Peng C., Chen G.Z., Li Puma G. 2008. Photo-electro-catalysis enhancement on carbon nanotubes/titanium dioxide (CNTs/TiO₂) composite prepared by a novel surfactant wrapping sol-gel method. *Appl. Catal. B. Environ.*, 85: 17–23.

Gimeno M.P., Gascon J., Tellez C., Herguido J., Menendez M. 2008. Selective oxidation of *o*-xylene to phthalic anhydride over V₂O₅/TiO₂: kinetic study in a fluidized bed reactor. *Chem. Eng. Process*, 47: 1844–1852.

Grieken R.V., Aguado J., Lopez-Munoz M.J., Marugan J. 2002. Synthesis of size-controlled silica-supported TiO₂ photocatalysts. *J. Photochem. Photobiol. A. Chem.*, 148: 315–322.

Guillard C., Beaugiraud B., Dutriez C., Herrmann J-M, Jaffrezic H., Jaffrezic-Renault N., Lacroix M. 2002. Physicochemical properties and photocatalytic activities of TiO₂-films prepared by sol-gel methods. *Appl. Catal. B: Environ.*, 39: 331–342.

Guo T., Bai Z., Wu C., Zhu T. 2008. Influence of relative humidity on the photocatalytic oxidation (PCO) of toluene by TiO₂ loaded on activated carbon fibers: PCO rate and intermediates accumulation. *Appl. Catal. B. Environ.*, 79: 171–178.

Haskouri J.E., Morales J.M., Zarate D.O., Fernandez L., Latorre J., Guillem C., Beltran A., Beltran D., Amoros P. 2008. Nanoparticulated silicas with bimodal porosity: chemical control of the pore sizes. *Inorg. Chem.*, 47: 8267–8277.

Herrmann J.M. 1999. Heterogeneous photocatalysis: fundamentals and applications to the removal of various types of aqueous pollutants. *Catal. Today*, 53: 115–129.

Hoffmann M.R., Martin S.T., Choi W., Bahnemann D.W. 1995. Environmental applications of semiconductor photocatalysis. *Chem. Rev.*, 95: 69–96.

Howard J.R. 1989. *Fluidized bed technology: principles and applications*, Adam Higler.

- Hu S., Wang H., Cao J., Liu J., Fang B., Zheng M., Ji G., Zhang F., Yang Z. 2008. Synthesis of mesostructure anatase TiO₂ particles in room-temperature ionic liquids. *Mater. Lett.*, 62: 2954–2956.
- Ibusuki T., Takeuchi K. 1986. Toluene oxidation on UV-irradiated titanium dioxide with and without O₂, NO₂ or H₂O at ambient temperature. *Atmos. Environ.*, 20: 1711–1715.
- Janik J.M., Pytasz G., Stanek T. 1969. An infra-red study of crystallo-hydrates. *Acta Physica Polonica*, XXXV: 997–1008.
- Jansen J.C., Shan Z., Maschmeyer Th., Marchese L., Zhou W., Puil N.V.D. 2001. A new templating method for three-dimensional mesopore networks. *Chem. Commun.*, 713–714.
- Jones A.P. 1999. Indoor air quality and health. *Atmos. Environ.*, 33(28): 4535–4564.
- Jung W.Y., Baek S.H., Yang J.S., Lim K., Lee M.S., Lee G., Park S.S., Hong S. 2008. Synthesis of Ti-containing SBA-15 materials and studies on their photocatalytic decomposition of orange II. *Catal. Today*, 131: 437–443.
- Kanna M., Wongnawa S. 2008. Mixed amorphous and nanocrystalline TiO₂ powders prepared by sol-gel method: characterization and photocatalytic study. *Mater. Chem. Phys.*, 110: 166–175.
- Kim S.B., Hong S.C. 2002. Kinetic study for photocatalytic degradation of volatile organic compounds in air using thin film TiO₂ photocatalyst. *Appl. Catal. B. Environ.*, 35: 305–315.
- Koči K., Obalová L., Matějová L., Plachá D., Lacný Z., Jirkovský J., Šolcová O. 2009. Effect of TiO₂ particle size on the photocatalytic reduction of CO₂. *Appl. Catal. B: Environ.*, 89: 494–502.

Kruk M., Jaroniec M. 2001. Gas adsorption characterization of ordered organic–inorganic nanocomposite materials. *Chem. Mater.*, 13: 3169–3183.

Kruk M., Jaroniec M., Joo S.H., Ryoo R. 2003. Characterization of regular and plugged SBA–15 silicas by using adsorption and inverse carbon replication and explanation of the plug formation mechanism. *J. Phys. Chem. B.*, 107: 2205–2213.

Kruk M., Jaroniec M., Ko C.H., Ryoo R. 2000. Characterization of the porous structure of SBA–15. *Chem. Mater.*, 12: 1961–1968.

Ku Y., Tseng K., Wang W. 2005. Decomposition of gaseous acetone in an annular photoreactor coated with TiO₂ thin film. *Water Air Soil Pollut.*, 168: 313–323.

Kuo H.P., Wu C.T., Hsu R.C. 2009. Continuous reduction of toluene vapors from the contaminated gas stream in a fluidized bed photoreactor. *Powder Technology*, 195: 50–56.

Landau M.V., Vradman L., Wang X., Titelman L. 2005. High loading TiO₂ and ZrO₂ nanocrystals ensembles inside the mesopores of SBA–15: preparation, texture and stability. *Micropor. Mesopor. Mater.*, 78: 117–129.

Larson S.A., Widegren J.A., Falconer J.L. 1995. Transient studies of 2–propanol photocatalytic oxidation on titania. *J. Catal.*, 157: 611–25.

Lavrenčič Štangar U., Černigoj U., Trebše P., Maver K., Gross S. 2006. Photocatalytic TiO₂ coatings: effect of substrate and template. *Monatsh. Chem.*, 137: 647–655.

Lee D.S., Liu T.K. 2002. Preparation of TiO₂ sol using TiCl₄ as a precursor. *J. Sol–Gel Sci. Technol.*, 25: 121–136.

Levenspiel O. 1999. *Chemical reaction engineering*, 3rd ed. John Wiley & Sons.

Li Puma G., Bono A., Krishnaiah D., Collin J.G. 2008. Preparation of titanium dioxide photocatalyst loaded onto activated carbon support using chemical vapor deposition: A review paper. *J. Hazard. Mater.*, 157: 209–219.

Lim M., Rudolph V., Anpo M., Lu G.Q. 2008. Fluidized-bed photocatalytic degradation of airborne styrene. *Catal. Today*, 131: 548–552.

Lim T.H., Jeong S.M., Kim S.D., Gyenis J. 2000. Photocatalytic decomposition of NO by TiO₂ particles. *J. Photochem. Photobiol. A. Chem.*, 134: 209–217.

Lim T.H., Kim S.D. 2004. Trichloroethylene degradation by photocatalysis in annular flow and annular fluidized bed photoreactors. *Chemosphere*, 54: 305–312.

Lin K., Cooper W.J., Nickelsen M.G., Kurutz C.N., Waite T.D. 1995. Decomposition of aqueous solutions of phenol using high energy electron beam irradiation – a large scale study. *Appl. Radiat. Isot.*, 46: 1307–1316.

Linssen T., Cassiers K., Cool P., Vansant E.F. 2003. Mesoporous templated silicates: an overview of their synthesis, catalytic activation and evaluation of the stability. *Adv. Coll. Inter. Sci.*, 103: 121–147.

Litter M.I. 1999. Heterogeneous photocatalysis, transition metal ions in photocatalytic systems. *Appl. Catal. B. Environ.*, 23: 89–114.

Liu T., Li F., Li X. 2008a. Effects of peptizing conditions on nanometer properties and photocatalytic activity of TiO₂ hydrosols prepared by H₂TiO₃. *J. Hazard. Mater.*, 155: 90–99.

Liu T., Li F., Li X. 2008b. TiO₂ hydrosols with high activity for photocatalytic degradation of formaldehyde in a gaseous phase. *J. Hazard. Mater.*, 152: 347–355.

Long Y., Xu T., Sun Y., Dong W. 1998. Adsorption behavior on defect structure of mesoporous molecular sieve MCM-41. *Langmuir*, 14: 6173–6178.

Lopez–Munoz M.J., Grieken R.V., Aguado J., Marugan J. 2005. Role of the support on the activity of silica–supported TiO₂ photocatalysts: structure of the TiO₂/SBA–15 photocatalysts. *Catal. Today*, 101: 307–314.

Luan Z., Kevan L. 2001. Characterization of titanium–containing mesoporous silica molecular sieve SBA–15 and generation of paramagnetic hole and electron centers. *Micropor. Mesopor. Mater.*, 44–45: 337–344.

Luan Z., Maes E.M., Heide P.A.W., Zhao D., Czernuszewicz R.S., Kevan L. 1999. Incorporation of titanium into mesoporous silica molecular sieve SBA–15. *Chem. Mater.*, 11: 3680–3686.

Lukens Jr. W.W., Schmidt–Winkel P., Zhao D., Feng J., Stucky G.D. 1999. Evaluating pore sizes in mesoporous materials: a simplified standard adsorption method and a simplified Broekhoff–de Boer method. *Langmuir*, 15: 5403–5409.

Maggos T., Bartzis J.G., Leva P., Kotzias D. 2007. Application of photocatalytic technology for NO_x removal. *Appl. Phys. A.*, 89: 81–84.

Marci G., Addamo M., Augugliaro V., Coluccia S., Garcia–Lopez E., Loddo V., Martra G., Palmisano L., Schiavello M. 2003. Photocatalytic oxidation of toluene on irradiated TiO₂: comparison of degradation performance in humidified air, in water and in water containing a zwitterionic surfactant. *J. Photochem. Photobiol. A. Chem.*, 160: 105–114.

Mazaj M., Stevens W.J.J., Zabukovec Logar N., Ristić A., Novak Tušar N., Arčon I., Daneu N., Meynen V., Cool P., Vansant E.F., Kaučič V. 2009. Synthesis and structural investigations on aluminium–free Ti–Beta/SBA–15 composite. *Micropor. Mesopor. Mater.*, 117: 458–465.

McQuillan A.J. 2001. Probing solid–solution interfacial chemistry with ATR–IR spectroscopy of particle films. *Adv. Mater.*, 13: 1034–1038.

Méndez-Román R., Cardona-Martínez N. 1998. Relationship between the formation of surface species and catalyst deactivation during the gas-phase photocatalytic oxidation of toluene. *Catal. Today*, 40: 353-365.

Meynen V., Cool P., Vansant E.F., Kortunov P., Grinberg F., Karger J., Martens M., Lebedev O.I., Van Tendeloo G. 2007. Deposition of vanadium silicate-1 nanoparticles on SBA-15 materials. Structural and transport characteristics of SBA-VS-15. *Micropor. Mesopor. Mater.*, 99: 14-22.

Meynen V., Beyers E., Cool P., Vansant E.F., Mertens M., Weyten H., Lebedev O.I., Van Tendeloo G. 2004. Post-synthesis deposition of V-zeolitic nanoparticles in SBA-15. *Chem. Commun.*, 898-890.

Miyazawa K., Inagaki S. 2000. Control of the microporosity within the pore walls of ordered mesoporous silica SBA-15. *Chem. Commun.*, 2121-2122.

Mukherjee P.S., Ray A.K. 1999. Major challenges in the design of a large-scale photocatalytic reactor for water treatment. *Chem. Eng. Technol.*, 22: 253-260.

Munuera G., Stone F.S. 1971. Adsorption of water and organic vapours on hydroxylated rutile, *Discussions of the Faraday Society*, 52: 205-214.

Murov S.L., Carmichael I., Hug G.L. 1993. *Handbook of photochemistry*, 2nd ed. Marcel Dekker Inc., 1993, 299-305.

Music S., Gotic M., Ivanda M., Popovic S., Turkovic A., Trojko R., Sekulic A., Furi K. 1997. Chemical and microstructural properties of TiO₂ synthesized by sol-gel procedure. *Mater. Sci. Eng.*, B47: 33-40.

Na Y., Kim D., Lee C., Lee S., Park Y., Oh Y., Park S., Song S. 2004. Photocatalytic decolorization of rhodamine B by fluidized bed reactor with hollow ceramic ball photocatalyst. *Korean J. Chem. Eng.*, 21: 430-435.

Nag M., Basak P., Manorama S.V. 2007. Low-temperature hydrothermal synthesis of phase-pure rutile titania nanocrystals: time temperature tuning of morphology and photocatalytic activity. *Mater. Res. Bull.*, 42: 1691–1704.

Novak Tušar N., Ristić A., Mali G., Mazaj M., Arčon I., Arčon D., Kaučič V., Zabukovec Logar N. 2010. MnO_x nanoparticles supported on a new mesostructured silicate with textural porosity. *Chem. Eur. J.*, 16: 5783–5793.

Obuchi E., Sakamoto T., Nakano K. 1999. Photocatalytic decomposition of acetaldehyde over TiO₂/SiO₂ catalyst. *Chem. Eng. Sci.*, 54: 1525–1530.

Ohko Y., Fujishima A., Hashimoto K. 1998. Kinetic analysis of the photocatalytic degradation of gas-phase 2-propanol under mass transport-limited conditions with a TiO₂ film photocatalyst. *J. Phys. Chem. B*, 102: 1724–1729.

Oppenlander T. 2003. Photochemical purification of water and air, Wiley-Vch Verlag GmbH & Co.

Paschoalino M.P., Kiwi J., Jardim W.F. 2006. Gas-phase photocatalytic decontamination using polymer supported TiO₂. *Appl. Catal. B. Environ.*, 68: 68–73.

Pengyi Z., Fuyan L., Gang Y., Qing C., Wanpeng Z. 2003. A comparative study on decomposition of gaseous toluene by O₃/UV, TiO₂/UV and O₃/TiO₂/UV. *J. Photochem. Photobiol. A: Chem.*, 156: 189-194.

Perathoner S., Lanzafame P., Passalacqua R., Centi G., Schlog R., Su D.S. 2006. Use of mesoporous SBA-15 for nanostructuring titania for photocatalytic applications. *Micropor. Mesopor. Mater.*, 90: 347–361.

Pozzo R.L., Baltanas M.A., Cassano A.E. 2006. Fluidized bed photoreactors using composites of titania CVD-coated onto quartz sand as photocatalyst: assessment of photochemical efficiency. *Chem. Eng. J.*, 118: 153–159.

Pozzo R.L., Giombi J.L., Baltanas M.A., Cassano A.E. 2000. The performance in a fluidized bed reactor of photocatalysts immobilized onto inert supports. *Catal. Today*, 62: 175–187.

Prieto O., Feroso J., Irusta R. 2007. Photocatalytic degradation of toluene in air using a fluidized bed photoreactor. *International J. Photoenergy*, Article ID 32859, doi:10.1155/2007/32859.

Qiu W., Zheng Y. 2007. A comprehensive assessment of supported titania photocatalysts in a fluidized bed photoreactor: photocatalytic activity and adherence stability. *Appl. Catal. B. Environ.*, 71: 151–162.

Random C., Wongnawa S., Boonsin P. 2004. Bleaching of methylene blue by hydrated titanium dioxide. *Sci. Asia*, 30: 149–156.

Sayari A., Liu P., Kruk M., Jaroniec M. 1997. Characterization of large-pore MCM-41 molecular sieves obtained via hydrothermal restructuring. *Chem. Mater.*, 9: 2499–2506.

Schiavello M. 1988. *Photocatalysis and environment. Trends and applications.* Kluwer Academic Publishers, Dordrecht.

Schneider M., Baiker A. 1997. Titania-based aerogel. *Catal. Today*, 35: 339–365.

Schubert U., Hüsing N. 2005. *Synthesis of inorganic materials*, Wiley-Vch Verlag GmbH & Co.

Sekiguchi K., Yamamoto K., Sakamoto K. 2008. Photocatalytic degradation of gaseous toluene in an ultrasonic mist containing TiO₂ particles. *Catal. Commun.*, 9: 281–285.

Senthilkumaar S., Porkodi K., Vidyalakshmi R. 2005. Photodegradation of a textile dye catalyzed by sol-gel derived nanocrystalline TiO₂ via ultrasonic irradiation. *J. Photochem. Photobiol. A: Chem.*, 170: 225–232.

Serpone N., Pelizzetti E. (Eds.). 1989. Photocatalysis. Fundamentals and applications, Wiley Interscience, New York.

Shankar M.V., Anandan S., Venkatachalam N., Arabindoo B., Murugesan V. 2006. Fine route for an efficient removal of 2, 4-dichlorophenoxyacetic acid (2,4-D) by zeolite-supported TiO₂. Chemosphere, 63: 1014–1021.

Sing K.S.W., Everett D.H., Hau R.A.W., Moscou L., Pierotti R.A., Rouquero J., Siemieniewska T. 1985. Reporting physisorption data for gas/solid systems with special reference to the determination of surface area and porosity. Pure Appl. Chem., 57: 603–619.

Sitkiewitz S., Heller A. 1996. Photocatalytic oxidation of benzene and stearic acid on sol-gel derived TiO₂ thin films attached to glass. New J. Chem., 20: 233–241.

Sleiman M., Conchon P., Ferronato C., Chovelon J-M. 2009. Photocatalytic oxidation of toluene at indoor air levels (ppbv): towards a better assessment of conversion, reaction intermediates and mineralization. Appl. Catal. B: Environ., 86: 159–165.

Sobczynski A., Duczma L., Zmudzinski W. 2004. Phenol destruction by photocatalysis on TiO₂: an attempt to solve the reaction mechanism. J. Molecular Catal. A. Chem., 213: 225–230.

Sonntag C.V., Schuchmann H.-P. 1991. The elucidation of peroxy radical reactions in aqueous solution with the help of radiation-chemical methods. Angew. Chem. Int. Ed. Engl., 30: 1229–1253.

Strini A., Cassese S., Schiavi L. 2005. Measurement of benzene, toluene, ethylbenzene and *o*-xylene gas phase photodegradation by titanium dioxide dispersed in cementitious materials using a mixed flow reactor. Appl. Catal. B. Environ., 61: 90–97.

Takeda N., Torimoto T., Sampath S., Kuwabata S., Yoneyama H. 1995. Effect of the inert supports for titanium dioxide loading on enhancement of photodecomposition rate of gaseous propionaldehyde. *J. Phys. Chem.*, 99: 9986–9991.

Tan B., Lehmler H–J., Vyas S.M., Knutson B.L., Rankin S.E. 2005. Large– and small–nanopore silica prepared with a short–chain cationic fluorinated surfactant. *Nanotechnology*, 16: S502–S507.

Tanev P.T., Vlaev L.T. 1993. An attempt at a more precise evaluation of the approach to mesopore size distribution calculations depending on the degree of pore blocking. *J. Colloid Interface Sci.*, 160: 110–116.

Tasbihi M., Lavrenčič Štangar U., Černigoj U., Jirkovsky J., Bakardjieva S., Novak Tušar N. 2010b. Photocatalytic oxidation of gaseous toluene on titania/mesoporous silica powders in a fluidized–bed reactor. doi: 10.1016/j.cattod.2010.08.015.

Tasbihi M., Lavrenčič Štangar U., Černigoj U., Kogej K. 2009. Low–temperature synthesis and characterization of anatase TiO₂ powders from inorganic precursors. *Photochem. Photobiol. Sci.*, 8: 719–725.

Tasbihi M., Lavrenčič Štangar U., Sever Škapin A., Ristić A., Novak Tušar N. 2010a. Titania–containing mesoporous silica powders: structural properties and photocatalytic activity towards isopropanol degradation. *J. Photochem. Photobiol. A: Chem.*, 216: 167–178.

Tasbihi M., Rohaida Ngah C., Aziz N., Mansor A., Abdullah A.Z., Teong L.K., Mohamed A.R. 2007. Lifetime and regeneration studies of various supported TiO₂ photocatalysts for the degradation of phenol under UV–C light in a batch reactor. *Ind. Eng. Chem. Res.*, 46: 9006–9014.

Tomasic V., Jovic F., Gomzi Z. 2008. Photocatalytic oxidation of toluene in the gas phase: modelling an annular photocatalytic reactor. *Catal. Today*, 137: 350–356.

Tuel A. 1999. Modification of mesoporous silicas by incorporation of heteroelements in the framework. *Micropor. Mesopor. Mater.*, 27: 151–169.

Urban C., Schurtenberger. 1998. Characterization of turbid colloidal suspensions using light scattering techniques combined with cross-correlation methods. *P. J. Coll. Inter. Sci.*, 207: 150–158.

Van der Voort P., Ravikovitch P.I., De Jong K.P., Benjelloun M., Van Bavel E., Janssen A.H., Neimark A.V., Weckhuysen B.M., Vansant E.F. 2002. A new templated ordered structure with combined micro- and mesopores and internal silica nanocapsules. *J. Phys. Chem. B.*, 106: 5873–5877.

Velasco M.J., Rubio F., Rubio J., Oteo J.L. 1999. DSC and FT-IR analysis of the drying process of titanium alkoxide derived precipitates. *Thermochim. Acta*, 326: 91–97.

Wang W., Song M. 2006. Multistep impregnation method for incorporation of high amount of titania into SBA-15. *Mater. Res. Bull.*, 41: 436–447.

Wittmann G., Demeestere K., Dombi A., Dewulf J., Van Langenhove H. 2005. Preparation, structural characterization and photocatalytic activity of mesoporous Ti-silicate. *Appl. Catal. B: Environ.*, 61: 47–57.

Wu L., Yu J.C., Wang X., Zhang L., Yu J. 2005. Characterization of mesoporous nanocrystalline TiO₂ photocatalysts synthesized via a sol-solvothermal process at a low temperature. *J. Solid State Chem.*, 178: 321–328.

Yanagisawa T., Shimizu T., Kuroda K., Kato C. 1990. The preparation of alkyltrimethylammonium-kanemite complexes and their conversion to microporous materials. *Bull. Chem. Soc. Jpn.*, 63: 988–992.

Yang J., Zhang J., Zhu L., Chen S., Zhang Y., Tang Y., Zhu Y., Li Y. 2006. Synthesis of nano titania particles embedded in mesoporous SBA-15: characterization and photocatalytic activity. *J. Hazard. Mater.*, B137: 952–958.

Yu K., Lee G.W.M., Huang W., Wu C., Yang S. 2006. The correlation between photocatalytic oxidation performance and chemical/physical properties of indoor volatile organic compounds. *Atmos. Environ.*, 40: 375–385.

Zhang M., An T., Fu J., Sheng G., Wang X., Hu X., Ding X. 2006. Photocatalytic degradation of mixed gaseous carbonyl compounds at low level on adsorptive $\text{TiO}_2/\text{SiO}_2$ photocatalyst using a fluidized bed reactor. *Chemosphere*, 64: 423–431.

Zhang Q.H., Gao L., Guo J.K. 1999. Preparation and characterization of nanosized TiO_2 powders from aqueous TiCl_4 solution. *Nanostructured Mater.*, 11: 1293–1300.

Zhang W., Froba M., Wang J., Tanev P.T., Wong J., Pinnavaia T.J. 1996. Mesoporous titanosilicate molecular sieves prepared at ambient temperature by electrostatic (S^+T , $\text{S}^+\text{X}^-\text{T}^+$) and neutral ($\text{S}^\circ\text{T}^\circ$) assembly pathways: a comparison of physical properties and catalytic activity for peroxide oxidations. *J. Am. Chem. Soc.*, 118: 9164–9171.

Zhang W., Pauly T.R., Pinnavaia T.J. 1997. Tailoring the framework and textural mesopores of HMS molecular sieves through an electrically neutral ($\text{S}^\circ\text{T}^\circ$) assembly pathway. *Chem. Mater.*, 9: 2491–2498.

Zhao D., Feng J., Huo Q., Melosh N., Fredrickson G.H., Chmelka B.F., Stucky G.D. 1998. Triblock copolymer syntheses of mesoporous silica with periodic 50 to 300 angstrom pores. *Science*, 279: 548–552.